Structural Characterisation of Heteroepitaxial Zincblende Gallium Nitride

Lok Yi Lee

Hughes Hall

Department of Materials Science and Metallurgy

University of Cambridge

This dissertation is submitted for the degree of Doctor of Philosophy

January 2019

Structural Characterisation of Heteroepitaxial Zincblende Gallium Nitride

Lok Yi Lee

To achieve white and colour-tuneable lighting, the mixing of light from red-, green- and blue- wavelength LEDs is desired. At present, the efficiency of green-wavelength LEDs based on InGaN is only about half that of red phosphide and blue nitride LEDs. This is known as the 'green gap' problem. III-nitrides based on the zincblende crystal structure have the potential to bridge the 'green gap' due to the theoretically achievable absence of internal polarisation fields that plague the commonly used c-plane wurtzite crystal structure.

In this thesis, metastable zincblende GaN grown by metal-organic vapour phase epitaxy is stabilised on 3C-SiC/Si substrates with a miscut, ranging from 0° to 4°. Crystalline zincblende GaN nucleates as elongated islands which coalesce with increasing GaN deposition. Annealing of nucleation layers reduces the substrate coverage, due to both material desorption and the ripening of islands. Incomplete substrate coverage of the nucleation layer results in a low zincblende phase purity and pits in the subsequent epilayer. For epilayer growth, a temperature of around 885 °C and a V/III-ratio of 38 produce zincblende GaN with a phase purity of more than 98 % and the lowest surface roughness in the range of parameters investigated. The surface morphology of elongated features found in both nucleation layers and epilayers is explained by the anisotropic diffusion of adatoms on the low-symmetry top monolayer of (001)-oriented zincblende GaN lattice. Defects, including stacking faults and dislocations, are found to relax the heteroepitaxial zincblende GaN film in both nucleation layers and epilayers. Miscut of the 3C-SiC/Si substrate, used to avoid the formation of antiphase domains, results in the preferential formation of the {111} stacking fault that is steeper with respect to the GaN/SiC interface. This reduces the efficiency of the annihilation between the oppositely inclined {111} stacking faults and thus limits the reduction in stacking fault density with epilayer thickness. Bunches of {111} stacking faults, with a range of spacings (up to around 10 nm) between stacking faults within a bunch, result in a broad photoluminescence emission peak with energy that extends above band gap of zincblende and wurtzite GaN.

The understanding of the physics behind the formation of the surface morphology can aid future decisions on the growth process to produce desired surfaces, while the knowledge of the origin and annihilation of stacking faults is useful for the consideration of defect reduction techniques for LED structures.

Declaration

This dissertation is the result of my own work and includes nothing which is the outcome of work done in collaboration except as declared in the Preface and specified in the text. It is not substantially the same as any that I have submitted, or, is being concurrently submitted for a degree or diploma or other qualification at the University of Cambridge or any other University or similar institution except as declared in the Preface and specified in the text. I further state that no substantial part of my dissertation has already been submitted, or, is being concurrently submitted for any such degree, diploma or other qualification at the University of Cambridge or any other University or similar institution except as declared in the Preface and specified in the text. It does not exceed 60,000 words, including summary/abstract, tables, footnotes and appendices, but excluding table of contents, photographs, diagrams, figure captions, list of figures/diagrams, list of abbreviations/acronyms, bibliography and acknowledgements.

Lok Yi Lee

January 2019

Acknowledgements

First of all, I would like to thank my supervisor, Prof. Rachel Oliver, for her excellent guidance, nurture and the opportunity to study towards a PhD at the GaN group. Her feedback on this thesis and other work have been invaluable.

Another very important mentor during my PhD studies is Dr Martin Frentrup, who also performed the XRD measurements in this thesis. We have sat through many scientific discussions for manuscripts and thesis chapters, and he has always been patient in answering my questions. Moreover he once wisely said that 'writing is an art', and taught me to create meticulous figures. I am grateful to him for all the above.

I would also like to thank everyone on the cubic GaN team at Cambridge: Prof. David Wallis for leading the cubic project and providing insightful discussions and interpretations of data during group meetings; Dr Menno Kappers for growing all the samples in this thesis and for his scientific insights; Petr Vacek for developing the stacking fault annihilation model and enlightening me with his TEM knowledge during his short but fruitful visit; and Dr Suman-Lata Sahonta for providing initial TEM training on cubic GaN. I also appreciate everyone's feedback on manuscripts, which often involved many iterations! I would also like to thank our collaborators at the University of Manchester, especially Stephen Church whose photoluminescence spectroscopy and modelling results are included in this thesis.

Dr Fabien Massabuau has been a great motivator during my studies. From sample prep to training on the JEOL 4000, I owe my TEM skills to him. He also helped me perform the STEM experiments on nucleation layers on the Titan. Lastly, a day at the office wouldn't be complete without hearing Fabien say: 'Don't be sad!'.

The GaN group has been wonderful company in the office, on Wednesday cake days and Social Fridays. Helen, Thomas, An and Tom were kind to help settle me in during my first year. John, Peter and Boning, Abhiram and Reza have also been friendly faces in the office. I would also like to thank Dr Alexander Hinz for his feedback on Chapter 7.

I had valuable opportunities to travel to local and international conferences, and would like to thank the NanoDTC in Cambridge, UK Nitrides Consortium, Hughes Hall Cambridge, and the Cambridge Philosophical Society for financial support.

Outside of the lab, Cambridge has provided me with many opportunities to explore different avenues, from ballet and coxing to NanoSoc and consulting, all of which have allowed me to meet wonderful people. A shout out goes to the Hughes Hall W1 crew whom I had the joy of coxing - I really enjoyed our adventures on the Cam and the Tideway! I would also like to thank my friend Sheen for always being around for meals and tea ever since the Oxford days. My cat Biscuit has aided the writing of this thesis with her cheekiness and purrs.

Finally, I am incredibly grateful to my parents for their unconditional support and love throughout my whole life, and for their regular early morning Skype calls in these past three years. I have also been blessed with the support of family and friends, especially Aunt Brenda and my grandmother who have provided laughs, advice and reminders to eat well.

List of publications

The following is a list of publications related to the work of this thesis.

1. **L. Y. Lee**, "Cubic zincblende gallium nitride for green-wavelength light-emitting diodes," *Mater. Sci. Technol. (United Kingdom)*, vol. 33, no. 14, pp. 1570–1583, 2017.

2. M. Frentrup, **L. Y. Lee**, S. L. Sahonta, M. J. Kappers, F. Massabuau, P. Gupta, R. A. Oliver, C. J. Humphreys and D. J. Wallis, "X-ray diffraction analysis of cubic zincblende III-nitrides," *J. Phys. D. Appl. Phys.*, vol. 50, p. 433002, 2017.

3. **L. Y. Lee**, M. Frentrup, P. Vacek, F. Massabuau, M. J. Kappers, D. J. Wallis, and R. A. Oliver, "Investigation of MOVPE-grown zincblende GaN nucleation layers on 3C-SiC/Si substrates," (under review)

4. **L. Y. Lee**, M. Frentrup, M. J. Kappers, R. A. Oliver, C. J. Humphreys, and D. J. Wallis, "Effect of growth temperature and V/III-ratio on the surface morphology of MOVPE-grown cubic zincblende GaN," *J. Appl. Phys.*, vol. 124, p. 105302, 2018.

5. **L. Y. Lee**, M. Frentrup, P. Vacek, M. J. Kappers, D. J. Wallis, and R. A. Oliver, "Investigation of stacking faults in MOVPE-grown zincblende GaN by XRD and TEM," *J. Appl. Phys.*, vol. 125, p. 105303, 2019.

6. S. A. Church, S. Hammersley, P. W. Mitchell, M. J. Kappers, **L. Y. Lee**, F. Massabuau, S. L. Sahonta, M. Frentrup, L. J. Shaw, D. J. Wallis, C. J. Humphreys, R. A. Oliver, D. J. Binks and P. Dawson, "Effect of stacking faults on the photoluminescence spectrum of zincblende GaN," *J. Appl. Phys.*, vol. 123, no. 18, p. 185705, 2018.

Remarks:
Chapter 3 is based on Publication no. 3. Chapters 5 and 6 were reproduced and extended from Publications no. 4 and 5 respectively, with the permission of AIP Publishing.

Contents

List of Abbreviations and Symbols

Abbreviations

AFM	atomic force microscopy
APD	antiphase domain
DAP	donor-acceptor pair
FWHM	full width at half maximum
HEB	high energy band
HRTEM	high-resolution transmission electron microscopy
LED	light-emitting diode
MBE	molecular beam epitaxy
MD	misfit dislocation
MOVPE	metal-organic vapour-phase epitaxy
PL	photoluminescence
QCSE	quantum-confined stark effect
QW	quantum well
RHEED	reflection high energy electron diffraction
rms	root mean square
SF	stacking fault
HR-STEM	high-resolution scanning transmission electron microscopy
TEM	transmission electron microscopy
wz	wurtzite
XRD	x-ray diffraction
ZA	zone axis
zb	zincblende

Symbols

b	Burgers vector
g	reciprocal space vector
2θ	angle between the scattered beam and the incident beam
v	Poisson's ratio

1 Introduction

1.1 Why green-wavelength LEDs?

In the UK and around the world, about 20% of electricity consumption is typically used on lighting. [1] Therefore a significant amount of electricity can be saved by using highly energy efficient light-emitting diodes (LEDs) as light sources instead of the traditional incandescent and fluorescent lighting. At present, virtually all commercial LED light bulbs that emit white light utilise blue-wavelength gallium nitride-based (GaN) LEDs capped with a phosphor. The phosphor absorbs parts of the blue spectrum and re-emits the other colours of longer wavelengths in the visible spectrum, with the superposition of the different wavelengths producing white light. Since there is inevitable energy loss during the wavelength conversion in the phosphor, a more energy efficient system of producing white light is to mix light from red, blue and green LEDs, with the additional benefit that their intensities can be varied to produce colour-tuneable lighting. The ability to tune the wavelengths of indoor lighting throughout the day has potential health benefits, as studies have suggested that exposure to blue wavelengths in the evenings through LED-lit devices suppresses the body's production of melatonin, a hormone that promotes sleepiness. [2]

1.2 LED structure and operation

A schematic of the structure of an LED is shown in Figure 1.1. Applying a forward-bias across the p- and n-contacts results in holes from the p-type layer and electrons from the n-type layer moving towards the InGaN/GaN multiple quantum well (MQW) region, where radiative recombination occurs between electrons and holes to

produce photons. It is also possible that non-radiative recombination takes place instead, for example due to defect states within the bandgap, to produce phonons. The efficiency of an LED is often expressed in terms of the internal quantum efficiency (IQE) and external quantum efficiency (EQE), which are the ratio of radiative electron-hole recombinations to number of injected carriers, and the ratio of emitted photons to injected carriers, respectively.

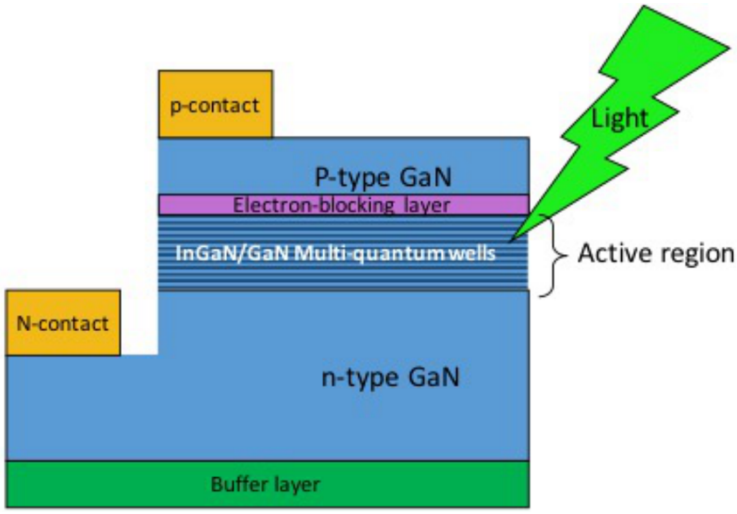

Figure 1.1 Schematic of an LED structure with InGaN/GaN multiple quantum wells as active layers and light extraction via a cleaved side facet. Figure from Prof. David Wallis.

The main purpose of the InGaN/GaN MQW region is to spatially confine the electrons and holes together in a small region, so that the probability that they will meet and recombine is greatly increased, and thus the radiative recombination rate and the overall IQE are also increased. This is possible as the GaN/InGaN band alignment is Type I and the GaN/InGaN/GaN heterostructure creates a QW structure, as shown in Figure 1.3.

The emission wavelength of the InGaN quantum wells can be tuned by the indium content (by changing the band gap energy, as shown in Figure 1.2) and the thickness of the quantum wells. Higher indium contents and thicker quantum wells are required to achieve green emission wavelengths. From Figure 1.2 which presents Γ-valley energy gap values for relaxed III-nitride layers at 300K, the indium contents of $In_xGa_{1-x}N$ alloys that have green emission band gaps of 2.3 eV are x = 0.26 and 0.31 for the zincblende and wurtzite structures respectively. Since the InGaN quantum wells are strained in LEDs, the band gap is calculated to be 0.173 eV larger for fully strained $In_xGa_{1-x}N$ (x = 0.26) layers compared with relaxed layers, using the method in Morkoc *et al.* [3] and

material constants from Vurgaftman *et al.* [4].

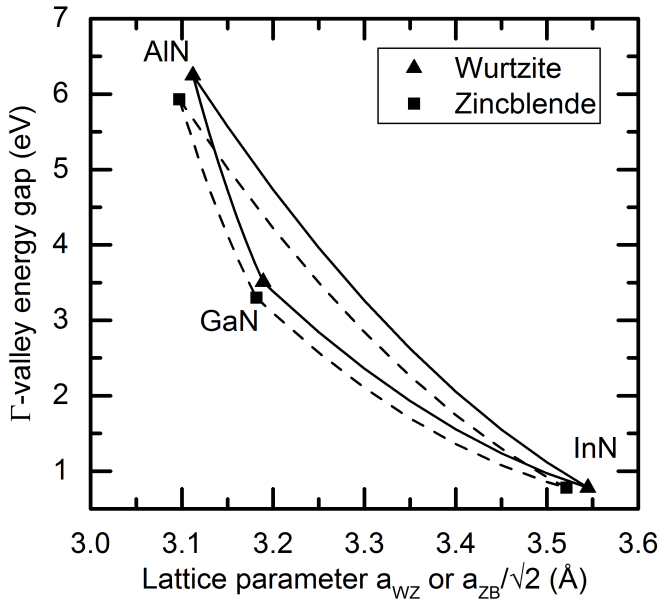

Figure 1.2 Γ-valley energy gaps at 300K of wurtzite and zincblende III-nitrides. Energy gaps are plotted as a function of lattice parameter a_{wz} for wurzite and $a_{zb}/\sqrt{2}$ for zincblende, both of which correspond to the distance between group-III ions in the (001) plane. Values from Vurgaftman *et al.* [4] and As *et al.* [5].

1.3 The 'green gap' problem

Currently, green indium gallium nitride (InGaN) LEDs only have less than half the EQE of blue InGaN and red aluminium gallium indium phosphide (AlGaInP) LEDs [6], and this is known as the 'green gap' problem. Phosphide-based LEDs for green-wavelength emission suffer from an indirect bandgap which lowers the radiative recombination efficiency. For nitride-based LEDs, the bandgap is direct but there are several possible factors that can contribute to the 'green gap' problem, with all of them related to the requirement that a higher indium content of around 11% is required in the InGaN quantum wells for emission of green wavelengths (540 nm) compared to blue wavelengths (470 nm) for the wurtzite crystal structure.

Most of the commercial LEDs are currently grown in the c-plane (0001)-oriented hexagonal wurtzite crystal structure, which results in piezoelectric and spontaneous polarisation fields in the [0001] growth direction across the LED device structure. The internal electric field across a wurtzite InGaN/GaN MQW structure can be as large as several MV cm^{-1} for a typical blue-emitting LED. [7] Figure 1.3 compares the band

structures of a InGaN/GaN quantum well (a) with and (b) without the presence of an electric field. The internal electric field results in the bending of the band structure of the InGaN/GaN quantum well and spatial separation between the electron and hole wavefunctions, thus lowering the rate of radiative recombination and decreasing the radiative efficiency of the QW. This is known as the quantum confined Stark effect (QCSE). An additional effect of the QCSE is a decreased band gap energy, resulting in a redshift of the emission wavelength.

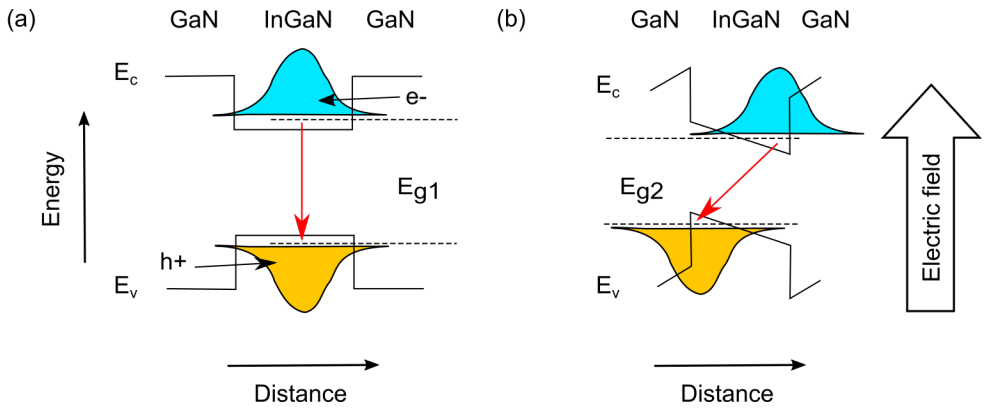

Figure 1.3 The band diagrams of an InGaN/GaN quantum well in the (a) absence and (b) presence of an internal electric field, illustrating the quantum confined Stark Effect. The labels 'E_c' and 'E_v' indicate the energy levels of the edges of the conduction and valence bands, respectively. The blue and orange curves represent the electron and hole wavefunctions, respectively.

Although all working diodes are subjected to the QCSE due to external bias, the internal piezoelectric and spontaneous electric fields present in the c-plane wurtzite crystal structure exacerbate the effect. In order to reduce such internal electric fields, many groups have focussed their studies on wurtzite GaN structures with non-polar (m-plane and a-plane) and semi-polar orientations, but the efficiencies of such LEDs have not been as high as expected and lag behind those of c-plane wurtzite LEDs. [8] Throughout this thesis, the c-plane orientation is implied where the wurtzite structure is mentioned, unless explicitly stated otherwise.

Increased indium concentrations and thickness in the InGaN quantum wells result in larger lattice mismatch and strains with the GaN quantum barriers, thus larger piezoelectric polarisation fields. Again, this results in a lower rate of radiative recombination. Moreover, the density of extended defects, such as misfit dislocations and trench defects, have been shown to increase with higher indium content [9,10] and are likely to result in higher rates of non-radiative recombination [11,12]. The lower rates of radiative recombination and higher rates of non-radiative recombination from the above factors

result in the decrease in IQE and EQE of c-plane wurtzite GaN LEDs of decreasing wavelengths from blue to green.

1.4 Properties of zincblende and wurtzite III-nitrides

The cubic zincblende (zb) structure and the hexagonal wurtzite (wz) structure are two different crystal polytypes of the same material, differing in the arrangement of the atoms within the material. The lattice parameters a and c are equal for the zincblende structure, whereas $a \neq c$ for the wurtzite structure, as depicted in Figure 1.4 [13].

III-nitrides with the wurtzite structure exhibits a net dipole along the [0001] direction or 'spontaneous polarisation' due to the partially ionic nature of the III-N bonds and an absence of inversion symmetry in the crystal structure (i.e. the (0001) and (000-1)-oriented crystals are distinct from each other). Additionally, wurtzite III-nitrides display a piezoelectric response when strained to result in 'piezoelectric polarisation'.

On the other hand, in the natural and relaxed zb-III-nitrides structure, there is no spontaneous polarisation along the [001] growth direction due to the perfect symmetry of bonds in the cubic structure. Piezoelectric polarisation would only occur in a zb-III-nitride structure if a shear strain were applied to the crystal. Therefore normal strains arising from higher indium content in QWs and increased thickness of QWs for green-wavelength emission do not contribute to internal electric fields for zb-InGaN, and both indium content and thickness of wells can be tuned in a wider range without reducing recombination efficiency in theory.

Moreover, zb-InGaN has a smaller bandgap than wz-InGaN by around 0.14 eV at 300 K, as shown in Figure 1.2. Therefore, zb-InGaN quantum wells require lower In incorporation compared with equivalent non-polar or semi-polar InGaN quantum wells. However, zb-GaN is a metastable phase while wz-GaN is the thermodynamically more stable phase, so careful selection and optimisation of growth conditions are required.

In addition to green-wavelength LEDs, the absence of internal electric fields in zincblende III-nitrides is beneficial for other optoelectronic devices that contain quantum well or quantum dot active regions, including near-UV AlGaN/GaN emitters [14], quantum well infrared photodetectors and quantum cascade lasers [15]. Moreover, both normally-on and normally-off heterojunction field effect transistors can be realised with zincblende AlGaN/GaN grown on 3C-SiC substrate [16,17].

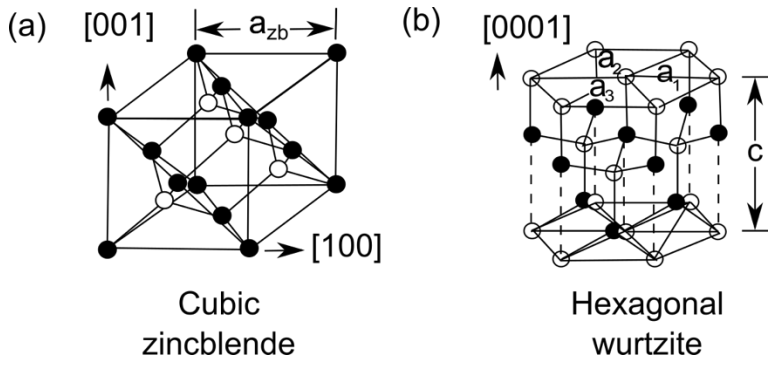

Figure 1.4 Crystal structures of (a) wurtzite and (b) zincblende. Figure reprinted by permission from Springer Nature Customer Service Centre GmbH: [13].

1.5 Growth methods

GaN and GaN-based heterostructures are grown in an epitaxial manner, where a crystalline thin film is deposited monolayer by monolayer on a crystalline substrate. The orientation and crystal structure of the thin film are determined by the substrate. Zincblende GaN has been mainly grown by molecular beam epitaxy (MBE) and metal-organic vapour phase epitaxy (MOVPE).

1.5.1 MBE

MBE is an ultra-high vacuum technique in which the ultra-pure forms of the elements are made to sublime, either by heating or electron beam evaporation. The fine molecular beams formed in this way are directed to a heated substrate, where the atoms of the different elements become physically adsorbed and subsequently incorporated into the crystal lattice through formation of bonds with neighbouring lattice atoms. The low growth rates (50 - 400 nm/h for zb-GaN) of this process notionally allow precise atomic layer control of the growth.

1.5.2 MOVPE

In MOVPE, a carrier gas, such as N_2 or H_2, is bubbled through solutions of the precursors, and the gas saturated with precursors is introduced into the reaction chamber. In the reaction chamber, the precursors flow laminar above the heated substrate and decompose by pyrolysis to leave behind the pure elements (e.g. Ga, In and N). Like MBE growth, the pure elements are then physically adsorbed on the heated substrate and incorporated into the crystal lattice. MOVPE does not require an ultra-high vacuum and

has a faster growth rate compared with MBE, hence it is widely employed in industry for the growth of commercial GaN-based LEDs.

The zb-GaN samples studied in this thesis are grown by MOVPE in Cambridge by Dr. Menno Kappers, using a 6 × 2 inch Thomas Swan close-coupled showerhead reactor. The gaseous precursor molecules, trimethylgallium (TMGa) and ammonia (NH_3), are introduced onto a heated 3C-SiC/Si substrate for GaN growth. The carrier gas, hydrogen, is passed through a bubbler containing the liquid TMGa precursor, so that it becomes saturated with TMGa vapour as it flows through. The vapour pressure, and thus the amount of TMGa that is carried into the reactor, is controlled by adjusting temperature of the bubbler. Figure 1.5 shows a schematic of the MOVPE reactor used. The gaseous precursors are introduced onto the substrate surface through the many tiny outlet tubes of a showerhead at the top the reactor. The substrates are heated by the susceptor underneath them. The substrate temperature, reactor pressure, flow rate of the gases into the reactor, and the ratio of partial pressures of NH_3 and TMGa (V/III ratio) can be controlled to produce different MOVPE growth conditions. The overall reaction to produce crystalline GaN is as follows:

$$Ga(CH_3)_3\ (g) + NH_3\ (g) \rightarrow GaN\ (s) + 3\ CH_4\ (g)$$

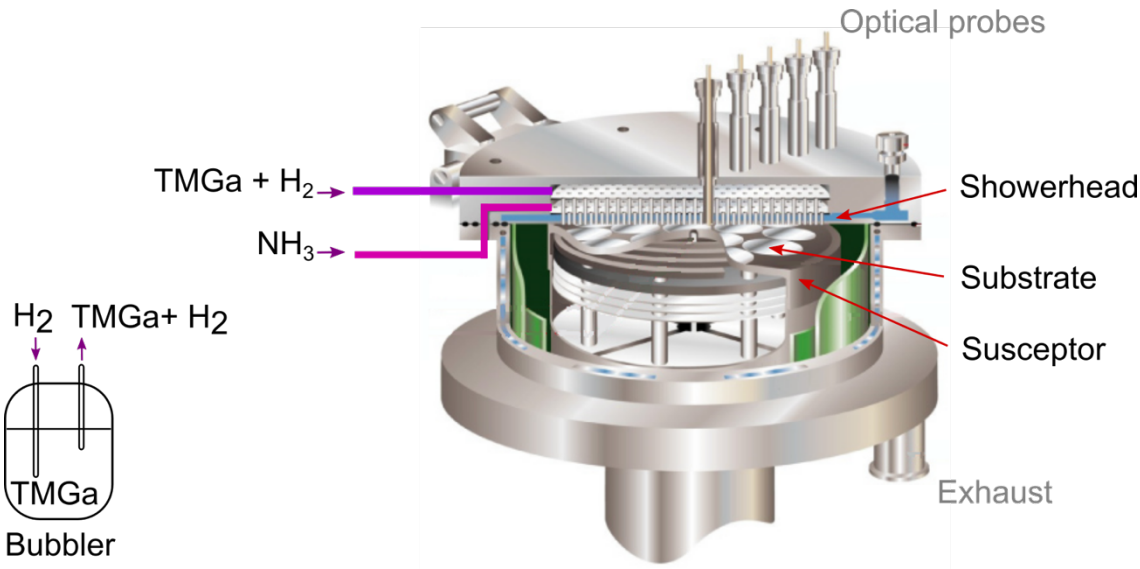

Figure 1.5 Schematic of the Thomas Swan close-coupled showerhead reactor. Figure adapted from [18], reproduced with permission of IOP Publishing.

1.5.2.1 Growth steps

Thin film growth of zb-GaN typically consists of several steps. After annealing and cleaning of the substrate, a low-temperature nucleation layer of a few nanometres is often grown at around 600 °C [19–23] to ensure wetting of substrate, 2D growth mode and high phase purity of zb-GaN growth at increased temperatures. The substrate temperature during subsequent GaN growth can affect the kinetics of the growth surface and is important in controlling the polytype of GaN that nucleates on the surface. [24]

Zincblende GaN is typically reported to be stabilised by growth at lower temperatures of 600 - 950 °C, whereas temperatures of 1000 – 1100 °C are used for growth of wz-GaN. Moreover, the substrate temperatures reported for MOVPE (900 – 950 °C) [22,25,26] are generally higher than MBE (600 – 835 °C) [20,23,27–31], which reflects in part that the low pressures used in MBE impacts the stability of zb-GaN at higher temperatures. The ratio of N to Ga, or V/III ratio, can affect surface diffusion since N adatoms have a higher sticking coefficient than Ga adatoms. [32] A high V/III ratio can thus limit surface diffusion and promote surface roughening, which has been reported to subsequently result in the nucleation of wurtzite inclusions. [20,31] Typical optimised V/III ratios used for MOCVD zb-GaN growth are 1000 – 1500. [22,33]

1.6 Substrates for the growth of zb-GaN

After its initial synthesis by Mizuta *et al.* in 1986, [34] zb-GaN received significant attention in the subsequent 15 or so years [35,36] before research efforts dwindled to that of only a handful of research groups. [37–42] However, due to its potential to overcome the 'green gap' problem, there has been renewed interest in zb-III-nitrides since 2010 with the recent demonstration of green light-emitting InGaN/GaN quantum well structures. [43]

The growth of wz-GaN is usually heteroepitaxial, which means that the substrate is not GaN but another material, since bulk GaN substrates are expensive and difficult to obtain. The correct choice of substrate is vital to achieve zb-GaN growth, and substrates with the zincblende structure have most commonly been selected as they provide the correct crystallographic template for zb-GaN growth. The zincblende substrates that have been studied for zb-GaN growth include: zb-GaAs (001) (by MBE [36,44–47] and MOVPE [25,33,37,48–51]), 3C-SiC (by MBE [40]), 3C-SiC on Si (by MBE [19,27–29,52–55] and MOVPE [26]), and patterned 3C-SiC on Si [56]. Some of the substrate properties to consider are lattice

matching and difference in thermal expansion coefficient with zb-GaN and cost.

The lattice parameters at 298 K of zb-GaN and the various substrate materials are presented in Table 1.1. Zincblende GaAs substrates and zb-GaN have a large lattice mismatch of - 20.3% resulting in a high density of defects in the zb-GaN layer. [57] 3C-SiC substrates have a much lower lattice mismatch of + 3.4% with zb-GaN [58] which thus produces zb-GaN with improved crystallinity and lower content of wurtzite inclusions. [19,52,53] However, the high cost of the 3C-SiC substrates compared with substrates such as silicon can limit their commercial viability.

	Lattice parameter *a* at 297 K (Å)
zb-GaN	4.506 [58]
3C-SiC	4.3596 [59]
zb-GaAs	5.653 [60]

Table 1.1 Lattice parameters of zb-GaN, 3C-SiC and zb-GaAs.

By depositing only a few micrometres of 3C-SiC onto Si substrates, as shown in Figure 1.6, the 3C-SiC layer can act as a pseudo-substrate to provide close lattice matching between GaN and SiC. 3C-SiC/Si substrates are potentially the only viable substrate for cost-effective zb-GaN. The commercial viability of zb-GaN LEDs grown on 3C-SiC/Si substrates is increased by the availability of large area (up to 150 mm in diameter) Si substrates. The fact that a Si substrate is used means that devices are compatible with silicon technology. Moreover, the higher thermal stability of 3C-SiC than GaAs substrates is preferable because of the relatively high temperatures required for GaN growth. [26] 3C-SiC layers have been grown on silicon by chemical vapour deposition [22], carbonising with a carbon-containing gas such as C_2H_2 [32], and high-dose carbon ion implantation [29].

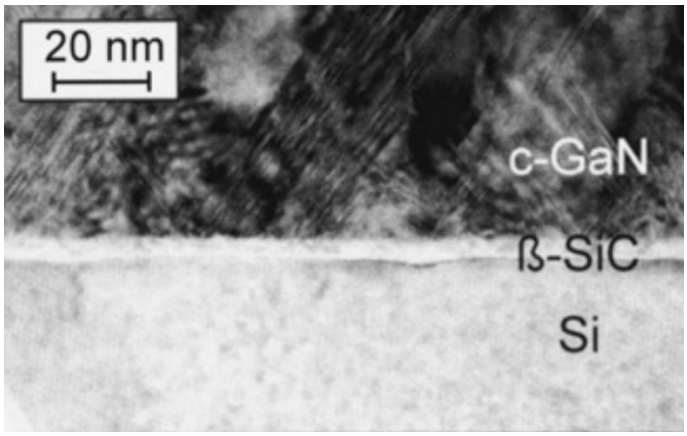

Figure 1.6 Zincblende GaN epilayer grown by MBE on thin 3C-SiC/Si (001) substrates. Reprinted from [20], with the permission of AIP Publishing.

More recently, Stark *et al.* [43] and Bayram *et al.* [61] have both used patterned Si substrates with {111} side walls, although in slightly different geometries. Referring to Figure 1.7, the wz-GaN (0001) phase first nucleates on the two opposite {111} side walls. As the wurtzite crystals from opposite walls meet, the (0001) planes become the {111} planes of a zincblende crystal [43], since the wurtzite (0001) plane and zincblende {111} planes are close-packed planes and the two crystal structures only differ by the stacking sequence of such planes. Such methods result in stripes of zb-GaN crystal being formed, with a width of ~ 1μm and a length limited by the size of the substrate. A method which allowed the growth of planar films on large-area substrates that are readily available would be much more attractive.

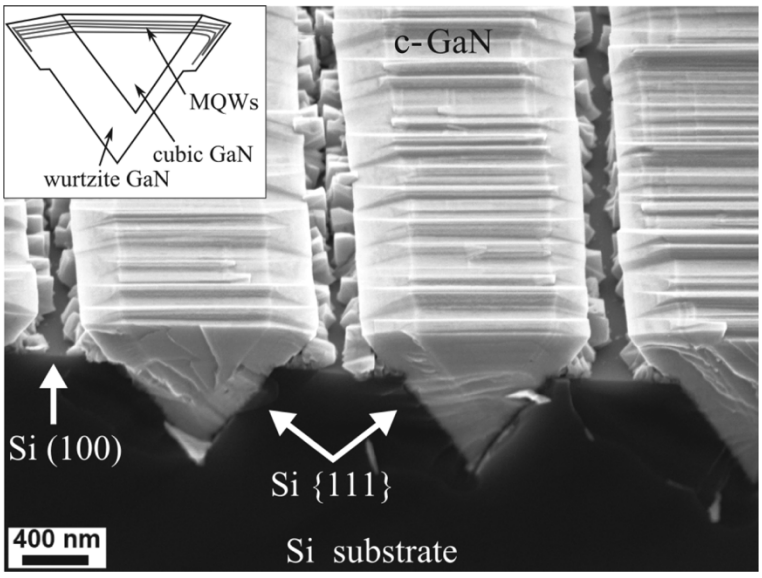

Figure 1.7 Coalescence of the two wurtzite crystal nucleated at the Si {111} side walls result in the formation of zb-GaN phase. Reprinted from [43], with the permission of AIP Publishing.

1.6.1 Defects in 3C-SiC/Si (001) substrates

In our work, we have chosen 3C-SiC/Si (001) substrates for the epitaxial growth of zb-GaN. The presence of native defects in the SiC layer of 3C-SiC/Si (001) substrates can affect the subsequent GaN epitaxy. The defects in the SiC layer that have been reported in literature include antiphase domains and stacking faults.

1.6.1.1 Antiphase domains (APDs)

Antiphase domains in the 3C-SiC layer grown on Si (001) substrates are formed in the following manner. They arise since the heights of a monolayer in Si and SiC are 0.25 and 0.5 of their lattice parameters *a*, respectively. A Si (001) substrate is usually not atomically flat and exhibits surface steps. Figure 1.8 (a) and (b) illustrates schematically two neighbouring SiC nuclei that have nucleated on different steps of step height $h = \frac{na_{si}}{4}$ on the Si substrate. If *n* is odd (Figure 1.8 (a)), the two SiC nuclei are translated in the (001) direction by half a monolayer relative to each other, such that a Si layer in one nucleus is level with a C layer in the neighbouring nucleus. The two nuclei thus have an antiphase relationship and an antiphase boundary results between them. On the other hand, if *n* is even (Figure 1.8 (b)), the two nuclei are translated in the (001) direction by a monolayer relative to each other, such that a Si layer in one nucleus is level with a Si layer in the neighbouring nucleus. The two nuclei therefore do not have an antiphase relationship and only a vertical displacement boundary results. Figure 1.8 (c) shows that if antiphase boundaries cross each other, they can be annihilated at the junction.

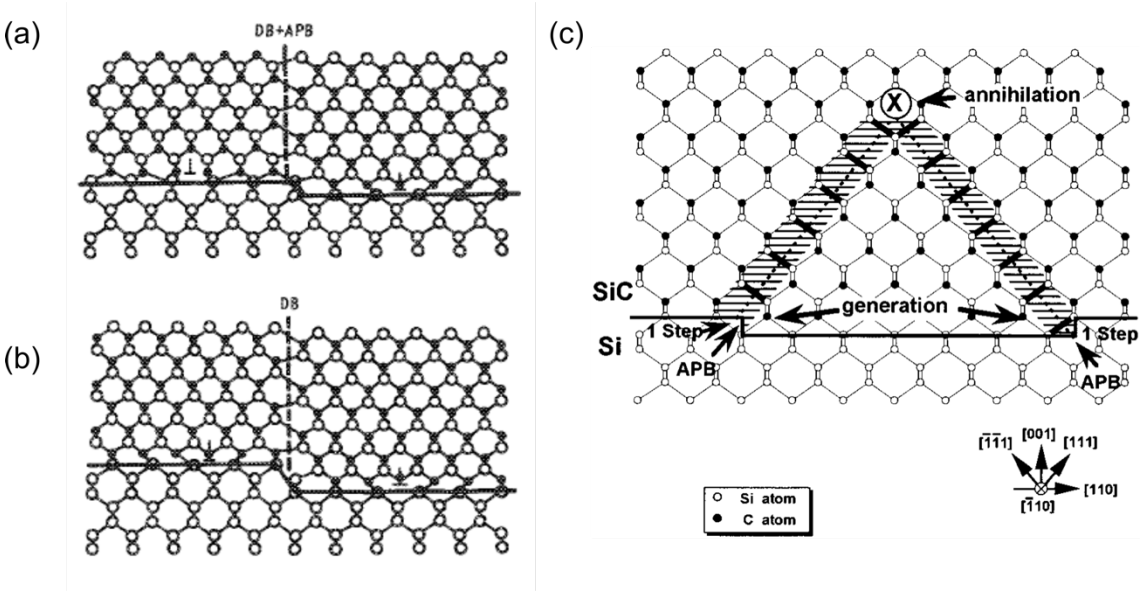

Figure 1.8 Schematics of two neighbouring 3C-SiC nuclei that have nucleated on different steps of a stepped Si (001) substrate with step height $h = \frac{na_{si}}{4}$, where in (a) n = 1, and in (b) n = 2. It is assumed that, SiC is more thermodynamically stable than Si and that the first layer that is deposited on the silicon (white circles) surface is a layer of carbon atoms (black circles). (a) and (b) reprinted from [62], with the permission of AIP Publishing. (c) Generation and annihilation of antiphase domains. Reprinted from [63], with the permission of John Wiley and Sons.

Antiphase domains in the 3C-SiC layer template the formation of similar defects in zb-GaN during its subsequent growth, as shown in Figure 1.9 [64].

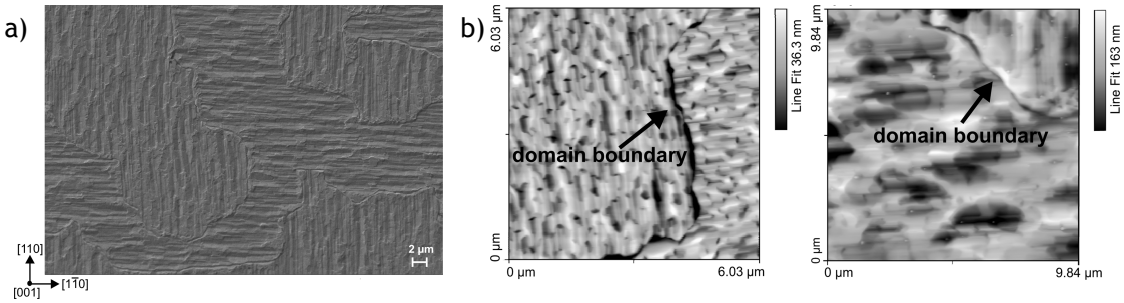

Figure 1.9 (a) SEM and (b) AFM images of antiphase domains in zb-GaN grown on 3C-SiC/Si (001) substrates. Reprinted from [64], with the permission of AIP Publishing.

When a Si (001) wafer is cut at a slight angle to the [001] direction, the wafer has a miscut, which is the angular difference between the [001] direction and the normal to the wafer surface, as shown in Figure 1.10. It is well-known that introducing a miscut to the substrate by cutting the Si (001) wafer at a slight angle (< ~ 5°) reduces the presence of antiphase domains in GaAs [65] and Si [66]. This is because miscut creates steps on the substrate. Huang *et al.* [66] proposed that the double step height was critical for achieving

antiphase domain suppression on the miscut Si substrate.

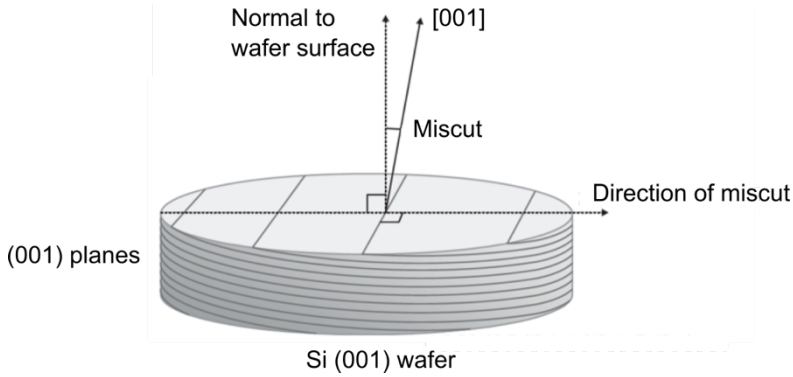

Figure 1.10 Si (001) wafer with a miscut. The miscut is the angular difference between the [001] direction and the normal to the wafer surface. Figure adapted from [67], with the permission of P. Kidd.

1.6.1.2 Stacking faults

A stacking fault in the 3C-SiC structure is a disruption of the zincblende ABCABC packing of the close-packed {111} planes. An intrinsic stacking fault is produced with the absence of one of the {111} planes, while an extrinsic stacking fault results from the addition of a {111} plane. 3C-SiC and Si have a large lattice mismatch of - 20%, and misfit dislocations and SFs are the dominant crystal defects to relieve the strain at the heterointerface. [68] Approximately 5 SiC cells fit with 4 Si cells, which would require the generation of misfit dislocations and extrinsic stacking faults in the SiC layer. Stacking faults in the 3C-SiC layer grown on Si substrates have been observed to originate mainly from the 3C-SiC/Si interface, and can terminate within the 3C-SiC layer as they intersect with each other, resulting in a decrease in stacking fault density with distance from the interface. [69,70] The stacking faults that extend to the top of the 3C-SiC layer can propagate into the subsequently grown GaN layer. {111}-type stacking faults in 3C-SiC have a low energy of formation, with a theoretically calculated value of - 3.0 mJ m^{-2} [71], which makes their formation difficult to avoid.

1.7 Defects in zb-GaN

1.7.1 Stacking faults and wurtzite inclusions

The stacking sequence of the close-packed {111} planes in the zincblende structure is ABCABCABC, while that of the close-packed {0001} planes in the wurtzite

structure is ABABABAB. An intrinsic stacking fault in the zincblende structure arises when a monolayer and is removed from the lattice, such that the stacking sequence of the {111} planes becomes AB**C**B**C**ABC, where the missing plane is between the letters in bold, as shown in Figure 1.11 (a). On the other hand, an extrinsic stacking fault in the zincblende structure occurs when a monolayer is inserted into the lattice, such that the stacking sequence of the {111} planes becomes ABC**B**ABC, where the additional plane is in bold, as shown in Figure 1.11 (b). Therefore, both intrinsic and extrinsic {111}-type stacking faults in the zincblende structure has wurtzite stacking for four and three monolayers, respectively.

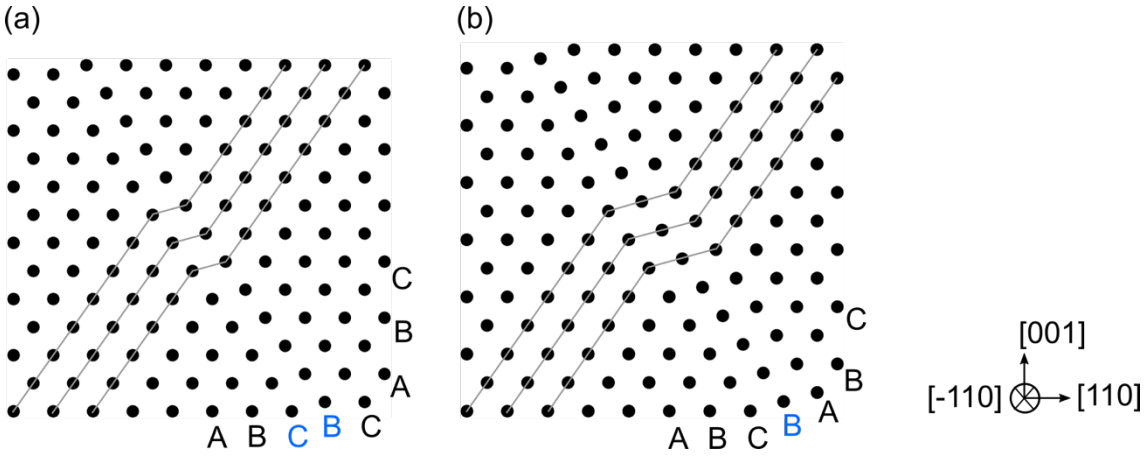

Figure 1.11 (a) Schematic of (a) an intrinsic stacking fault and (b) an extrinsic stacking fault in a zincblende lattice. Both schematics are projections of the {111} planes in the [-110] direction. The grey lines provide a guide to the eye for the arrangement of the atoms. Figures created by Petr Vacek.

Stacking faults in zb-GaN have been consistently found to lie on the {111} planes when grown on both GaAs [72,73], 3C-SiC [54,55] and patterned 3C-SiC/Si [56] substrates. The prevalence of stacking faults in zb-GaN is likely due to stacking faults having the same stacking sequence as the wurtzite structure, which is more thermodynamically stable than the zincblende structure. Wang *et al.* [32] and Ruiz-Zepeda *et al.* [74] reported that stacking faults originate from the rougher regions of the interface between the zincblende layer and a 3C-SiC/Si substrate. However, it is not clear if the stacking faults originate at the substrate surface steps, at existing stacking faults in the substrate, or at other locations. The stacking fault density in zb-GaN is found to decrease with the distance from the GaN/substrate interface by Martinez-Guerrero *et al.* [54], and it has been suggested that stacking faults lying on the {111} planes in the zincblende structure can intersect and annihilate to create a sessile dislocation in the <110>-type directions. Stacking faults are thought to act as nucleation sites for wurtzite inclusions. The presence of wurtzite

inclusions and stacking faults have been found to be correlated by Kemper *et al.* [75] and Martinez-Guerrero *et al.* [54], with the wurtzite inclusions nucleating on the {111} planes.

The impact of stacking faults on the optical properties of zb-GaN was reported by Kemper *et al.* [76]. It was found that as the density of {111} stacking faults decreased with increasing layer thickness, the STEM-cathodoluminescence (STEM-CL) emission intensity increased. This suggests that stacking faults reduce the efficiency of radiative recombination.

In wz-GaN, stacking faults have zincblende stacking and are thought to act as type–II QWs in the surrounding wurtzite lattice. [77,78] (For type-II band alignment, the band offsets for the conduction and valence bands are both either positive or negative, whereas in type-I, the band offset is positive for one band and negative for the other.) Since stacking faults in zb-GaN have the atomic stacking sequence of the wurtzite structure, it is possible that stacking faults in zb-GaN have similar type-II QW emission properties.

Kemper *et al.* [75] also reported that stacking faults resulted in MQWs with an undulating morphology, however whether this affects light emission properties still needs to be investigated.

An obvious and simple remedy to avoid the effects of stacking faults would be to grow thicker GaN films to reduce the stacking fault density near the MQW light emitting region of the LED, since oppositely inclined {111} stacking faults have been found to annihilate with each other. However, as we will see in Chapter 6, the efficiency of the annihilation process is affected by the substrate miscut for zb-GaN grown on 3C-SiC/Si substrates.

1.7.2 Misfit dislocations

For zb-GaN grown on GaAs substrate, misfit dislocations at the GaN/GaAs interface created by extra {111} lattice planes in GaN were revealed with high resolution TEM by Trampert *et al.* [79] in Figure 1.12. The extra {111} lattice plane in GaN occurs at every fifth {111} lattice plane in GaAs, and such a density of lattice planes almost perfectly accommodates the lattice mismatch of – 20.3 % between zb-GaN and GaAs.

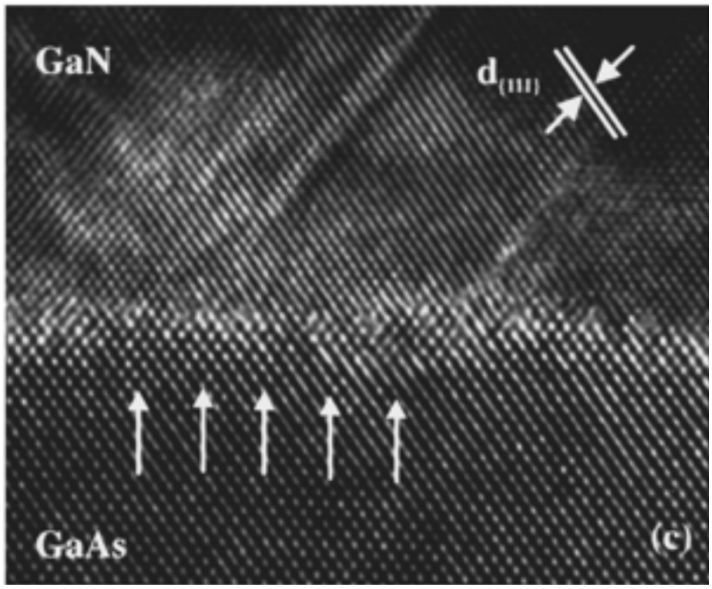

Figure 1.12 High resolution TEM image of zb-GaN grown on GaAs substrate from Trampert *et al*. Reprinted from [79], with the permission of AIP Publishing. The extra {111} lattice planes in GaN occurring at every fifth {111} lattice plane in GaAs are pointed out by the white arrows. The zone axis of the TEM image is assumed to be a <110>-type direction.

It is commonly found in fcc materials that a perfect 1/2 <110>-type dislocation dissociates into two partial 1/6 <112>-type dislocations on the same {111}-type plane, separated by an intrinsic stacking fault [80]. Theoretical calculations are necessary to verify whether the dissociation of the perfect dislocation in zb-GaN is energetically possible. [81]

1.8 Structure of thesis

This thesis presents a study of zb-GaN grown on 3C-SiC/Si substrates by MOVPE, with the goal of realising a zb-GaN based green-wavelength LED.

Chapter 2 introduces the techniques used in this thesis for the characterisation of zb-GaN, namely atomic force microscopy (AFM), X-ray diffraction (XRD), transmission electron microscopy (TEM) and photoluminescence (PL) spectroscopy. For each technique, the background principles, operation and data analysis methods are described as appropriate.

Our study of the growth of zb-GaN on 3C-SiC/Si substrates begins with the investigation of the nucleation stage. Since our zb-GaN nucleation layers (NLs) are grown at a lower temperature compared with the subsequent epilayer, NLs that are as-grown and annealed by heating to the higher epilayer growth temperature have been studied. Chapter 3 examines the effect of NL thickness on the properties of the NL and the

subsequent GaN epilayer, including surface morphology, phase purity, substrate coverage and strain. In Chapter 4, the crystallinity of the GaN/SiC interface and the nature and origin of defects in GaN NLs are investigated by high-resolution STEM with atomic resolution.

The remaining results chapters of the thesis investigate zb-GaN epilayers that are more than 300 nm thick.

Chapter 5 is a study to determine the optimum growth conditions to produce GaN epilayers with high phase purity and smooth surfaces required for the subsequent growth of InGaN/GaN quantum wells. The effect of miscut, growth temperature, V/III-ratio and reactor pressure on the surface morphology and phase purity are presented.

In order to avoid the formation of antiphase domains in the GaN epilayer, 3C-SiC/Si substrates with a 4° miscut have been used for the growth of zb-GaN in this work. In Chapter 6, we investigate the effect of the 4° miscut on the nucleation and subsequent annihilation of {111}-type stacking faults in the GaN epilayer.

The stacking faults in the GaN epilayer often occur as bunches. The effect of such stacking fault bunches on the photoluminescence properties of the GaN epilayer is studied in Chapter 7.

Finally, the conclusions and suggestions for future work are presented in Chapter 8.

2 Characterisation techniques

2.1 Introduction

This chapter describes the basic principles and operation of the techniques used in this thesis to characterise zb-GaN grown on 3C-SiC/Si substrates, including atomic force microscopy (AFM), X-ray diffraction (XRD), transmission electron microscopy (TEM), and photoluminescence (PL) spectroscopy. For each technique, the experimental details and data analysis methods used are described as appropriate.

2.2 Atomic force microscopy (AFM)

2.2.1 Operation principles

Atomic force microscopy (AFM) is a scanning probe microscopy technique, where a sharp physical probe interacts with the sample as it is rastered across the surface, and topographic information of the sample's surface can be obtained. A schematic of the typical set-up of an AFM is presented in Figure 1. The probe consists of a tip attached to a cantilever, and its x, y and z motions are enabled by piezoelectric actuators. A laser beam is directed to the top surface of the cantilever above the location of the tip, and is reflected into a four-sector photodiode detector. The signal is processed by a computer and the feedback circuit adjusts the z-motion of the probe as required, and the voltage ramps control the x and y motions of the probe.

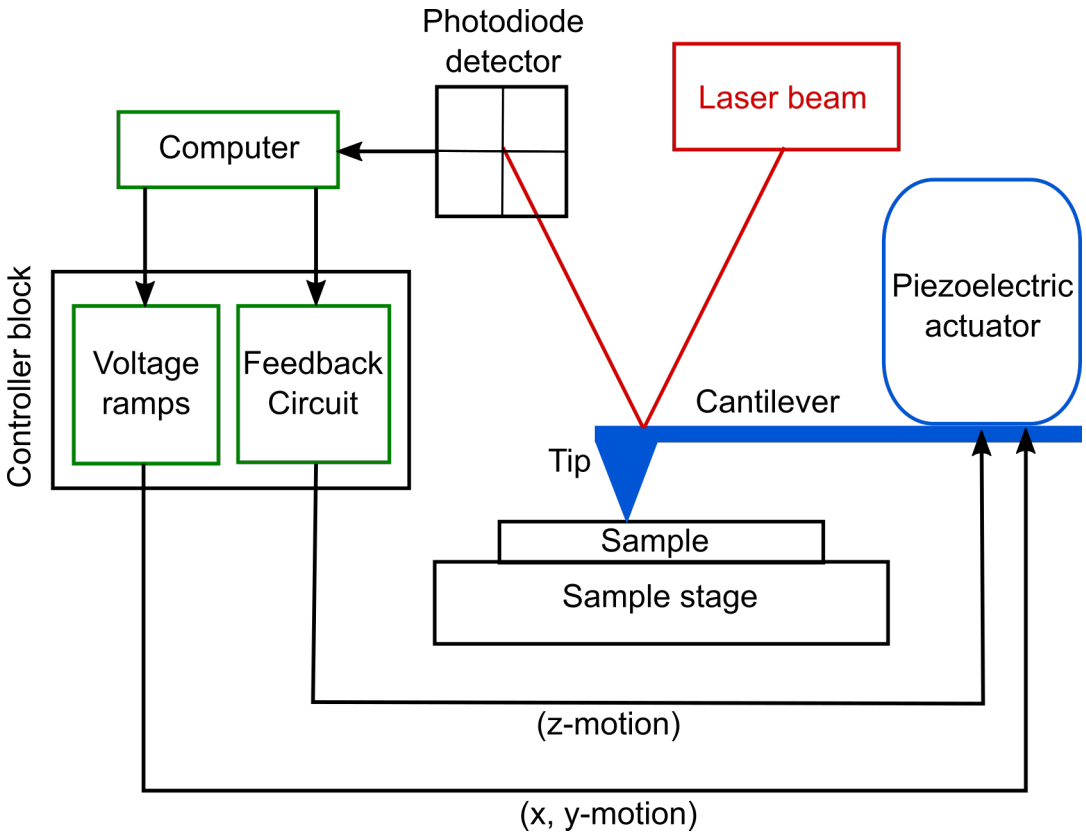

Figure 2.1 Schematic of the set-up of a typical AFM. Figure adapted from [82].

2.2.2 Modes of operation

Topographic information can be obtained from the AFM using contact mode, intermittent-contact mode, or non-contact mode. All the AFM data in this thesis was acquired with the intermittent-contact modes, TappingMode™ or PeakForce Tapping®, developed by Bruker Inc. To image the surface morphology of the samples in ambient air, TappingMode™ was performed on both the Digital Instruments Dimension 3100 AFM and Veeco Dimension Pro AFM, while only the latter was used for PeakForce Tapping® mode. MPP-11100-10 and RTESP-300 etched silicon probes from Bruker Nano Inc. with a nominal tip radius of 8 nm were used for TappingMode™, while ScanAsyst-Air-HR silicon nitride probes with nomial tip radius of 2 nm were used for PeakForce Tapping®.

2.2.2.1 TappingMode™

In TappingMode™, the probe is vertically oscillated slightly below its resonant frequency by a piezoelectric element so that it 'taps' the surface of the sample at the minima of each oscillation. As the probe is scanned across the surface in x and y directions, a change in the height of the surface results in a change in oscillation amplitude

of the probe, which is detected by the laser reflected off the end of the cantilever onto a photodiode detector. A feedback circuit uses the probe oscillation amplitude signal to adjust the z-motion of the probe to maintain a set oscillation amplitude, usually called the 'amplitude set-point'. An image of surface topography can then be obtained by using calibration data to convert the voltages applied to the scanner for a constant tip-sample distance during the scan to height information of the surface. [83]

The deviation of the probe oscillation amplitude to the set oscillation amplitude during a scan can be recorded, and an image produced by this amplitude error signal can also be used as a depiction of the shape of the surface. Figure 2.2 (a) is the height image of a zb-GaN epilayer surface consisting of domains with perpendicularly aligned features. The different domains can be more easily identify from the amplitude error image in Figure 2.2 (b).

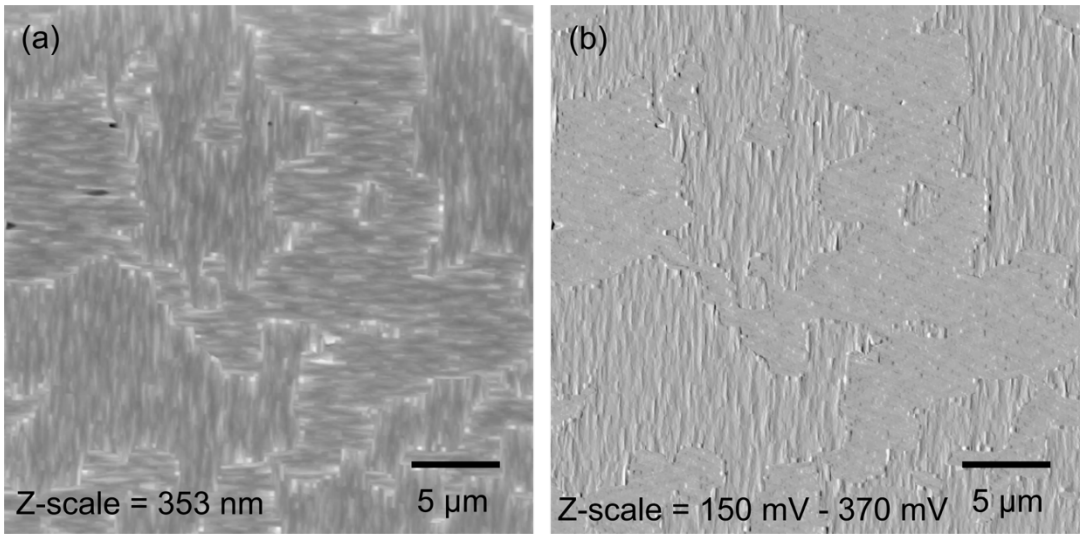

Figure 2.2 (a) Height image and (b) amplitude error image of a zb-GaN epilayer surface consisting of domains with perpendicularly aligned features.

2.2.2.2 PeakForce Tapping® mode

In PeakForce Tapping® mode, the probe is also vertically oscillated but at a frequency far below the resonant frequency. This low frequency oscillation is achieved using the main scanning piezo-actuator . During each oscillation, the z-motion imposed on the tip by the piezo-actuator which follows a simple sinusoidal waveform such that as the tip approaches the surface of the sample, the tip velocity approaches zero, as shown by the grey 'probe motion' line in Figure 2.3. However, the actual motion of the tip involves snapping onto and off the sample, and the accompanying changes in vertical force on the tip with time for each oscillation is plotted in the force-time curve in blue

and red in Figure 2.3. The following description of the tip motion and forces is adapted from Pittenger *et al.* [84]. At point 'A', the tip is furthest away from the sample surface in the oscillation and hence no force acts on the tip. As the tip approaches the samples surface, the tip is attracted towards the surface by long range forces such as electrostatic, van der Waals, and capillary forces. At point 'B', the cantilever can no longer sustain the attractive forces on the tip, which is pulled to the sample surface. As the tip is lowered further onto the sample, the vertical force on the tip acting against the direction of motion increases in magnitude. The 'peak force' occurs at point 'C' or the minimum of the sinusoidal z-motion. As the tip is withdrawn from the sample surface, the vertical force decreases to a minimum at point 'D' when the tip is pulled off from the surface, after which only long range attractive forces act on the tip and the z-motion reaches the maximum of the oscillation at point 'E'. A force-time curve is obtained during each oscillation at each pixel of the AFM image, and the 'peak force' is used by the feedback circuit to adjust the z-motion of the tip to maintain a set peak force. [85] The PeakForce Tapping® mode allows pN level interaction forces between the tip and sample that is significantly lower than the nN level used in TappingMode™. Such low tip-sample forces mean that the AFM tips do not get blunt as easily and can last longer.

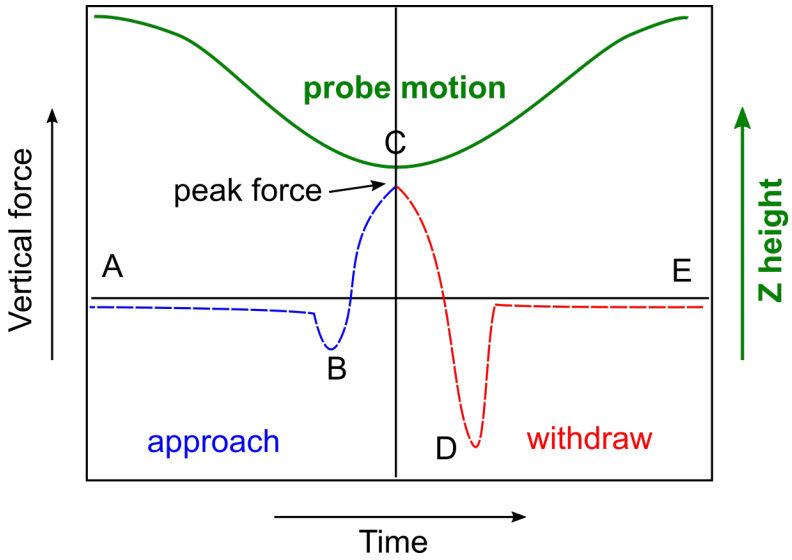

Figure 2.3 Motion and forces on the AFM tip during PeakForce Tapping® mode. Figure adapted from Bruker Inc. [86].

2.2.3 Imaging

The vertical resolution is notionally determined by the piezoelectric z-actuator which has sub-Angstrom precision, but can be limited by surrounding background noise in practice. Several factors can affect the lateral resolution, such as the size and shape of the AFM tip.

When imaging with the AFM, we should be aware of tip-related artefacts. As illustrated in the schematic in Figure 2.4, the geometry of the tip can result in a scanned profile (red dotted lines) that does not reflect the actual profile (solid black lines) of the surface features. The AFM tips used in this work typically have a front angle (FA) that is shallower than the back angle (BA), e.g. the RTESP-300 etched silicon probes used in this work has a FA of (15 ± 2)° and a BA of (25 ± 2)°. When the tip is rastered across a protruding or depressed feature such as in Figure 2.4 (a) and (b) respectively, the sidewall of the tip contacts the feature rather the apex of the tip in some parts. The feedback circuit registers the change in oscillation amplitude or peak force, and the z-motion of the tip is adjusted accordingly. This results in sidewalls of the tip being imaged instead of the surface feature. To accurately image features with facets, the angle of the facet from the horizontal should be smaller than (90° - FA) or (90° - BA). Moreover, for a depressed feature, the tip may not reach the bottom of the feature to result in a scanned profile where the measured feature depth is smaller than the real depth.

A damaged, blunt or dirty tip is likely to result in the same artefacts that occur

throughout the AFM scan. If the same artefacts also occur in the scan where the sample is rotated by e.g. 90°, the tip should be replaced and a new scan should be performed.

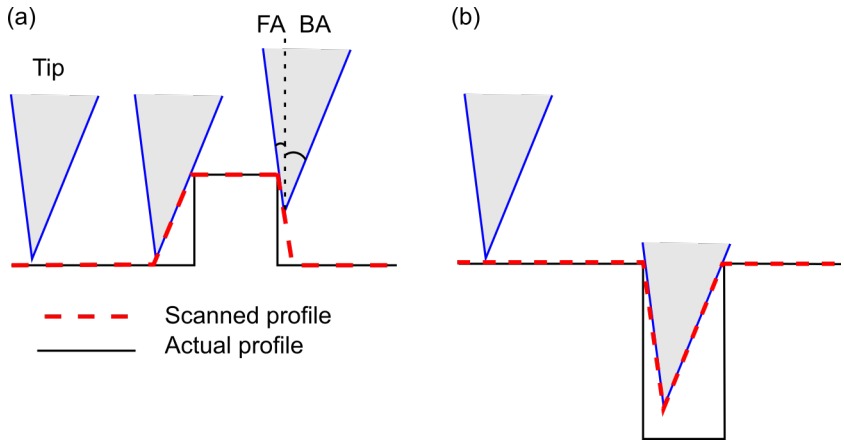

Figure 2.4 Effect of the front angle (FA) and back angle (BA) of the AFM tip on the scanned profile compared with the actual profile of (a) a protruding feature and (b) a depressed feature. Figure adapted from [87].

The pixel density of the AFM scan should be selected for a particular scan size such that the required details from the image can be resolved in a reasonable period of time, but the pixel size should not be significantly smaller than the lateral resolution.

Moreover, since the piezoelectric actuator scans a line in the x direction before moving on to the next line in the y direction, they are usually called the fast and slow scan directions and should be decided by considering the surface features of the sample. The fast scan direction is less affected by drift compared with the slow scan direction. If a sample contains elongated surface features that are aligned in one direction, the sample should be oriented such that the fast scan direction is perpendicular to the elongation direction of the surface features. In this way, the smaller dimension of the features can be more accurately imaged by the fast scan direction.

2.2.4 Image processing and analysis

The software WSxM [88] was used for the post-processing of AFM data. Scanner bow is an artefact arising from the fact that the probe does not scan in a perfectly flat plane but in a parabolic arc due to the hollow tube construction of the piezoelectric actuator. The flatten function was used to eliminate effects of scanner bow in the AFM data, especially on the larger area scans. This function calculates a least-squares-fit polynomial for each line of the AFM scan in the fast-scan direction, and subtracts the

polynomial from the original scanned line. Typically a 0^{th} or 1^{st} order polynomial fit was selected.

The root-mean-square (rms) roughness function was often used to obtain a measure of the roughness of the surfaces. The software first obtains the height distribution of an image, fits a Gaussian distribution to the data and the rms value of the distribution is given as the root-mean-square (rms) roughness [88]. The rms roughness values must always be compared between images of the same size processed in the same way.

2.2.5 Method for quantifying average surface feature size

The typical surface morphology of our zb-GaN epilayers consists of elongated surface features, as shown in the AFM height image in Figure 2.5 (a). To quantify the typical sizes of the surface features, we used the two-dimensional fast Fourier transform (2D-FFT) of the AFM scans that picks out the common frequencies in an AFM image. First, we applied a 2D-FFT filter the AFM scan (Figure 2.5 (b)). Then we extracted the intensity profile from the centre of the 2D-FFT pattern in the direction of the surface feature dimension we are interested in e.g. x and y. The intensity profiles typically followed a Gaussian distribution curve, as shown in Figure 2.5 (c) and (d), from which the full width at half maximum (FWHM) is obtained. By comparing with AFM profiles of surface features, we found empirically that the positive frequency at the FWHM of the Gaussian curve reflects the average feature size well. Since the positive and negative frequencies are symmetrical and are both included in the FWHM, the reciprocal of ½ × FWHM gives a measure of the average feature size. It is usually worth drawing several line profiles across the AFM height scan to check that the FFT method gives a reasonable feature size. When comparing feature sizes calculated using this method, it is important that the AFM scans used are of the same size. The judgement of the FWHM of the 'Gaussian' curve can be subjective, hence the same person should perform the analysis for data used in the same study.

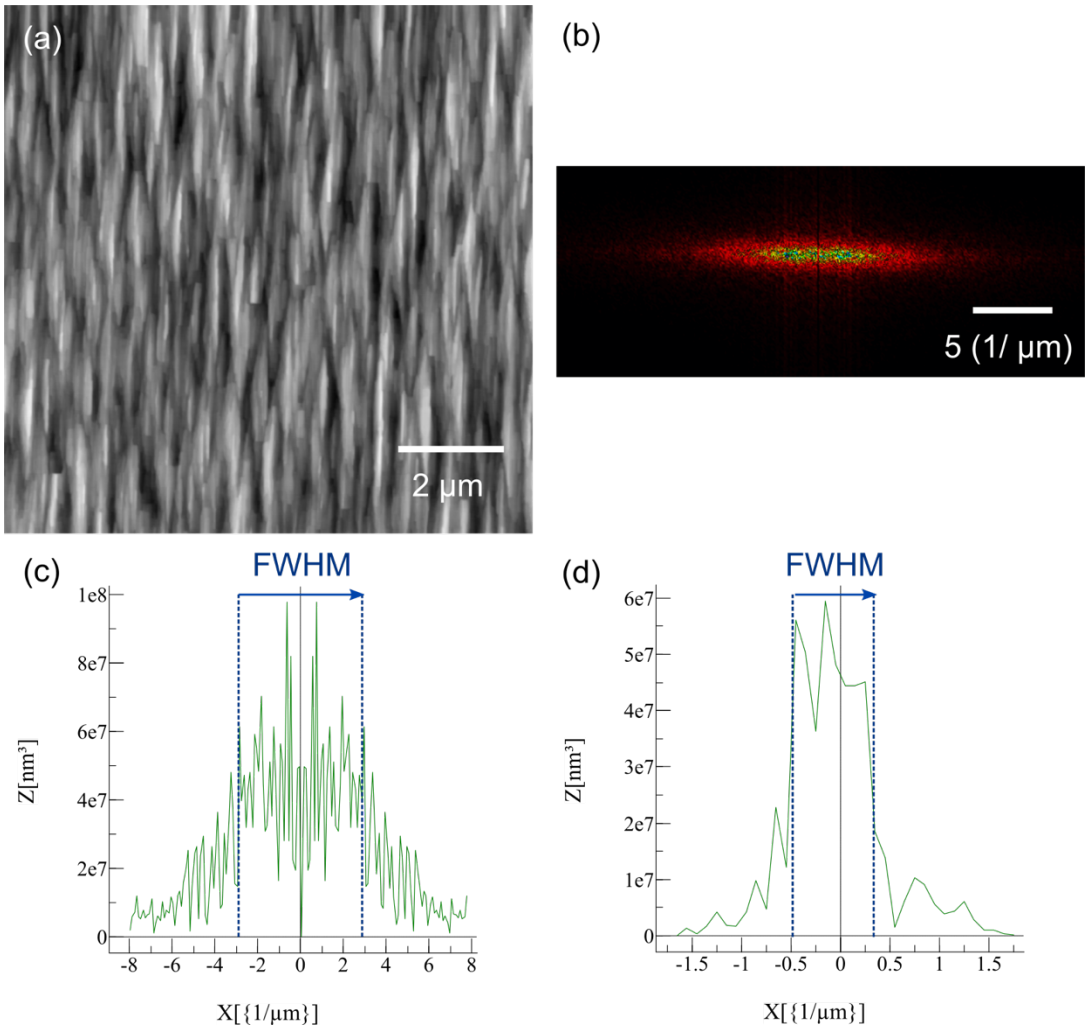

Figure 2.5. Method for quantifying average feature size from AFM height images. (a) 10 × 10 µm AFM height image. (b) 2D-FFT filter on the AFM height image in (a). (c) and (d) Profiles taken in the horizontal and vertical directions respectively. The processing and analysis above were performed with software WSxM [88].

2.3 High resolution X-ray diffraction (XRD)

2.3.1 Background theory

High resolution X-ray diffraction (XRD) is a quick and non-destructive technique that can be used to obtain information on the structural properties of crystalline materials, including phase purity, strain state and defects present in the material. This section is largely adapted from Chapter 3 'Principles of measurement' in 'XRD of gallium nitride and related compounds: strain, composition and layer thickness' by P. Kidd [67].

The technique is based on the diffraction of an X-ray beam by a crystalline sample and measuring the positions and intensities of the diffracted X-ray beams with a detector. The positions of the intensity peaks, also termed 'reflections', from a crystalline material is described by Bragg's law. In real space, Bragg's law can be understood as the path difference between X-rays scattered from neighbouring (*hkl*) crystal planes with spacing, d_{hkl}. Constructive interference of X-rays occurs if the path difference is an integer number of wavelengths, $n\lambda$. This condition is met when the incident and diffracted beam are both at the same angle, θ, from the diffracting plane. From Figure 2.6, we can equate the integer number of wavelengths to the path difference between the two X-ray beams from neighbouring planes, giving $n\lambda = 2d_{hkl}sin\theta$, which is Bragg's law. In X-ray crystallography, the expression is usually simplified to

$$\lambda = 2d_{hkl}sin\theta$$

as n is the order of reflection and $n > 1$ simply denotes the same diffraction condition but from planes that are d_{hkl}/n apart.

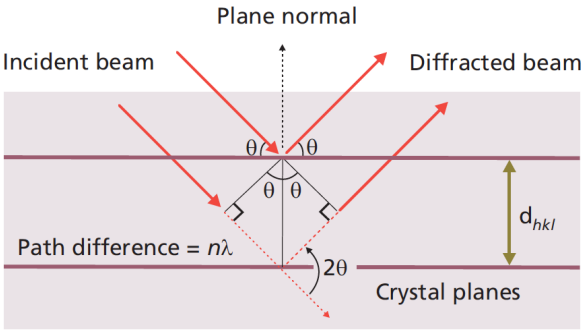

Figure 2.6. Schematic illustrating the constructive interference of two X-rays reflected off two diffracting planes separated by distance d_{hkl} at Bragg angle θ. Figure reproduced from [67], with the permission from P. Kidd.

A convenient fact is that the reciprocal space lattice of a crystal represents the positions of the reflections in reciprocal space. A reciprocal lattice vector is perpendicular to the set of (*hkl*) crystallographic planes it represents and has a length of $1/d_{hkl}$. Figure 2.7 illustrates the set up when the Bragg condition is met in reciprocal space. The scattering vector $\underline{Q}$, which represents the momentum difference between the wave vector of the incident beam $\underline{K_O}$ and detected beam $\underline{K_H}$, overlaps with the reciprocal lattice vector $\underline{d^*_{hkl}}$ of the set of planes.

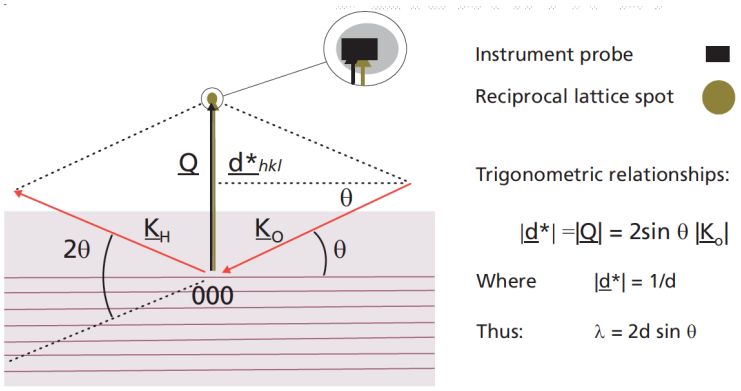

Figure 2.7. Schematic illustrating Bragg's law in reciprocal space. Figure reproduced from [67], with the permission from P. Kidd.

Figure 2.8 shows the various components and angles of an X-ray diffractometer. The detector position (2θ) and angle of incidence of the X-ray beam (ω) control the scattering vector. With the angles phi (φ) and psi (ψ), the crystal can be tilted and rotated in the goniometer. They are used to orient the crystal and thus the reciprocal lattice for a specific reflection in 3-dimensional space.

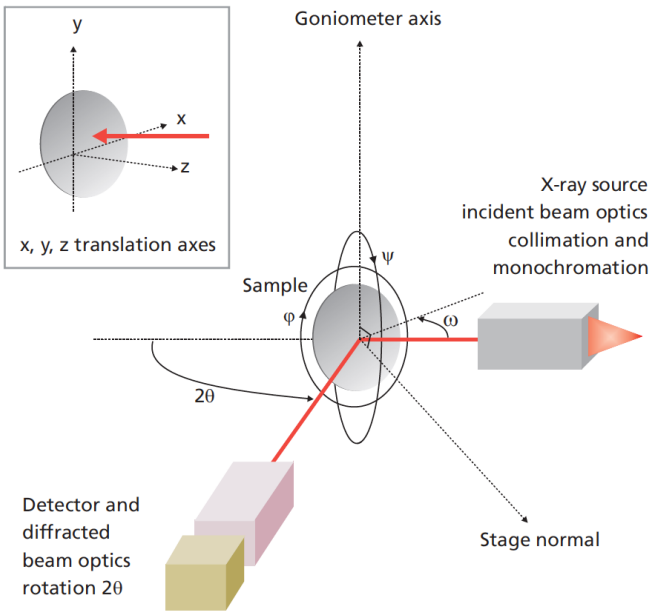

Figure 2.8. Schematic diagram of an X-ray diffractometer showing the various angles that can be changed accurately to measure diffracted intensities. Figure reproduced from [67], with the permission from P. Kidd.

2.3.2 XRD characterisation of zb-GaN grown on 3C-SiC/Si substrates

XRD was used to investigate the phase purity, strain state and defects of the zb-GaN samples, as well as the relative amounts of GaN deposited between samples. The XRD measurements in this thesis were performed by Dr Martin Frentrup. Two diffractometers with Cu-Kα sources (λ = 1.54056 Å) were used: the reciprocal space maps were measured with a PANalytical Empyrean diffractometer equipped with a two-bounce hybrid monochromator 0.25° primary beam slit, and a PIXcel solid-state area detector; while the ω-2θ measurements for strain analysis were performed on a Philips X'pert diffactometer consisting of a 4-crystal Bartels monochromator, adjustable crossed slits collimator, and gas-proportional detector. The XRD measurements performed included ω-2θ scans and two-axis reciprocal space maps of the 002 and 113-type reflections. For an ω-2θ scan, the step size in 2θ is twice that of ω, which results in the scattering vector Q scanning radially from the origin at the sample surface in reciprocal space, as illustrated in Figure 2.9 (a) and (b). A ω-2θ scan is a 'symmetrical' scan when the angle of incident X-ray beam (ω) is equal to the angle of the diffracted beam (θ), and the scattering vector Q scans in the direction normal to the sample surface, as shown in Figure 2.9 (a). For the case where $\omega \neq \theta$, as in Figure 2.9 (b), the ω-2θ scan is an 'offset' scan and is collected in asymmetrical geometry, where the difference $\omega - \theta$ is the offset

angle, *o*. An area of reciprocal space can be investigated by performing ω-2θ scans for a series of offset angles to produce a two-axis reciprocal space map, which is usually plotted as a colour intensity map with Q_x and Q_z axes to represent the reciprocal space lattice vectors that are parallel and normal to the surface of the sample.

Figure 2.9 (c) is an example of a schematic cross-section of the reciprocal space lattice of a (001)-oriented zincblende crystal, showing the relative positions of the 002, 113 and 111-type reflections. Q_x and Q_z represent the reciprocal space lattice vectors that are parallel and normal to the surface of the sample, which are the [110] and [001] directions respectively in the example shown. While the 002 reflection is on the Q_z axis and can be accessed with a symmetrical scan, the 113-type reflections are off the Q_z axis and are acquired with offset scans.

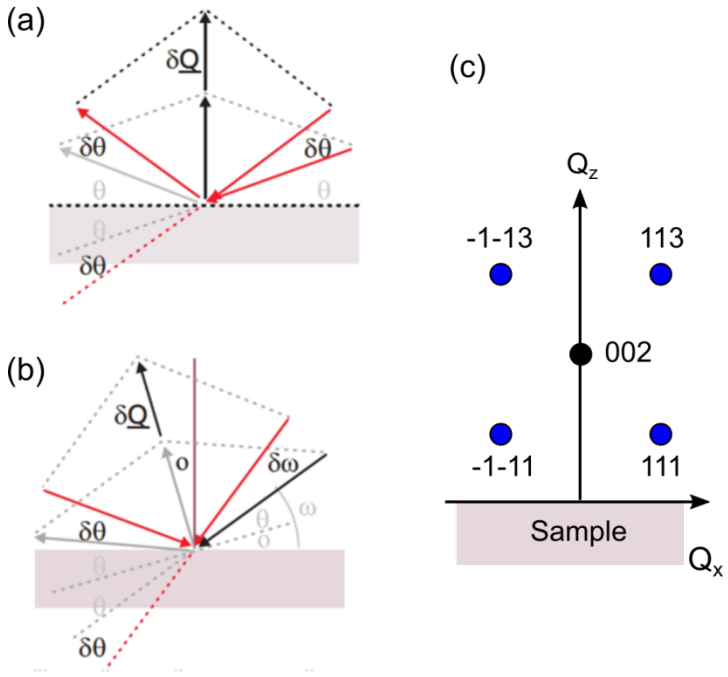

Figure 2.9 ω-2θ scans collected in (a) symmetrical and (b) asymmetrical geometry. Figures (a) and (b) are reproduced from [67], with the permission from P. Kidd. (c) Schematic cross-section of the reciprocal space lattice of a (001)-oriented zincblende crystal. Q_x and Q_z represent the reciprocal space lattice vectors that are parallel and normal to the surface of the sample.

2.3.2.1 Phase purity

The phase purity of our zb-GaN samples were determined from reciprocal space maps of the 113 zb-GaN reflection and the nearby 1-103 wz-GaN reflection with their stacking fault related intensity streaks collected in asymmetric geometry. These intense reflections were chosen, since they are relatively close by each other and do not

superimpose with unwanted diffuse scattering from surface features that arises from low incident beam angles of ~2° to the sample surface. Figure 2.10 shows examples of such reciprocal space maps taken from two samples with (a) a relatively high phase purity, and (b) a significant amount of wurtzite inclusions. Each of the maps contain a 113 zb-GaN peak, a 113 3C-SiC substrate peak and stacking fault streaks along the <111> type directions, as labelled; while the 1-103 wz-GaN peak is only present in the sample with wurtzite inclusions (Figure 2.10 (b)).

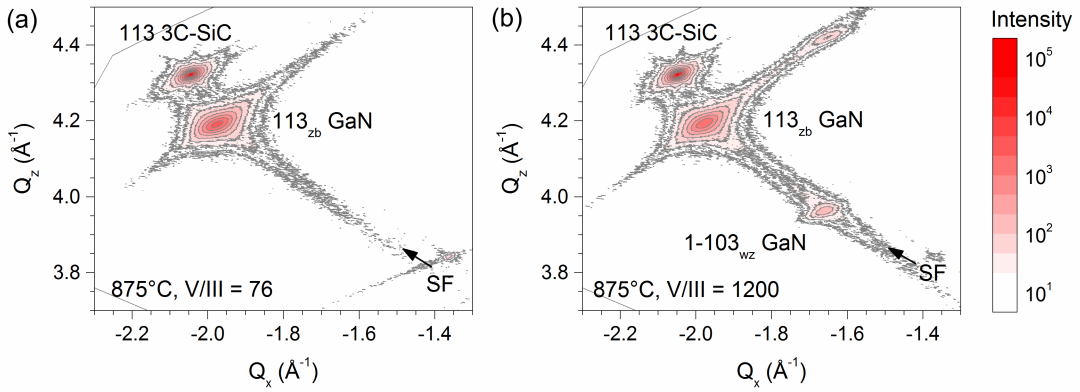

Figure 2.10 Reciprocal space maps of the 1-103$_{wz}$ and 113$_{zb}$ reflections for samples grown on a 4° miscut substrate at 875°C and a V/III-ratio of (a) 76, and (b) 1200, with (a) a relatively high phase purity, and (b) a significant amount of wurtzite inclusions. Figures from Dr Martin Frentrup.

Subsequently, the intensity profiles along the streaks (Q ∥ [111]) were extracted from the reciprocal space maps, as present in Figure 2.11 (a) and (b). Pseudo-Voigt functions for the zincblende and wurtzite phases were fitted to the intensity profiles at the theoretical positions of ~ 4.03 Å^{-1} and ~ 3.64 Å^{-1}, respectively. A third Pseudo-Voigt function was fitted in between the zincblende and wurtzite fits to consider the contributions from highly defective zb-GaN regions, containing bunches of stacking faults. As the integrated intensities of these fits is proportional to the material volume of each phase [58], these were then used to quantify the proportion of each phase.

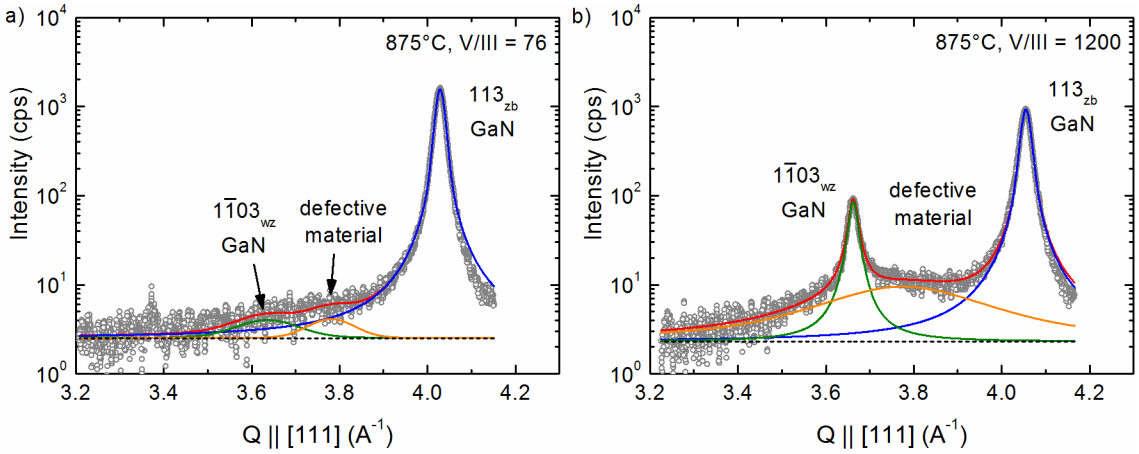

Figure 2.11 XRD intensity profile through the 1-103$_{wz}$ and 113$_{zb}$ reflections (grey circles) for the samples grown on a 4° miscut substrate at 875°C and a V/III-ratio of (a) 76, and (b) 1200, with (a) a relatively high phase purity, and (b) a significant amount of wurtzite inclusions. Pseudo-Voigt fits for the zb-phase (blue), wz-phase (green), and defective zb-GaN material (orange) were used to estimate the phase fractions. Figures from Dr Martin Frentrup.

2.3.2.2 Strain measurements

When a GaN film is deposited on a 3C-SiC/Si substrate, the film is likely to experience a biaxial in-plane strain, due to lattice and thermal mismatch between the film and the substrate. The biaxial in-plane strain is accompanied by an out-of-plane strain.

The ω-2θ scan of the 002 3C-SiC and zb-GaN reflections for a sample is obtained, and Gaussian curves are fitted for each reflection, with the 3C-SiC reflection used as a reference. The 2θ value of the zb-GaN reflection is extracted and the d_{002} spacing, or half of the out-of-plane lattice constant for a (001)-oriented GaN film, $a_{\perp\, GaN}$, is calculated using Bragg's law.

$$d_{002} = \frac{\lambda}{2sin\theta}$$

$$a_{\perp\, GaN} = 2 \times d_{002}$$

The out-of-plane strain, $\varepsilon_{\perp\, GaN}$, is determined from the out-of-plane lattice constant $a_{\perp\, GaN}$ and the lattice constant for relaxed zincblende GaN $a_{0\, GaN}$, which is 4.50597 Å [58]:

$$\varepsilon_{\perp\, GaN} = \frac{a_{\perp\, GaN} - a_{0\, GaN}}{a_{0\, GaN}}$$

Since the stress experienced by the film from the lattice mismatch to the substrate

is parallel to the GaN/SiC interface, we assume that the film is stress-free in the [001] growth direction. If we also assume that the in-plane strain is equal along the two in-plane directions, the bi-axial in-plane strain, $\varepsilon_{\parallel GaN}$, is given by Hooke's law:

$$\varepsilon_{\parallel GaN} = -\frac{1}{2}\frac{C_{11}}{C_{12}}\varepsilon_{\perp GaN}$$

where C_{11} and C_{12} are the materials' elastic constants, and are 293 GPa and 159 GPa for zb-GaN respectively.

2.4 Transmission electron microscopy (TEM)

In a transmission electron microscope (TEM), a beam of electrons is typically accelerated to velocities 50 – 80 % the speed of light by a voltage between 100 kV and 400 kV, and is directed towards a sample. The electrons interact with the sample and generate various signals which we can select and detect with the TEM. The sample needs to be electron transparent, i.e. typically thinner than 200 nm, hence sample preparation is essential for TEM.

2.4.1 Theoretical resolution

The resolution of a light or electron microscope can be defined by the Rayleigh's criterion for the diffraction limit:

$$d = \frac{1.22\,\lambda}{2\,n\,\sin\alpha}$$

where d is the resolution, λ is the wavelength of the photons or electrons, n is the refractive index of the medium through which the photons or electrons travel through, and α is the collection semiangle of the lens. Since $n\,sin\alpha$ is a constant for a particular imaging system, it is commonly referred to as the numerical aperture of the system. Hence from the equation, the resolution of a microscope is limited by the wavelength of the photons or electrons. For a light microscope, the highest resolution achievable is ~ 260 nm with a wavelength λ = 400 nm. Therefore, a light microscope is not able to resolve in the nanometre scale, or nanoscale defects in nitride semiconductors in our case.

When electrons are accelerated by voltages in the range 100 kV – 400 kV, wavelengths less than that of visible light can be achieved. At such accelerating voltages, the velocities of the electrons reach 50 % - 80 % the speed of light. Hence the wavelength of such electrons, taking into account relativistic effects, is given by:

$$\lambda = \frac{h}{\sqrt{2m_0eV(1 + \frac{eV}{2m_0c^2})}}$$

where h is the Planck's constant, m_0 is the rest mass of the electron, e is the elementary charge, V is the accelerating voltage and c is the speed of light in vacuum.

The transmission electron microscopes used for the work in this thesis have operating voltages of 200 kV - 400 kV, which correspond to relativistic electron

wavelengths of 1.64 pm to 2.51 pm, and theoretical resolutions on the order of 1 pm.

In practice, the resolution of a TEM is in fact limited by the aberrations of the electromagnetic lenses of the instrument, including spherical and chromatic aberrations and astigmatism. The typical resolution of the TEMs used in this thesis is ~ 0.2 nm for bright-field TEM and ~ 0.1 nm for scanning TEM (STEM).

2.4.2 Electron-sample interaction

When the accelerated electrons are directed at a thin sample in a TEM, they can be scattered elastically with almost no loss of energy through the interaction with the nuclei of the atoms of the sample, or scattered inelastically with some loss of energy by interacting with the electron cloud of the atoms. The TEM modes used in this thesis are based on elastically Bragg- and Rutherford-scattered electrons. Figure 2.12 illustrates the relative positions of the direct beam which is parallel to the incident beam, and the Bragg and Rutherford-scattered electrons.

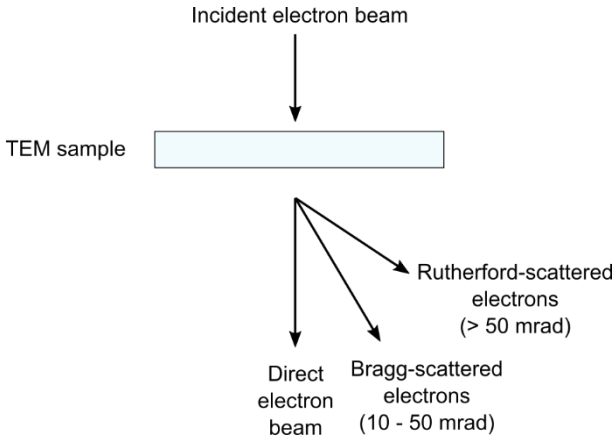

Figure 2.12 Elastically scattered electrons from a crystalline TEM sample. Figure adapted from Massabuau [87].

2.4.2.1 Diffraction or Bragg scattering

Similar to X-rays, electrons can be diffracted or Bragg scattered by a crystalline material. Bragg scattering of a crystalline material in a TEM can be described by Bragg's law:

$$|\boldsymbol{g}| = \frac{2\sin\theta_B}{\lambda}$$

where $\boldsymbol{g} = \boldsymbol{k}_D - \boldsymbol{k}_I$, $\boldsymbol{k}_I$ and $\boldsymbol{k}_D$ are the k-vectors of the incident and diffracted

waves respectively, and $|\boldsymbol{g}| = \frac{1}{d}$. Figure 2.13 illustrates Bragg's law, where the incident beam is diffracted from a set of planes with spacing *d* to result in a diffracted beam G, at an angle of 2 θ_B from the direct beam O. The additional diffraction spots *n*G, where $n \neq 1$, arise from planes with spacing *nd*.

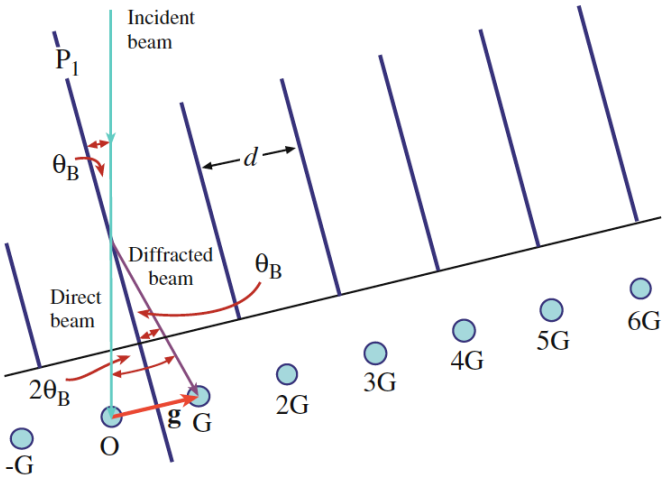

Figure 2.13 Bragg scattering of a beam of electrons from a set of crystal planes with spacing *d*. Figure reprinted by permission from Springer Nature: [89, p. 202].

The reciprocal space lattice of a crystal represents the possible positions of the diffraction spots, similar to X-ray diffraction. An Ewald sphere construction in reciprocal space, where the sphere has radius of $\frac{1}{\lambda}$ and crosses the origin of the reciprocal space lattice of the crystal, can be used to determine the possible planes that satisfy the Bragg condition. An example is shown in Figure 2.14 (a) and the Bragg condition is satisfied where the Ewald sphere intersects with the reciprocal space lattice, such as spot B in red. For the case in a TEM (Figure 2.14 (b)), the Bragg condition can be satisfied for many planes at a time, since λ and the Bragg angles θ_B of the diffracting planes are small, and the radius of the Ewald sphere is large. Moreover, the thin TEM samples result in the elongation of reciprocal lattice points into rods along the direction of the sample normal. Thus the Ewald sphere can intersect with a large number of rods, resulting in the relaxation of the Bragg condition and a TEM diffraction pattern consisting of a number of spots.

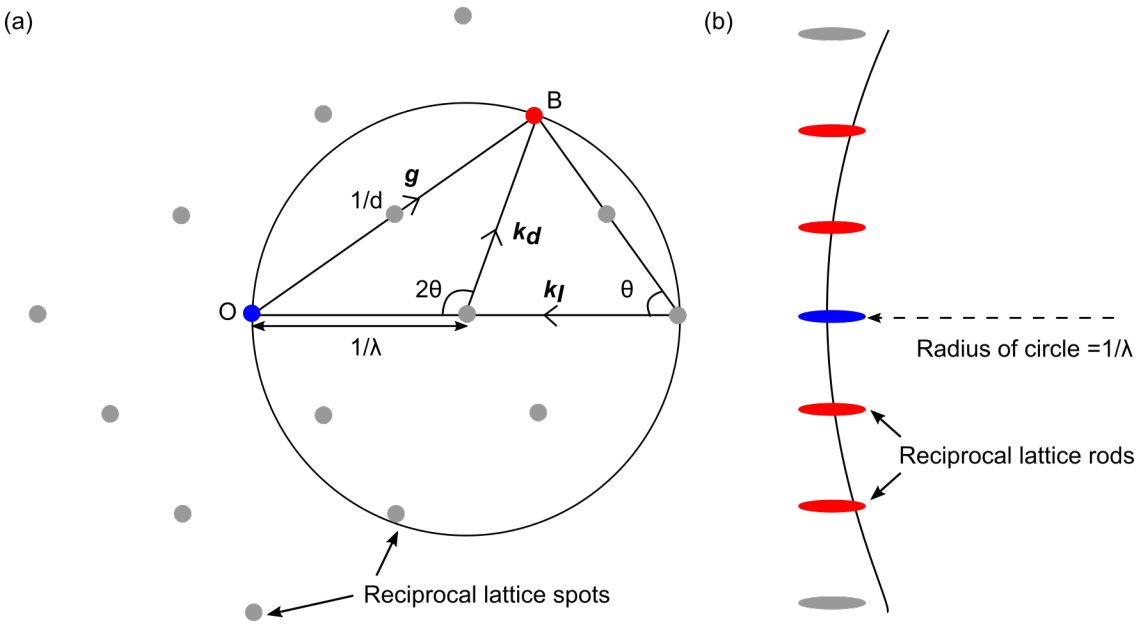

Figure 2.14 (a) Construction of an Ewald sphere in 2D. The Bragg condition is satisfied for the reciprocal lattice spots that touch the Ewald sphere, such as spot B in red. The k-vectors of the incident and diffracted waves ($\boldsymbol{k}_I$ and $\boldsymbol{k}_D$), $\boldsymbol{g}$ and θ are also labelled. (b) Ewald sphere construction for the case of TEM.

Even though the planes of a reciprocal lattice point may satisfy the Bragg condition, the structure factors of the crystal also need to be considered to determine the kinematically allowed and forbidden reflections:

$$F_{hkl} = \sum_i f_i \, e^{2\pi(hx_i + ky_i + lz_i)}$$

where *hkl* represents a reciprocal lattice point, and $\boldsymbol{r}_i = x_i \, \boldsymbol{a} + y_i \, \boldsymbol{b} + z_i \, \boldsymbol{c}$ is a vector defining the location of each atom within the unit cell of the crystal. A reflection is forbidden when the structure factor F is zero.

For fcc-based structures, such as zincblende, a reflection is allowed when *h*, *k* and *l* are all odd or all even, and forbidden when *h*, *k* and *l* are mixed odd and even.

The angle of Bragg scattered beams is low, typically between 15 mrad and 50 mrad (10 mrad is ~ 5°). Bragg scattered electrons are coherent, can provide information on the structure of material and are used for diffraction contrast (bright-field and dark-field) and high-resolution imaging.

2.4.2.2 Rutherford scattering

Rutherford scattering occurs when an incident electron is scattered by a nucleus of an atom. The scattering angle of the electron is more than 50 mrad, and is larger than that of Bragg scattered electrons. The Rutherford scattering cross-section, which

represents the probability that a scattering event will occur, is proportional to the square of the atomic number of the atom, Z^2. The Rutherford scattered electrons are incoherent, and are used in STEM imaging to provide *Z*-contrast imaging.

2.4.3 Sample preparation

The cross-sectional TEM samples investigated in this thesis typically consist of sandwiches of Si/SiC/GaN/Glue/GaN/SiC/Si. They are ground and polished to a thickness of less than 100 nm, and are mounted on a circular 3.05 mm-diameter Cu ring with a 2 mm-diameter hole. The process of preparing a TEM sample is described below, and a schematic of the final TEM sample is shown in Figure 2.15.

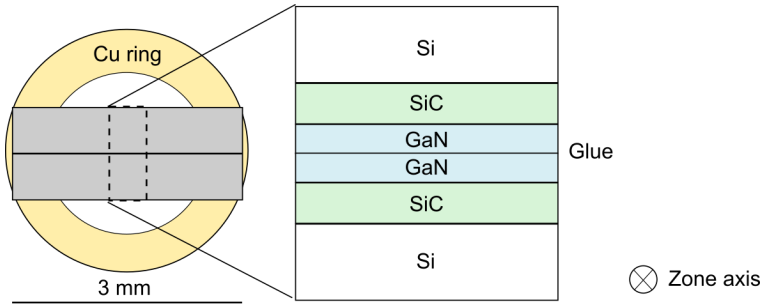

Figure 2.15 Schematic of a TEM sample.

A diamond saw is used to cut two pieces of the sample with dimensions 3 mm × 2 mm × thickness of the sample, where the 2 mm dimension is typically along the direction of the intended zone axis for the convenience of orienting the sample in the TEM.

The two pieces of samples are stuck together with epoxy glue, such that the GaN surfaces are in the middle of the sandwich and adjacent to each other. The two pieces are pressed together and rubbed against each other to ensure a thin glue layer that is free of air bubbles. The sample is placed on a hotplate to cure the glue at 130 °C for 45 minutes.

The sample is stuck to a grinding stub using a large dollop of thermoplastic wax that also covers and protects the sides of the sample. Care is taken so that the glue line is perpendicular to surface of the grinding stub, so that the zone axis of the sample will be as close to the intended one as possible after the grinding process.

Both of the wider cross-sectional surfaces of the sandwich are ground and polished manually, with successively finer grinding paper. Typically, the first surface is ground with SiC grinding paper with grit size P400 until the surface is flat, then it is polished

with diamond lapping films with grain sizes of 30 μm to 0.5 μm. The wax is then melted so that the sample can be flipped over to reveal the second surface. The second surface is ground with P400 SiC grinding paper to a sample thickness of 200 μm, then with P800 SiC paper to a thickness of 150 μm, and with P1200 SiC paper to 100 μm. A cotton wheel in a dimpler grinder is used to further decrease the sample thickness to 50 μm. The thickness of sample is regularly monitored with a light microscope, and can be estimated by the difference between the focal lengths of the sample surface and the grinding stub surface.

Epoxy glue is dotted onto the sides of the sample with a cocktail stick, and a circular Cu ring is placed on top of the sample. The glue is cured before the sample with Cu ring attached is removed from the stub by dissolving the wax away with acetone.

Finally, the sample is placed in a precision ion polishing system (PIPS), where two Ar^+ ion beams are directed towards a point of the sample, usually at the centre and close to the glue line. The sample is gently milled away by the Ar^+ ions, typically with a gun voltage of 5 keV and incidence angle of 7°, until colour fringes appear at the SiC layer. The gun voltage is then reduced to between 0.5 keV and 2 keV to clean the surface of the sample of debris from the higher energy ion milling.

2.4.4 Imaging

The microscopes used to perform the TEM work in this thesis include the FEI Tecnai F20 and the JEOL 4000 for bright-field and high resolution imaging, and the FEI Titan^3 for high resolution STEM imaging. In normal TEM mode, a parallel beam of electrons is used, while for STEM mode, the electrons are focussed to a probe.

2.4.4.1 Kikuchi lines and diffraction patterns

In a TEM, Kikuchi lines are useful in orienting a crystalline sample, while diffraction patterns are central to image formation.

Kikuchi lines arise from inelastically scattered electrons that travel at Bragg angle to the diffracting planes, where they are subsequently elastically scattered. Since the inelastically scattered electrons are scattered in all directions, they can diffract at all the possible diffracting *hkl* planes of the crystal to form a network of lines. Kikuchi lines form in pairs as electrons are scattered from the hkl and $\bar{h}\bar{k}\bar{l}$ planes. The Kikuchi lines remain fixed to the crystal as it is tilted, hence can be used to orient the TEM sample,

acting as a roadmap for tilting the sample from one zone to another. The Kikuchi map of an fcc crystal is shown in Figure 2.16 (a).

Typically, our TEM samples have been prepared such that the direction of the zone axis is along the thickness of the sample, but the direction might be slightly off due to the sample preparation process. The Kikuchi lines can be used get the sample exactly on to the zone axis.

Once the sample is exactly on the zone axis, a diffraction pattern consisting of the direct beam and spots corresponding to diffracting planes in that zone can be formed. Since our zb-GaN TEM samples have zone axes along <110>, an experimental diffraction pattern with zone axis = [-110] is included in Figure 2.16 (b). The indices of the first order diffraction spots are labelled.

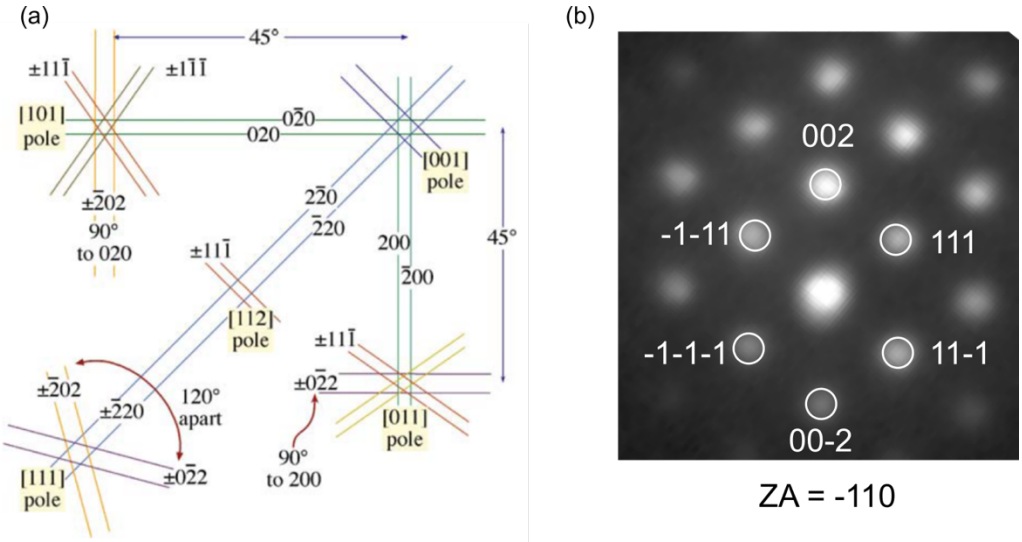

Figure 2.16 (a) Kikuchi map for a fcc crystal. Figure reprinted by permission from Springer Nature: [89, p. 315]. (b) Experimental diffraction pattern of a zb-GaN crystal with zone axis = [-110], with indices of the first order diffraction spots labelled. Image courtesy of Dr Lata Sahonta.

2.4.4.2 Diffraction contrast imaging

Diffraction contrast imaging makes use of the Bragg scattered electrons discussed in Section 2.4.2.1 to reveal structural information of a crystalline sample.

In bright-field imaging, the objective aperture in the TEM is used to select the direct beam of the diffraction pattern to form the image. Since the diffracted beams are not included in generating the image, the planes that diffract appear dark, while the parts of the sample that do not diffract appear bright. An example of a bright-field image is shown in Figure 2.17 (a)

As for dark-field imaging, the objective aperture is used to select one of the Bragg diffracted beams to form the image. The contrast is therefore reversed compared with a bright-field image, with bright diffracting planes and the non-diffracting parts of the sample appearing dark. Often the incident electron beam is tilted so that the diffracted beam is on-axis, since an off-axis beam is affected by aberrations of the lenses in the TEM. Such a configuration is the centred dark-field mode and an example image is shown in Figure 2.17 (b).

The contrast of bright and dark-field images can be improved by slightly tilting the sample away from the zone axis, along the band between a pair of Kikuchi lines associated with a *hkl* reflection, such that the desired $\boldsymbol{g}$ vector or *hkl* diffracted beam is strongly excited in addition to the direct beam. After tilting, the diffraction pattern usually appears as a row of spots ($\boldsymbol{g}$, $2\boldsymbol{g}$, $3\boldsymbol{g}$ etc) that is perpendicular to the *hkl* Kikuchi band.

Bright-field TEM has been used to image edge-on {111}-type stacking faults in zb-GaN in cross-sectional TEM samples with zone axes along <110> directions. A stacking fault translates the two parts of the crystal on either side of the fault by a relative displacement of $\boldsymbol{R}$. The $\boldsymbol{g}.\boldsymbol{R}$ analysis can be used to determine whether a defect is visible. [89, p. 424] If $\boldsymbol{g}.\boldsymbol{R}$ is zero or an integer, the defect is invisible; whereas if $\boldsymbol{g}.\boldsymbol{R}$ is non-zero or non-integer, the defect is visible. Stacking faults in fcc materials typically have $\boldsymbol{R}$ = 1/6 <112> or 1/3 <111>. [89, p. 420] We have found that the stacking faults are visible by exciting either the 111 type or 002 type diffraction spots, as shown in Figure 2.17 where (a), (c) and (d) were taken with $\mathbf{g}$ = 002, $\mathbf{g}$ = 111 and $\mathbf{g}$ = -1-11 respectively.

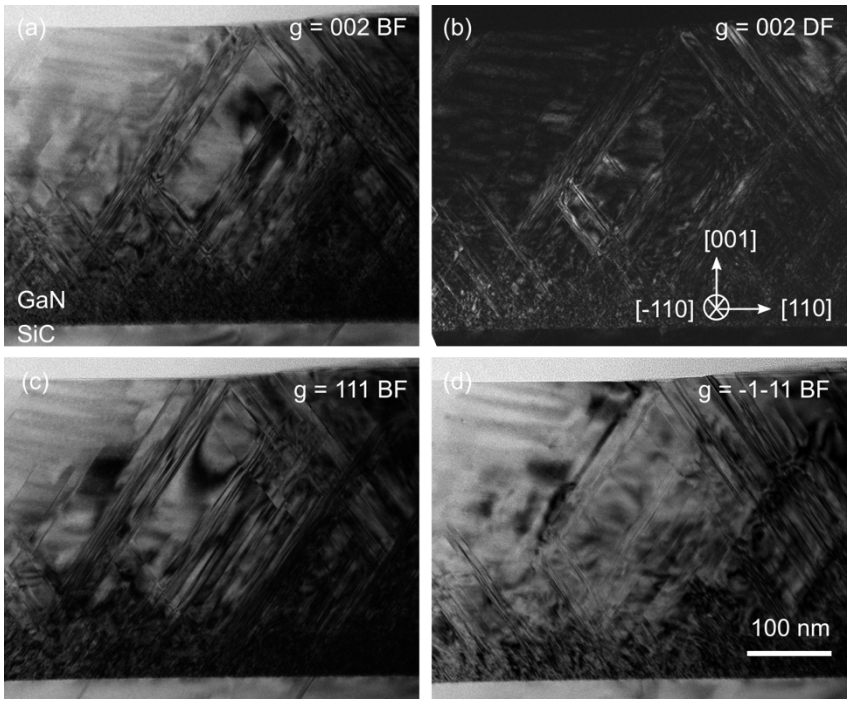

Figure 2.17 TEM images of a GaN epilayer with zone axis [-110] revealing the two inclinations of {111}-type stacking faults present in the zone. The imaging conditions are: (a) bright-field **g** = 002, (b) dark-field **g** = 002, (c) bright-field **g** = 111 and (d) bright-field **g** = -1-11.

2.4.4.3 Phase contrast imaging

In phase contrast imaging, also referred to as high-resolution TEM, the image is formed from the interference of the direct beam and one or more of the diffracted beams. As electrons are elastically scattered, their phase changes. Phase contrast in images arise due to the difference in phase between the direct and diffracted beams, and the interference between such beams.

When a diffracted beam ***g*** interferes with the direct beam, a set of lattice fringes normal to ***g*** is produced in the image plane. If several diffracted beams are allowed to interfere with each other and the direct beam, the sets of lattice fringes superimpose to result in an array of spots in the image plane. The lattice fringes or spots imaged can provide a picture of the periodicity of the crystalline sample, but *should not be directly interpreted as the locations of atomic planes or atoms*.

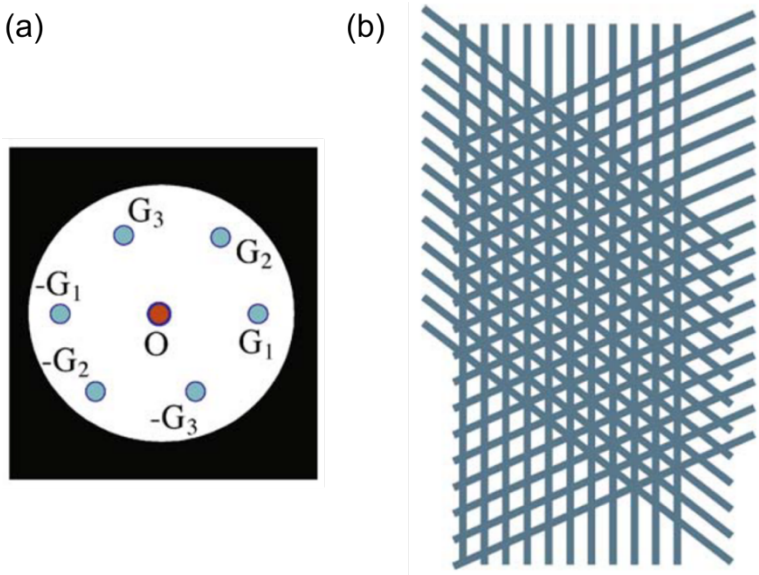

Figure 2.18 (a) Schematic of an objective aperture used to select the first order diffraction spots and the direction beam. (b) Schematic showing the sets of lattice fringes produced by each pair of diffraction spots (G and – G) in the image. The sets of lattice fringes are normal to ***g*** and superimpose to result in an array of spots. Figure adapted by permission from Springer Nature: [89, p. 391].

To achieve on-axis lattice fringe images, the TEM sample is tilted to a low index direction, which is <110> in our case, so that the atoms are arranged on top of each other and in columns. The objective aperture is used to select the first order diffraction spots, which interfere to form an image. The images are typically taken under the Scherzer defocus condition ($\Delta f = -1.2(C_s\lambda)^{0.5}$) to maximise the point resolution ($r = 0.66{C_s}^{0.25}\lambda^{0.75}$), where C_s and λ are the spherical aberration coefficient of the objective lens and wavelength of the electrons as defined by the accelerating voltage of the TEM. The Scherzer defocus for the Tecnai F20 operated at 200 kV (C_s = 1.22 mm, λ = 1.64 pm) is - 45 nm, and point resolution is 0.18 nm.

In this thesis, HRTEM images were used to identify stacking faults in the GaN layer in Chapter 7. The stacking faults interrupt the periodicity of the lattice and can be readily identified from an HRTEM image, hence the HRTEM images were interpreted intuitively without the simulation of images. With a higher resolution compared with bright-field images, stacking faults separated by a distance less than the resolution of bright-field images can be resolved in HRTEM images.

2.4.4.4 Z contrast imaging

Z contrast imaging can be achieved with high-angle annular dark-field scanning TEM (HAADF-STEM). The schematic of the HAADF-STEM system is shown in Figure 2.19. In STEM mode, the electron beam is focussed to a convergent probe as opposed to a parallel beam for normal TEM mode. As the electron beam is rastered across the sample, and the high-angle annular detector picks up any scattered electrons at each point of the scan. The intensity signal is displayed on a computer screen at each pixel of the scan. A high-angle annular detector, with collection angles between ~ 50 mrad and ~ 200 mrad, is used to intercept the Rutherford scattered electrons described in Section 2.4.2.2. Such electrons are scattered by more than 50 mrad, and their scattering cross-section is proportional to Z^2. Therefore atoms with higher atomic number have a higher probability of scattering and appear brighter than atoms with lower atomic number.

An advantage of STEM is that the formation of the image does not depend on lenses, and the resolution is limited by the probe size. For the aberration-corrected FEI Titan^3 S/TEM used for the STEM images in this thesis, a probe resolution of 70 pm can be achieved to allow atomic resolution. As a result of the image formation process, HAADF-STEM images are directly interpretable with atomic columns appearing bright.

In this thesis, high resolution HAADF-STEM images are used to image the atomic stacking of {111}-type planes in in zb-GaN, in order to identify defects such as misfit dislocations and stacking faults.

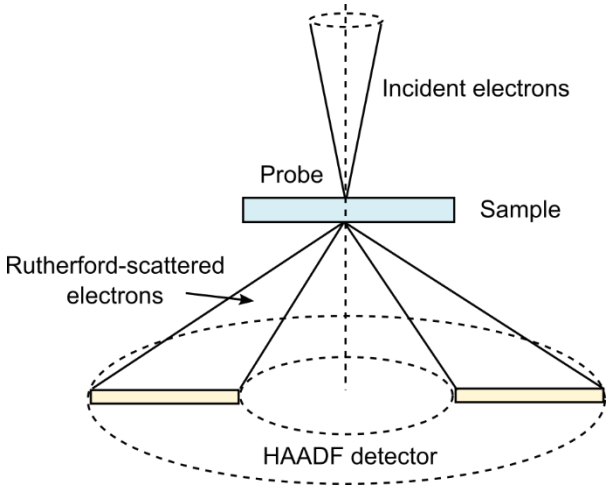

Figure 2.19 Schematic of the set-up of a HAADF-STEM system. The incident electrons are focussed to a probe that is scanned across the sample. The Rutherford-scattered electrons are collected by the HAADF detector, which has collection angles typically between 50 mrad and 200 mrad. Figure adapted from [90].

2.5 Photoluminescence (PL) spectroscopy

Photoluminescence (PL) spectroscopy is used to study the optoelectronic properties of semiconductor materials, such as GaN. A PL experiment involves optically exciting the sample by a laser to generate electron-hole pairs that can recombine radiatively. The emission energy and intensity of the recombination processes are then detected. This technique can be used to investigate the electronic states of the material that can trap the electrons and holes, and provide information regarding their concentrations. The various electronic states may result from impurities, intentional dopants and defects present in the material. The PL spectroscopy measurements in this thesis were performed by Stephen Church at 10 K in a temperature controlled closed-cycle helium cryostat, and exciting the samples with a continuous-wave 325 nm He-Cd laser.

A PL spectrum is a plot of intensity against photon energy of the detected radiative recombination. It typically consists of peaks and bands at various energies, which can be assigned to radiative recombination mechanisms by comparing with spectra from known samples or with theoretically predicted energies. A peak refers to a narrower region of the PL spectrum and is centred at a particular energy, while a band is a wider region of the spectrum and spans over a range of energies.

Three of the radiative transitions that commonly contribute to peaks or bands in PL spectra are described as follows:

(1) Free excitons

When an electron is optically excited to the conduction band by a photon from the laser, it leaves behind a hole in the valence band. The electron and hole pair can experience an electrostatic Coulomb attraction that bind them together to form an exciton. When the exciton decays, or when the electron and hole recombine, the energy released is slightly smaller in magnitude compared with the band gap of the semiconductor, due to the Coulombic binding energy between the electron and hole. Excitonic (X) emission is a type of near band edge emission.

(2) Bound excitons

Impurities and intentional dopants in a semiconductor material create electronic states within the band gap. A bound exciton arises when a free exciton described above is trapped by a donor or acceptor impurity or dopant. The decay of a donor-bound exciton

(D^0X) results in the recombination of an electron from the neutral donor level with a hole the valence band, while the decay of an acceptor bound exciton (A^0X) is the recombination of an electron from the conduction band with a hole in the neutral acceptor level.

(3) Donor-acceptor pair

Donor and acceptor impurities in a semiconductor material may form pairs. In a donor-acceptor pair (DAP), the electron and hole are bound to different impurities, and unlike an exciton, there is no Coulomb attraction between the electron and hole. After a DAP recombination, the donor and acceptor states become charged and there is a Coulomb attraction between the donor and acceptor impurities.

3 Structural characterisation of zb-GaN nucleation layers

3.1 Introduction

The nucleation stage plays an important role in ensuring epitaxial growth of zb-GaN. [21] However, only a handful of papers on the growth of nucleation layers (NLs) of zb-GaN is available in the literature, and the growth of zb-GaN in such studies is mostly by MBE. The most extensive studies on the nucleation of zb-GaN on GaAs (001) by MBE was performed by a group at Paul-Drude-Institut für Festkörperelektronik in Berlin [21,36,79,91]. The nucleation layers reported with the best structural qualities are epitaxial and crystalline, with the presence of misfit dislocations and stacking faults [79].

Most groups have adopted the use of low-temperature zb-GaN NLs, with growth temperatures reported between 550 °C and 630 °C for MBE and 550 °C for MOVPE, while subsequent epilayer growth occurred at higher temperatures between 620 °C and 850 °C for MBE [19,20,53,91], and between 850 °C and 950 °C for MOVPE [25,50]. Such a two-step growth procedure is widely used for the nucleation of wz-GaN on sapphire, where an anneal treatment results in the evaporation and re-deposition of the tops of predominantly zincblende as-grown islands as wz-GaN, while also eliminating faceting and misorientation of the islands. [92,93] The as-grown 0.5 monolayer thick NLs studied by Trampert *et al.* already forms an epitaxial zincblende layer, hence the reasons for the anneal treatment are not the same for zb- and wz-GaN. However, we have not been able to find studies in the literature that compares the growth of zb-GaN with and without a low-temperature NL to explicitly explain its use.

The influence of NL thickness on the morphology and phase purity of zb-GaN

epilayers grown on 3C-SiC (100) substrates by MOVPE was reported by Wu *et al.* [94]. It was found that for a GaN epilayer with a 20 nm thick NL, the epilayer islands were not coalesced and there was a higher wurtzite content than for a GaN epilayer with a NL that is more than 40 nm thick and coalesced islands.

We have also adopted the use of low-temperature NLs in our growth of zb-GaN. In this study, we determine an optimal GaN NL thickness for subsequent epilayer growth, by considering the coverage of the substrate by the NL, strain in the NL and the effect on epilayer growth. The NLs were annealed during heating to the growth temperature of the epilayer to study the effect of the temperature treatment on the NL morphology, substrate coverage, macroscopic strain, crystallinity and zincblende phase purity of the NLs. We also report on the effect of substrate miscut (4° and 2°) on the island formation of the NL.

3.2 Experimental methods

The GaN NLs were grown by Dr Menno Kappers by MOVPE in a 6 × 2'' Thomas Swan close-coupled showerhead reactor on ~ 2 × 2 cm^2 pieces of 150 mm diameter 3C-SiC/Si substrates provided by Anvil Semiconductors Ltd. The substrates consisted of ~ 3 μm thick layer of (001)-oriented 3C-SiC grown on a 1000 μm thick Si wafer with either 4° or 2° miscut towards the [110] in-plane direction. Laytec EpiTT emission-corrected optical pyrometry and three wavelength reflectance monitoring was used for in-situ metrology.

As-grown GaN NLs were grown with nominal thicknesses of 3 nm, 6 nm, 11 nm, 22 nm and 44 nm, which were calculated from the growth rate of 0.27 nm s^{-1}, as determined using the growth time and in-situ reflectance for a 130 nm thick NL test structure. The NL growth was carried out at a temperature of 600 °C, a V/III-ratio of 715, and a reactor pressure of 500 Torr. Two sets of samples were grown on the 4° miscut substrate: as-grown NLs, and annealed NLs by ramping the as-grown NLs to the epilayer growth temperature of 885 °C and subsequently cooling in an atmosphere of NH_3 and H_2. The same sets of as-grown and annealed NL samples were also grown on a 2° miscut substrate to study the effect of substrate miscut. To investigate the effect of NL thickness on the subsequent GaN epilayer, a set of 500 nm thick epilayer samples was grown on NLs with the different thicknesses on the 4° miscut substrate. The growth conditions of the epilayers were a growth temperature of 885 °C, a V/III-ratio of 150, and a reactor pressure of 100 Torr with a growth rate of approximately 0.5 nm s^{-1}.

The surface morphologies were measured using a Bruker Dimension Icon AFM in PeakForce mode for the NLs, and in tapping mode for the thicker epilayers. The fast scan direction for all samples was along the [110] miscut direction. The topographic data obtained from the AFM were analysed using the free software package WSxM [88]. The image height (H) is the height range from black to white in the AFM image, and is stated below each AFM scan.

The 2D-FFT method described in Section 2.2.5 was used to quantify the typical sizes of the surface features along [110] and [1-10], defined as $f_{[110]}$ and $f_{[1\text{-}10]}$ respectively. The directions [110] and [1-10] correspond to directions parallel and perpendicular to the miscut direction of the substrates. 500 × 500 nm^2 AFM scans were used for this analysis. The average feature size is determined from four measurements. The standard error of the mean from the four measurements was used to define the error bars of our measurements. The substrate coverage of the NLs was calculated from 500 × 500 nm^2 AFM scans using the software package Gwyddion [95], where the grains were selected using the 'mark grains by threshold' function and setting a height threshold which is typically ~ 25% of H.

For XRD characterisation performed by Dr Martin Frentrup, the method for determining phase purity is included in Section 2.3.2.1 while strain analysis using ω-2θ scans is discussed in Section 2.3.2.2. From the ω-2θ scan of the 002 zb-GaN and SiC reflections, the relative amounts of material deposited for different NLs were deduced from the integrated intensities of the GaN and SiC peaks. Nomarski optical microscopy performed by Dr Menno Kappers revealed the surface structure of the epilayer set of samples.

3.3 Results and discussion

3.3.1 As-grown NLs

The crystallinity of the as-grown NLs are revealed by XRD ω-2θ scans of the 002 zb-GaN and SiC reflections. A typical intensity profile of such a scan is shown in Figure 3.1, which was obtained from the 6 nm thick as-grown NL grown on the 4° miscut substrate. Such scans show that the NLs are crystalline with zincblende GaN (001) orientation. Reciprocal space maps of the nearby 10-11 wz-GaN reflection (not shown) reveal no significant intensity above the noise level, which suggests that the wurtzite

phase is absent or only present in very low concentrations below the detection limit.

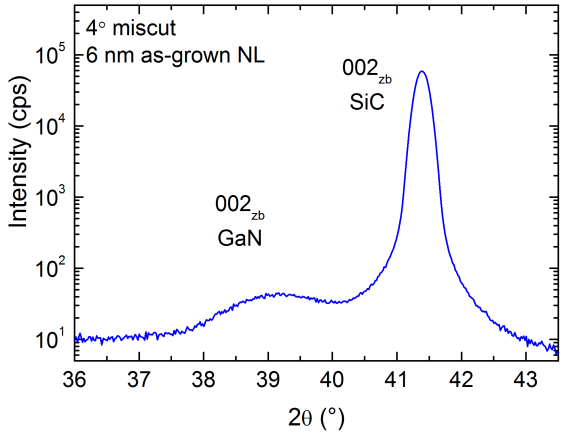

Figure 3.1 Intensity profile of the XRD ω-2θ scan of the 002 zb-GaN and SiC reflections for the 6 nm as-grown NL grown on 4° miscut substrate. Graph from Dr Martin Frentrup.

The variation in surface morphology of the zb-GaN NLs with layer thickness for the as-grown set of samples is shown in the 500 × 500 nm^2 AFM height scans in Figure 3.2. The surface morphology of all the NLs is characterised by merging islands elongated along the [1-10] direction. As the NL thickness increases from 3 nm to 44 nm, the AFM scans show that these surface features become slightly larger in both [110] and [1-10] directions, while the substrate coverage is similar.

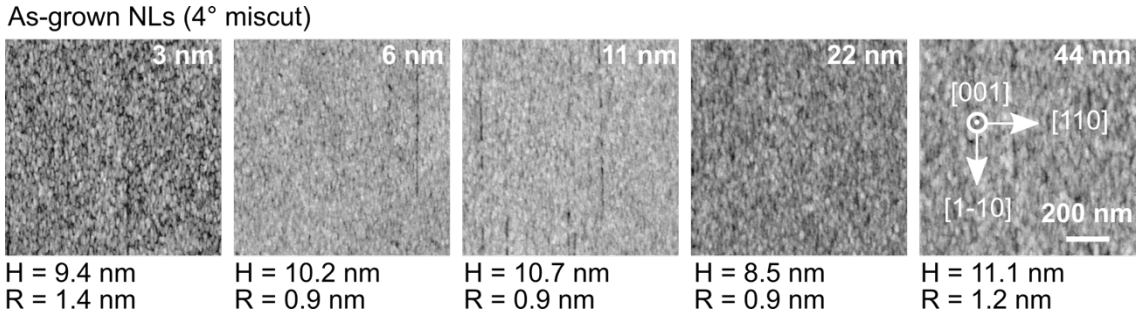

Figure 3.2 AFM height scans of the set of as-grown GaN NLs with different thicknesses revealing the surface morphology. The height (H) and rms roughness (R) are stated below each AFM scan.

The feature sizes in the [110] and [1-10] directions ($f_{[110]}$ and $f_{[1\text{-}10]}$) of the as-grown NLs on the 4° miscut substrate were quantified using the 2D-FFT method, and the results are shown by the filled circles and squares in Figure 3.3. The range of feature sizes in the [110] direction varied from 25 nm to 40 nm, while in the [1-10] direction the features are slightly larger between 35 nm and 65 nm. With increasing NL thickness, both $f_{[110]}$ and $f_{[1\text{-}10]}$ of the as-grown NLs increase slightly. Therefore, the AFM data shows that

the NLs are deposited as islands which coalesce with increasing material deposition, suggesting a three-dimensional Volmer-Weber type growth mode [96] which was also observed by Trampert *et al*. [79] and Daudin *et al*. [53].

The effect of the substrate miscut on the GaN feature size can be determined by comparing the feature size in the direction of miscut, $f_{[110]}$, for the NLs grown on 4° and 2° miscut substrates, which are denoted by the filled and open circles respectively in Figure 3.3. The data shows that the differences in feature sizes between the two miscuts are small and within the error bars of the measurements, indicating that miscut does not have an influence on size and shape of the islands.

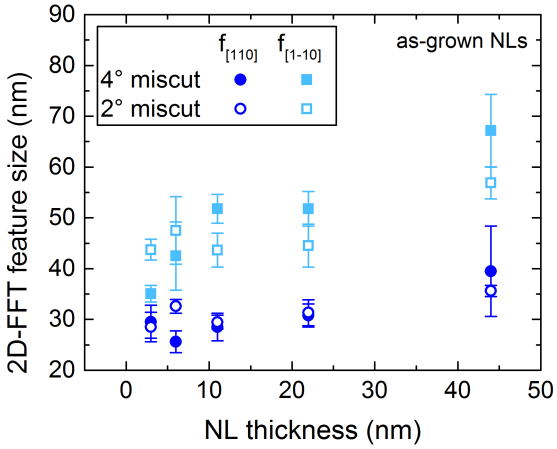

Figure 3.3 Feature sizes of the as-grown NLs grown on 4° (filled) and 2° (open) miscut substrates in the [110] (circle) and [1-10] (square) directions, as calculated by the 2D-FFT method.

The characteristic morphology of surface features elongated in the [110] direction of the GaN NLs is also found in subsequent epilayers grown on similar NLs, which will be reported in Chapter 5. The shape of such features are explained to be the result of anisotropic diffusion on the low-symmetry top monolayer of (001) GaN lattice, with the [110] and [1-10] directions going across and along the potential valleys of the GaN surface respectively. We note that for the epilayer samples, $f_{[110]}$ range from 0.6 µm to 1.3 µm, and $f_{[1\text{-}10]}$ from 1.0 to 4.8 µm, which are significantly larger than the features sizes of the NL samples. These differences in the scale are probably caused by the lower growth temperature for the NL, which results in shorter diffusion lengths.

3.3.2 Annealed NLs

The effect of an anneal treatment at the epilayer growth temperature of 885 °C on the as-grown set of NLs is revealed by the 500 × 500 nm^2 AFM height scans in Figure 3.4. The surface morphology of the NLs consists of features elongated in the [1-10] direction, similar to the as-grown NLs. It is evident that there is a reduction in surface coverage for the 3 nm, 6 nm and 11 nm NLs compared with the as-grown NLs in Figure 3.2. As the NL thickness increases from 3 nm to 44 nm, the surface coverage of the substrate increases as features become larger in both [110] and [1-10] directions and impinge on each other. For the thinnest NLs, the height (H) values in Figure 3.4 are large compared with the nominal NL thicknesses due to the formation of islands and reduction in substrate coverage upon annealing. It is also worth noting that the method of determining the nominal NL thickness from the growth rate is more inaccurate for the thinnest NLs than thicker ones.

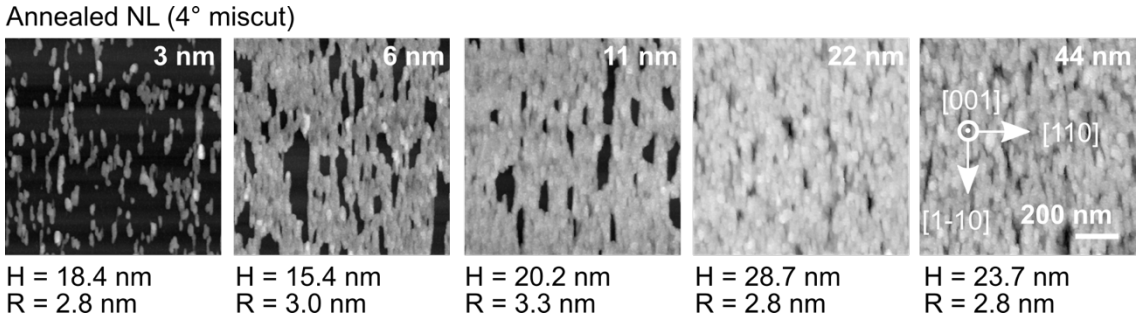

Figure 3.4 AFM height scans of the set of annealed GaN NLs with different thicknesses revealing the surface morphology. The height (H) and roughness (R) are stated below each AFM scan.

The feature sizes in the [110] and [1-10] directions of the annealed set of NLs grown on the 4° and 2° miscut substrate were quantified using the 2D-FFT method, as shown in Figure 3.5 (a). From the AFM scans, the surfaces of the 6 nm and 11 nm thick annealed NLs have a number of pits. This has resulted in the feature size obtained by the 2D-FFT method to be reflective of the size of the pits, rather than of the surface features. Hence the data points for 6 nm and 11 nm thick annealed NLs (within the dashed rectangle) should not be compared directly with the other data points in Figure 3.5 (a). The feature size in the [110] direction, $f_{[110]}$, increases slightly with increasing NL thickness, while in the [1-10] direction, $f_{[1\text{-}10]}$ does not differ significantly with NL thickness. Similar to the as-grown NLs, the data indicates that miscut does not have an influence on feature size. The aspect ratio ($f_{[1\text{-}10]}$/ $f_{[110]}$) of the features for the as-grown

and annealed NLs grown on the 4° and 2° miscut substrates is plotted in Figure 3.5 (b). The data points for 6 nm and 11 nm thick NLs have been taken out since $f_{[1\text{-}10]}$ and $f_{[110]}$ obtained from the 2D-FFT method do not reflect the actual feature sizes. There is a significant increase in the aspect ratio by a factor of 1.2 to 2 upon annealing, due to a larger increase in the feature size along [1-10] than [110], suggesting that the diffusion constants are anisotropic and higher along the [1-10] direction than the [110] direction.

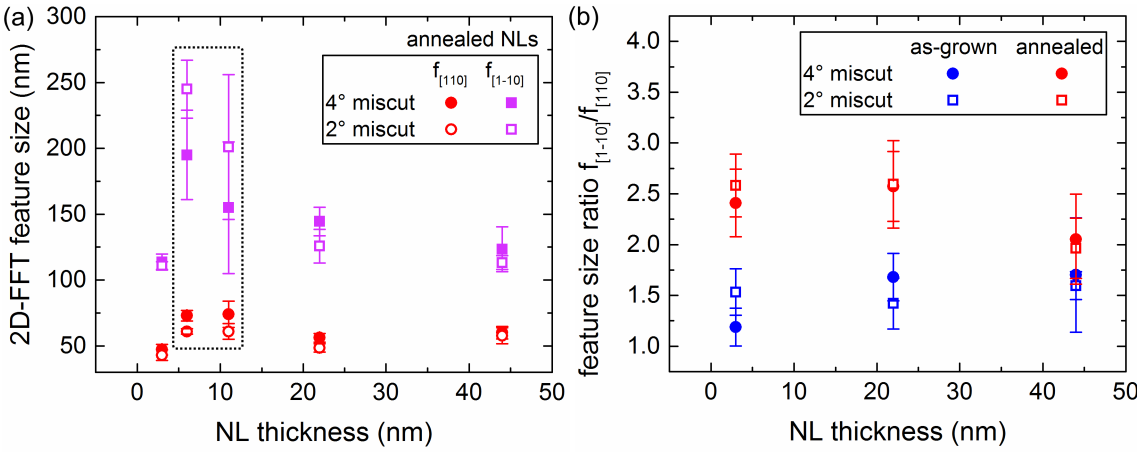

Figure 3.5 (a) Feature sizes of the annealed NLs grown on 4° (filled) and 2° (open) miscut substrates in the [110] (circle) and [1-10] (square) directions. The data points within the dashed rectangle are from samples where the 2D-FFT feature size measured reflects the sizes of the pits, and hence should not be compared directly with the other data points. (b) Variation of the aspect ratio of surface features with NL thickness for as-grown (blue) and annealed (red) NLs grown on 4° (filled) and 2° (open) miscut substrates.

Figure 3.6 shows the AFM scans of two annealed NLs that are (a) 3 nm and (b) 22 nm thick, and both grown on a 2° miscut substrate with the presence of antiphase domains, where neighbouring domains having surface features that are aligned along two perpendicular <110> directions. The anisotropic surface features are observed in both types of domains, and the elongation of the features is assumed to be along the potential valleys of each type of domain. This, together with the AFM scans in Figure 3.2 and Figure 3.4, demonstrate that the anisotropy of surface morphology starts at the nucleation stage. The characteristic morphology of surface features elongated in the [110] direction of the GaN NLs is also found in subsequent epilayers grown on similar NLs, and will be discussed further in Chapter 5.

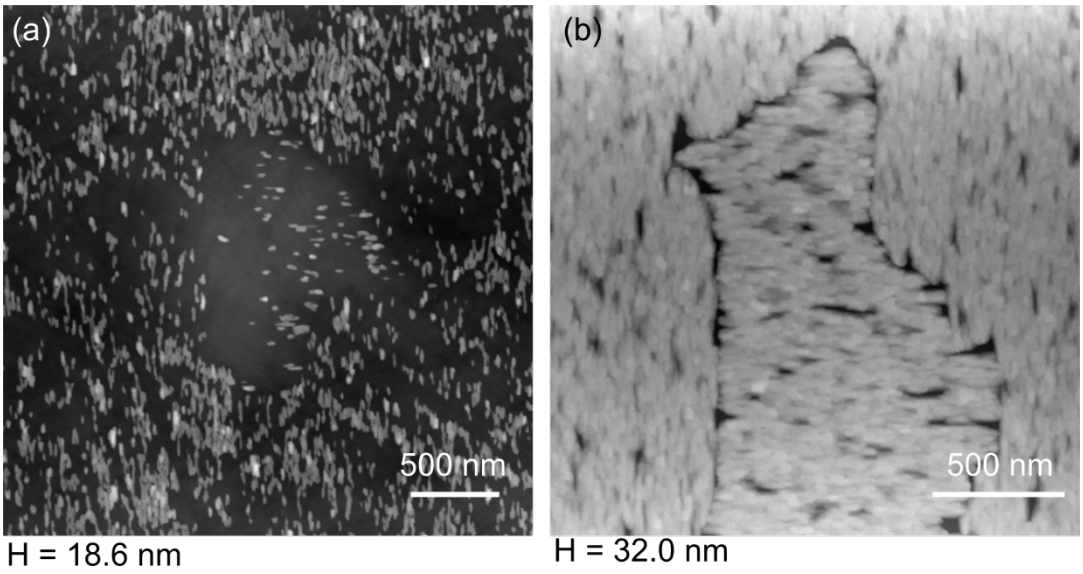

Figure 3.6 AFM height scans of annealed zb-GaN NL that are (a) 3 nm and (b) 22 nm thick, and grown on a 2° miscut substrate with antiphase domains. The height (h) is shown below each AFM scan. Data from Petr Vacek.

The coverage of the substrate by the NLs was determined from 500 × 500 nm^2 AFM scans for both the as-grown and annealed series of NLs grown on the 4° miscut substrate, as presented in Figure 3.7 (a). For the as-grown NLs, the SiC substrate is > 94 % covered by GaN even for a nominal thickness of 3 nm, and becomes fully covered (> 99 %) for thicknesses > 6 nm. Despite the reduced coverage at low thickness after the anneal treatment, the substrate coverage increases as the NL thickness is increased from 3 to 22 nm, at which point the substrate again becomes almost completely covered (> 99%).

The surface coverage observations by AFM is in agreement with XRD results from ω-2θ scans of the 002 reflections. In Figure 3.7 (b), the integrated intensity of zb-GaN reflection relative to the 3C-SiC substrate reflection is plotted against NL thickness for both the as-grown and annealed set of NLs in. The 3C-SiC substrate reflections have been used here to normalise the small experimental variations between the measurements of different samples. As the integrated intensity is proportional to the material volume of a thin sample [58], the ratio of the integrated intensities of the GaN/SiC reflections increases linearly with NL thickness, since there is an increasing volume of GaN deposited. The annealed NLs show a decrease in intensity compared with the as-grown NLs of the similar nominal thickness, revealing that material loss occurs during high temperature annealing. This material loss is relatively small and approximately the same for the thicker NL samples, suggesting that the degree of desorption is not as significant. However, the

material loss is large for the thinnest NL of 3 nm thickness, with a relative loss of 73% according to XRD, which fits well with the observation by AFM showing a relative reduction in the surface coverage of the same order (see Figure 3.7 (a)). Annealing of thinner NLs might result in more material desorption than thicker NLs because the former have less substrate coverage and the islands are not fully coalesced before annealing, hence the NL islands provide a larger surface area and sites for material desorption to take place.

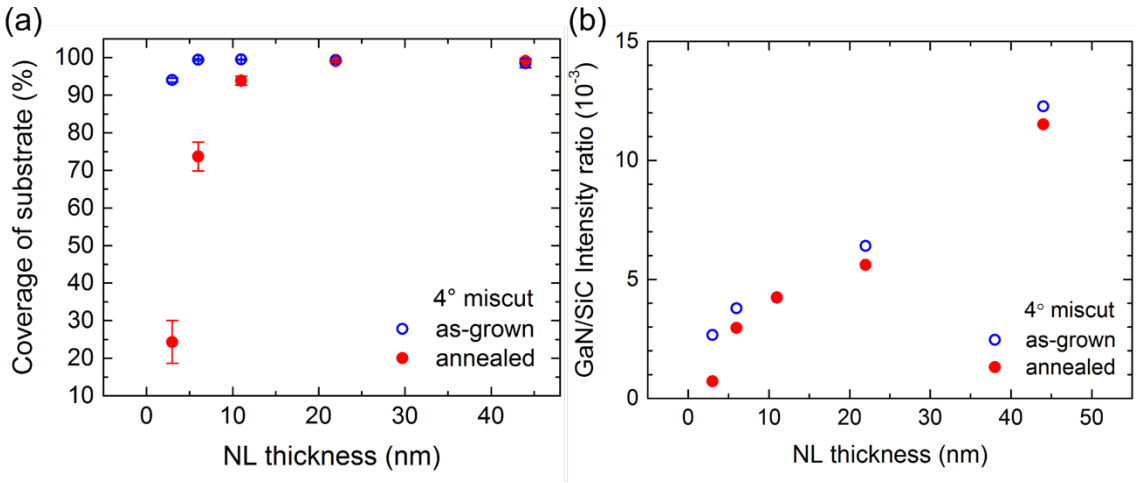

Figure 3.7 (a) Substrate coverage from AFM measurements and (b) ratio of integrated intensities of the 002 GaN and 3C-SiC reflections from XRD ω-2θ scans as function of the NL thickness for the as-grown and annealed sets of NLs grown on the 4° miscut substrate. Data from Dr Martin Frentrup.

To investigate the strain states of the NLs, the intensity profiles of the XRD ω-2θ scans of the 002 reflections for the annealed set of NLs grown on the 4° miscut substrate are compared in Figure 3.8 (a). The X-ray peaks of the thinnest GaN NLs are at lower Bragg angles than the Bragg angle of nominally unstrained zincblende GaN, which is indicated by the dotted line at 2θ = 39.9845(35)°. This shows that the GaN nucleation layers are stretched in growth direction and hence compressed parallel to the interface with SiC. With increasing NL thickness, the integrated intensity of zb-GaN reflection increases and the zb-GaN reflection steadily shifts towards higher Bragg angles, until it reaches the position of relaxed zb-GaN for a NL thickness of 44 nm. The bi-axial in-plane strain in Figure 3.8 (b) calculated from the peak positions of zb-GaN in the ω-2θ scans show that for both as-grown and annealed samples, the compressive in-plane strain reduces in magnitude with increasing thickness, from ~ -2×10^{-2} for the 3 nm thick NL to close to zero for the 44 nm thick NL. The thin NLs are compressively strained as zb-GaN has a larger lattice constant than 3C-SiC, and zb-GaN tries to matches the lattice

constant of SiC through elastic deformation. As the NL thickness increases, there is more plastic relaxation to result in a decrease in magnitude of the compressive in-plane strains. Misfit dislocations and stacking faults which facilitate plastic relaxation have been observed in such NLs, as will be shown in Chapter 4.

It can also be seen from Figure 3.8 (b) that the annealed NLs (filled circles) have a slightly smaller compressive in-plane strain than the as-grown NLs of similar thickness (open circles), even when the error bars are considered. This suggests that the anneal treatment results in relaxation of the material that is likely related to both the ripening of islands and material desorption, which is seen in the AFM data in Figure 3.2 and Figure 3.4, where the islands increase in size while the substrate coverage decreases after the anneal treatment. It is possible that the anneal treatment introduces pathways for vacancies to diffuse into the islands to form misfit dislocations, thus relaxing the material plastically. For 3 nm and 6 nm thick NLs, the annealed samples have significantly smaller compressive in-plane strains than the as-grown NL samples. Due to a low substrate coverage, the islands in the 3 nm and 6 nm annealed NLs may be less constrained parallel to the interface, thus possibly leading to more relaxation and lower in-plane strains. From Figure 3.8 (b), there is no obvious transition of the NLs from strained to unstrained state, hence it is not possible to determine a critical thickness of zb-GaN grown on 3C-SiC from the data.

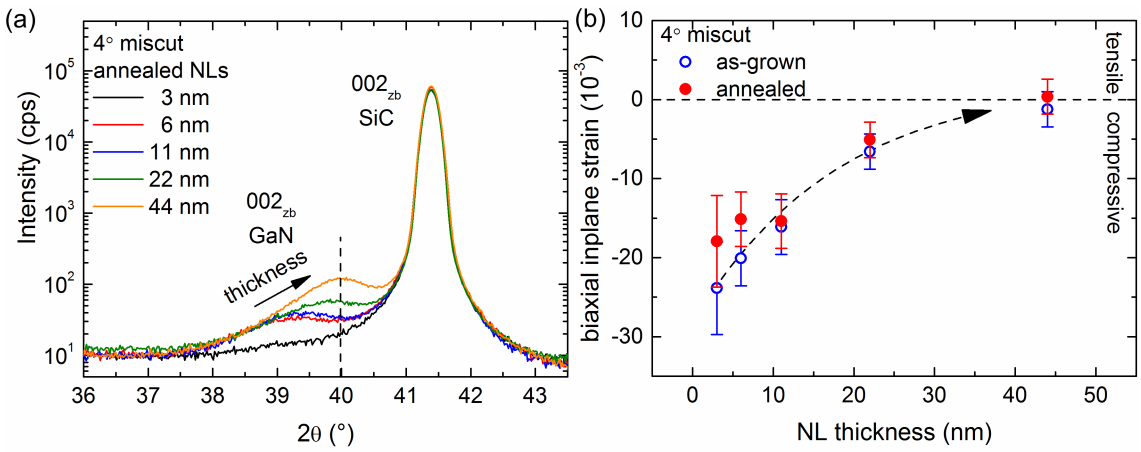

Figure 3.8 (a) XRD ω-2θ scans of the 002 zb-GaN and SiC reflections for the annealed NLs grown on the 4° miscut substrate. The dashed line marks the position of relaxed zb-GaN. (b) The trend line shows the change in bi-axial in-plane strain with increasing NL thickness of the as-grown and annealed sets of NL grown on the 4° miscut substrate. Graphs from Dr Martin Frentrup.

3.3.3 Effect of NL thickness on epilayer growth

Finally, we explore the properties of zb-GaN epilayers grown on NLs with different thicknesses. Nomarski optical micrographs of the zb-GaN epilayers grown on NLs with different thicknesses in Figure 3.9 (a) show that all the epilayers have a surface morphology with elongated features along the [1-10] direction, but the surface of the epilayer grown on the 3 nm thick NL has pits. Moreover, the phase purity analysis from XRD in Figure 3.9 (b) reveals that the epilayer grown on the 3 nm NL has the highest wurtzite content compared with thicker NLs. Referring to the AFM scans of the annealed set of NLs in Figure 3.4 and the substrate coverages determined from AFM and XRD data in Figure 3.7, the 3 nm annealed NL has the lowest substrate coverage of 26% of all the samples in the series. Therefore, we can conclude that an epilayer grown on NLs with a low substrate coverage of below at least 26% results in a pitted surface and a reduced zincblende phase purity. Wu *et al.* [94] did not observe the formation of a coalesced zb-GaN film for a NL thickness of 20 nm, whereas for the growth method applied here, a NL as thin as 6 nm provided sufficient surface coverage.

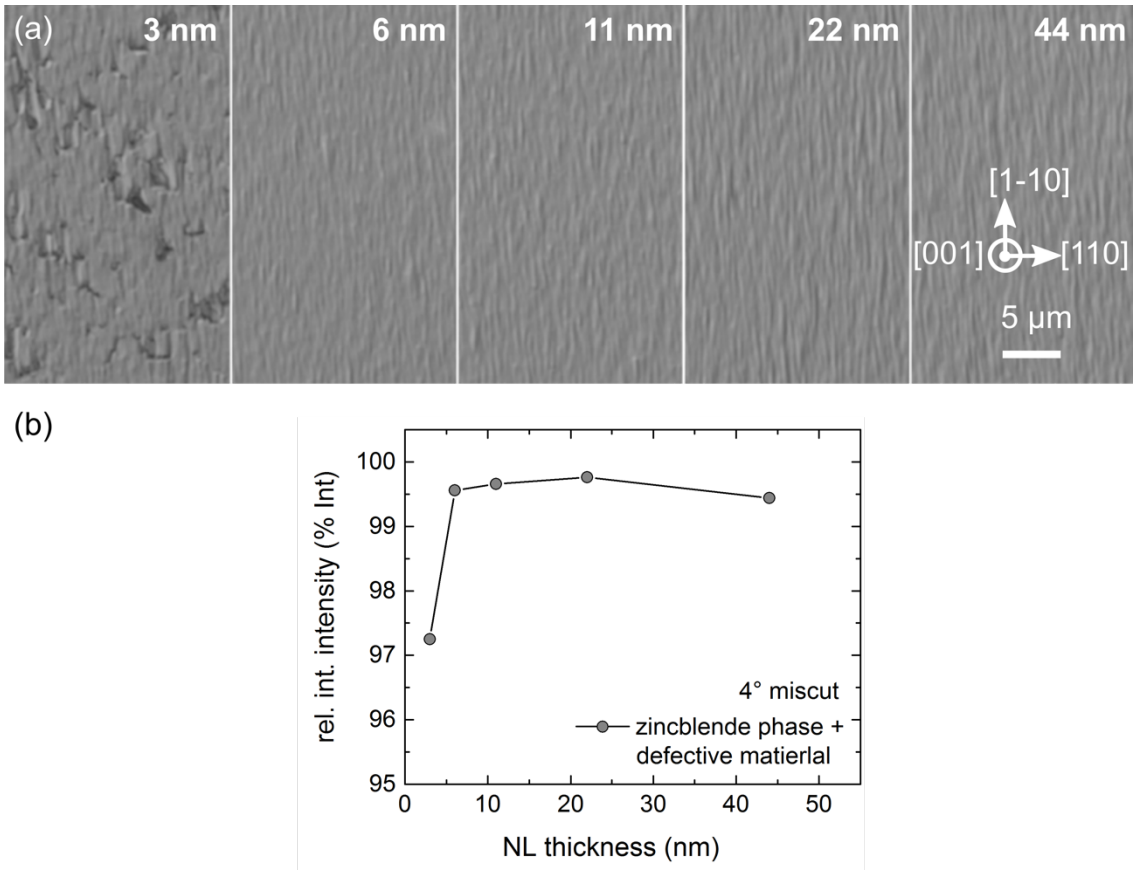

Figure 3.9 (a) Nomarski images of the GaN epilayers grown on NLs with different thicknesses. Images from Dr Menno Kappers. (b) The sum of the relative integrated intensity of zincblende phase and defective material peaks in the zb-GaN epilayers grown on NLs with different thicknesses, as determined by XRD. Data from Dr Martin Frentrup.

3.4 Conclusions

Both as-grown and annealed zb-GaN NLs with nominal thicknesses of 3 nm to 44 nm deposited on 3C-SiC/Si substrates by MOVPE are crystalline and have high zincblende phase purity. The miscut angle of the substrate (4° versus 2°) does not have an effect on the surface morphology of the NLs. The substrate coverage by the NL increases with NL thickness, while the annealing treatment of the NL to the higher epilayer growth temperature reduces the substrate coverage, especially for the thinnest NLs, due to material desorption and the ripening of islands. For full coverage (> 99 %) of the substrate, the nominal thickness of the annealed NLs should be > 22 nm. The substrate coverage of the NL is an important consideration as an incomplete coverage of the 3 nm thick annealed NL resulted in the subsequent epilayer having a pitted surface and a reduced zincblende phase purity. The minimum nominal NL thickness for the growth of zb-GaN films with high phase purity is 6 nm. The compressive bi-axial in-plane strain in the NLs reduces with increasing NL thickness (likely to arise from more

plastic relaxation by misfit dislocations and stacking faults), and after the anneal treatment due to relaxation from island ripening and material desorption. In light of such results, we recommend an optimal nominal NL thickness of 22 nm. Lastly, the study confirms that the anisotropy of surface morphology previously observed in zb-GaN epilayers starts at the nucleation stage and is controlled by the crystallography of the top monolayer of the (001) GaN lattice.

4 STEM investigation of zb-GaN nucleation layers

4.1 Introduction

In this chapter, we investigate the crystallinity of the GaN/SiC interface and the nature of defects in zb-GaN nucleation layers (NLs). The physical origin of the defects is also of interest: do the defects start at or away from the GaN/SiC interface, or at surface steps of the SiC substrate? Moreover, at which stage of growth do defects arise: before or after the coalescence of islands? Understanding the formation of defects could help us determine whether we can prevent or reduce their formation in the NL prior to the growth of an epilayer.

4.2 Experimental and analysis methods

The zb-GaN NLs studied here are three samples from the two as-grown and annealed series of NL samples grown on a 4° miscut substrate that were studied in the previous chapter. The three samples studied include: an as-grown 3 nm thick NL, an as-grown 22 nm thick NL, and an annealed 22 nm thick NL. Since the samples studied in this thesis typically have thicknesses of 22 nm, the combination of the three samples studied in this chapter provide snapshots of the different stages of growth for the NLs used, with the three stages exemplified being (1) early stage of NL growth, (2) NL after growth is completed, (3) NL after annealing.

The TEM samples were prepared by mechanical grinding and polishing, and thinned to electron transparency by precision ion polishing with Ar^+ ions by both myself and Petr Vacek. High-resolution STEM was performed using a FEI Titan^3 operated at 300

kV with Dr Fabien Massabuau. An average background subtraction filter (ABSF) was used to remove noise from the STEM images.

Identifying crystal defects from STEM images

Given the large number of STEM images to be analysed and that defects in the lattice are often not immediately clear to the eye, we used the following method to identify defects more readily. For an ABSF-filtered STEM image, such as Figure 4.1 (a) of the area surrounding the GaN/SiC interface, we used the software package Digital Micrograph to obtain its fast fourier transform (FFT) pattern (Figure 4.1 (b)). The sets of spots relevant to the (111) and (-1-11) planes are marked by the blue and red circles, respectively. By applying a mask to select one set of such spots and performing the inverse FFT function on the masked pattern, images such as Figure 4.1 (c) from the spots circled in red, or (d) from the spots circled in blue, are created.

An extra half-plane is identified by the red arrow in Figure 4.1 (c), where the white lines can be interpreted as the positions of the (-1-11) atomic planes and a break in a line indicates a half-plane. In the corresponding STEM image in Figure 4.1 (e), the red arrow marks the extra half-plane in the SiC layer and the white lines provide a guide to the eye of the positions of the surrounding (-1-11) planes. The two nearest neighbouring (-1-11) planes appear to bend around the extra half-plane. Since the extra half-planes terminate close to the GaN/SiC interface, we identify them as misfit dislocations that accommodate the lattice mismatch between GaN and SiC.

The white lines in Figure 4.1 (d) can be interpreted as the positions of the (111) planes. In the areas marked by the blue boxes, the white lines are not continuous but have breaks in them. The white lines also appear to be translated relative to each other along the [111] direction by about a third of the space between {111} planes. Referring to the original STEM image, the stacking of the (-1-11) planes is marked in Figure 4.1 (f). It shows the presence of two stacking faults, where the stacking sequence of the (111) planes is ABCBCABC instead of ABCABCABC for a perfect zincblende lattice. Hence we attribute features seen in the inverse FFT image in Figure 4.1 (c) to stacking faults in the [-110] zone.

Misfit dislocations and stacking faults are the two main defects in the zb-GaN lattice identified from the STEM images with the aid of the inverse FFT images. The origin and properties of these defects will be discussed in more detail in Sections 4.3.2

and 4.3.3.

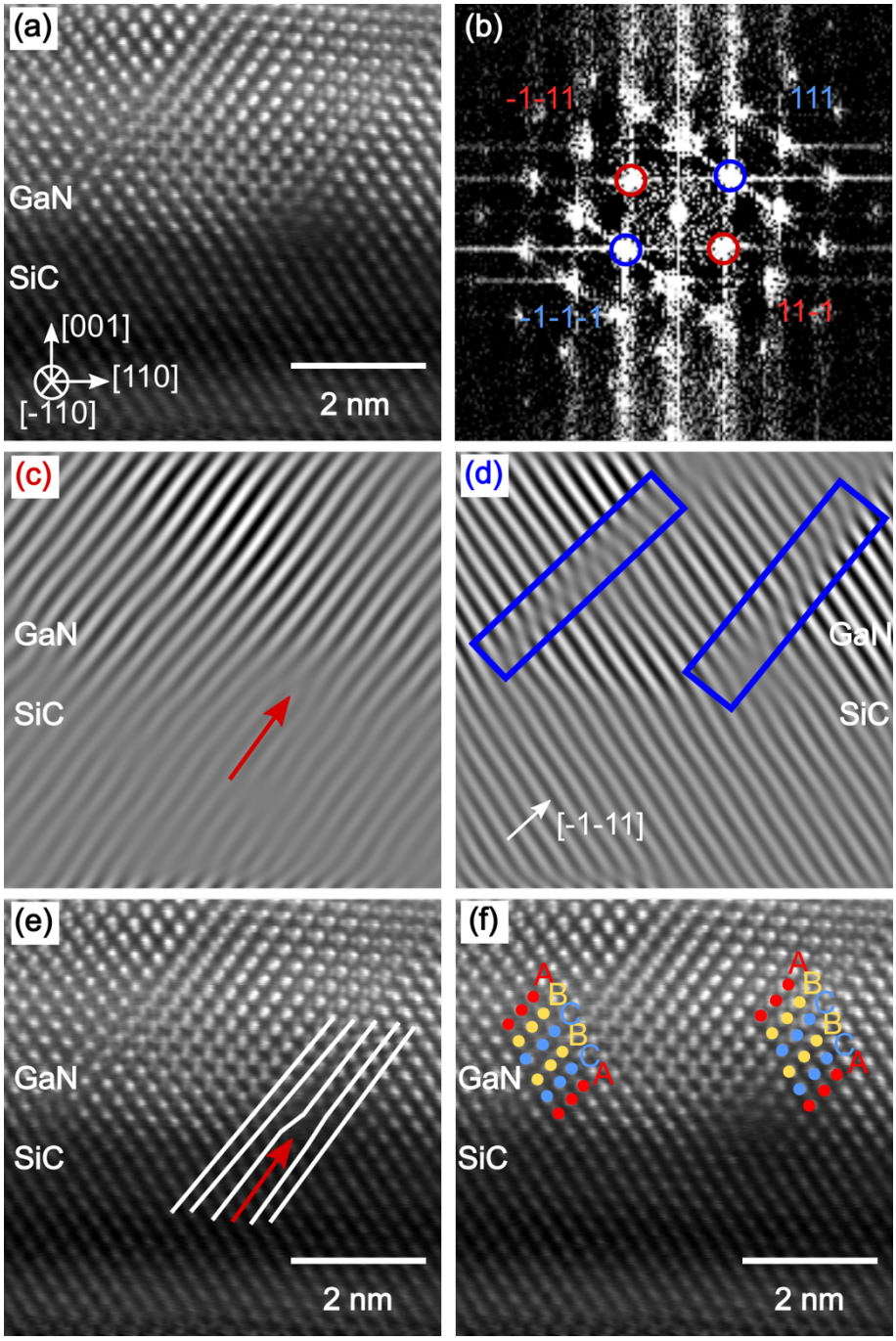

Figure 4.1 (a) STEM image with zone axis = [-110] of an area surrounding the GaN/SiC interface. (b) FFT pattern of the STEM image in (a). (c) Inverse FFT image of the filtered -1-11 and 11-1 spots circled in red in (b). (d) Inverse FFT image of the filtered 111 and -1-1-1 spots circled in blue in (b). (e) The misfit dislocation, or extra half-plane in SiC, is marked by the red arrow. The white lines provide a guide to the eye of the positions of (111) atomic planes. (f) The stacking of the (-1-11) planes close to the two stacking faults is marked by the different coloured circles and labels.

A third feature that commonly appears in our STEM images is the hexagonal pattern of atoms, as shown in the area within the blue circle in Figure 4.2 (a). It is

interesting to note that some of the atoms appear brighter than others. To explain the hexagonal pattern of atoms, we use schematics of projections of a lattice with an intrinsic stacking fault on the (1-11) plane. Figure 4.2 (b) shows such a projection of the lattice along the [110] zone axis, with ABCACABC stacking of the (1-11) planes, and the red and green regions signify atoms on either side of the stacking fault. When the lattice is rotated by 90° such that the projection is along the [-110] zone axis as in Figure 4.2 (c), the red atoms are now in front of the green atoms, creating a hexagonal pattern of atoms that is similar to that observed in Figure 4.2 (a). Hence we attribute the hexagonal pattern of atoms in the cross-sectional STEM images to stacking faults in the zone perpendicular to the zone axis of the STEM image.

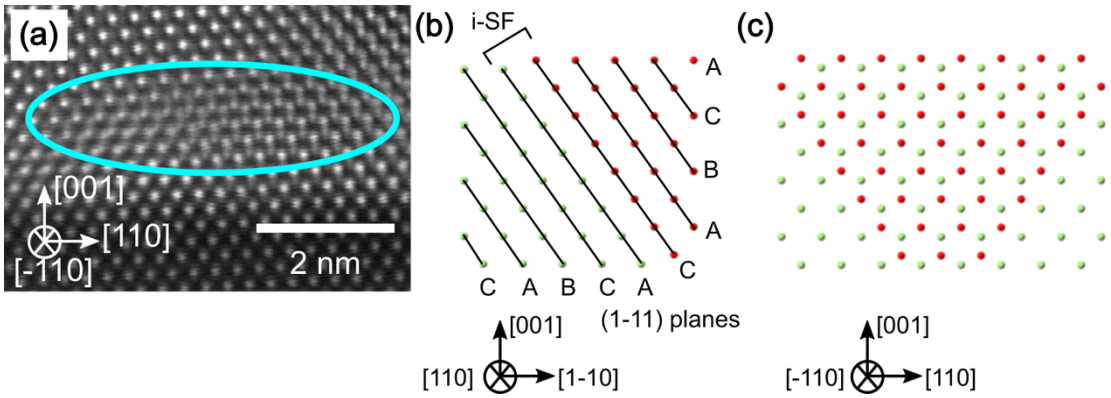

Figure 4.2 (a) STEM image with zone axis [-110] showing a stacking fault in the [110] zone. Schematic of the projection of an intrinsic stacking fault on the (1-11) plane in a zincblende lattice along the (b) [110] direction and (c) [-110] direction. Figures (b) and (c) are created by Petr Vacek.

4.3 Results

4.3.1 Crystallinity of zb-GaN nucleation layers

Since the GaN NL is grown at a lower temperature of 600 °C than the subsequent epilayer, there is a possibility that the as-grown NL is amorphous or polycrystalline prior to annealing treatment, as was observed by Paisley *et al.* [52]. In addition, as-grown nucleation layers of wurtzite GaN have been reported by Lorenz *et al.* [97] to consist of three-dimensional facetted islands that were highly misoriented with respect to each other and mainly of the zincblende phase. Annealing of the nucleation layers resulted in less misoriented islands and eliminated the faceting. To address the question of the crystallinity of the zb-GaN nucleation layers, we studied the 22 nm thick as-grown zb-GaN NL by cross-sectional STEM.

In the STEM image of the GaN/SiC interface of the 22 nm thick as-grown NL sample Figure 4.3, the two {111}-type planes in the [-110] zone, (-1-11) and (111), are marked by the white lines on the image. The ABCABC zincblende stacking of the {111}-type planes across the GaN/SiC interface are marked by the different coloured circles and labels. The GaN/SiC interface is crystalline and the {111}-type lattice planes in the SiC layer propagate into the GaN layer, with no observable amorphous layer. Moreover, from other STEM images such as Figure 4.4 of the 3 nm thick as-grown NL, the islands are oriented in the [001] direction and are not facetted even for as-grown NLs, in contrast to the wz-GaN NLs studied by Lorenz *et al.* [97].

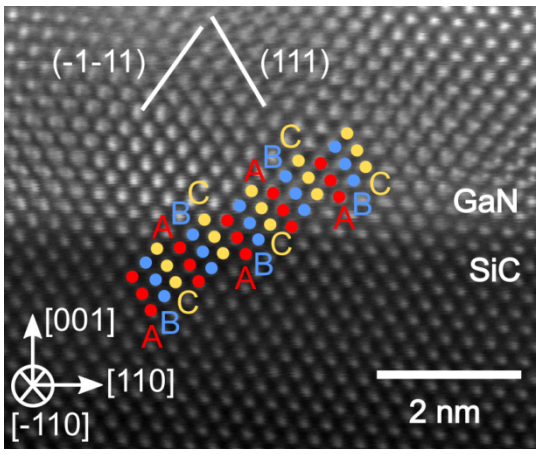

Figure 4.3 STEM image of the GaN/SiC interface of the 22 nm thick as-grown NL sample. Examples of the (-1-11) and (111) planes are shown by the white lines. The ABCABC stacking of the zincblende crystal structure in both the SiC and GaN layers is marked by the different coloured circles and labels.

4.3.2 Misfit dislocations

Misfit dislocations are labelled by red arrows in the STEM images of the as-grown nominally 3 nm thick zb-GaN NL in Figure 4.4. (Note that the nominal thickness of a NL represents an estimate of the average thickness of the layer, but the height of individual islands may fluctuate about this average.) The extra half-planes are found to terminate in the GaN NL close to the GaN/SiC interface, as marked by the arrowheads. A misfit dislocation could also generate a stacking fault where the extra half-plane in the SiC terminates, as shown by the blue box in Figure 4.4 (b). Since zb-GaN has a larger lattice parameter compared with 3C-SiC, the compressive strain in the GaN layer can be accommodated by the removal of a close-packed {111} half-plane in the GaN lattice to form an intrinsic stacking fault. (On the other hand, if the substrate had a larger lattice parameter than zb-GaN, the addition of an extra {111} half-plane in the zb-GaN lattice

to form an extrinsic stacking fault could accommodate the tensile strain in the GaN layer. Indeed, Trampert *et al.* [79] reported that for zb-GaN grown on GaAs, where GaAs has a larger lattice parameter than zb-GaN, a misfit dislocation consisted of an extra {111} half-plane in the zb-GaN lattice, resulting in an extrinsic stacking fault.)

The solid white lines in Figure 4.4 (a) and (b) trace out the approximate shapes of the islands, and the dotted white line in Figure 4.4 (b) indicates the likely position of a coalescence boundary between two neighbouring islands. Misfit dislocations are found to occur within an island (Figure 4.4 (a)), and potentially close to the coalescence boundary (Figure 4.4 (b)).

No clear surface steps of the substrate have been observed in the STEM images to suggest their involvement with the formation of defects.

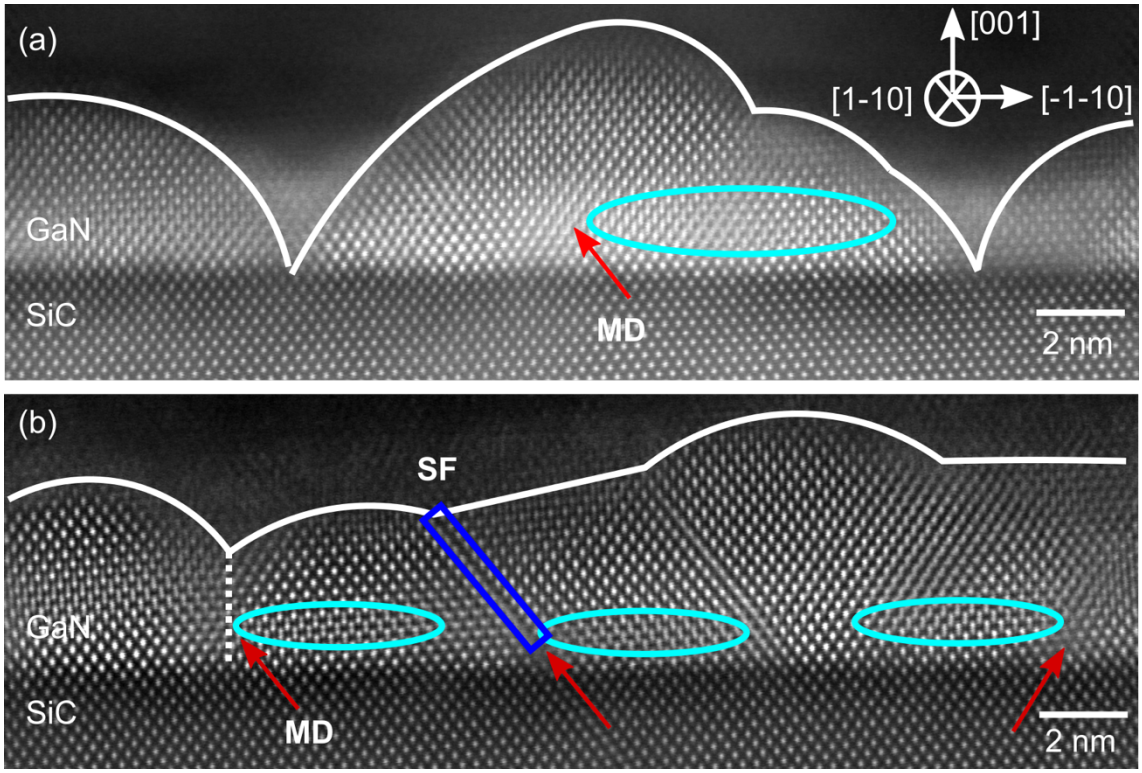

Figure 4.4 STEM images of the 3 nm thick as-grown zb-GaN NL. The solid white lines trace out the outline of the islands, while the dotted white line in (b) indicates a likely coalescence boundary between the two neighbouring islands. The misfit dislocations are marked by the red arrows, and a stacking fault is marked by the blue box.

We will discuss here three possible mechanisms for the formation of misfit dislocations: gap closure during the coalescence of islands, diffusion and agglomeration of vacancies, glide of dislocations from the free surfaces of the sample. The island coalescence model proposed by Gao *et al.* [98] considers the islands nucleated on the

substrate surface that grow and begin to impinge on each other. When two neighbouring islands grow until they are one atomic spacing apart (Figure 4.5 (a)), the edges of the islands snap together to leave an extra half-plane, or a misfit dislocation, in the substrate (Figure 4.5 (b)). In this model, a misfit dislocation and a stacking fault would be formed at the island coalescence boundary, as shown respectively by the red arrow and the stacking sequence in blue in Figure 4.5 (b).

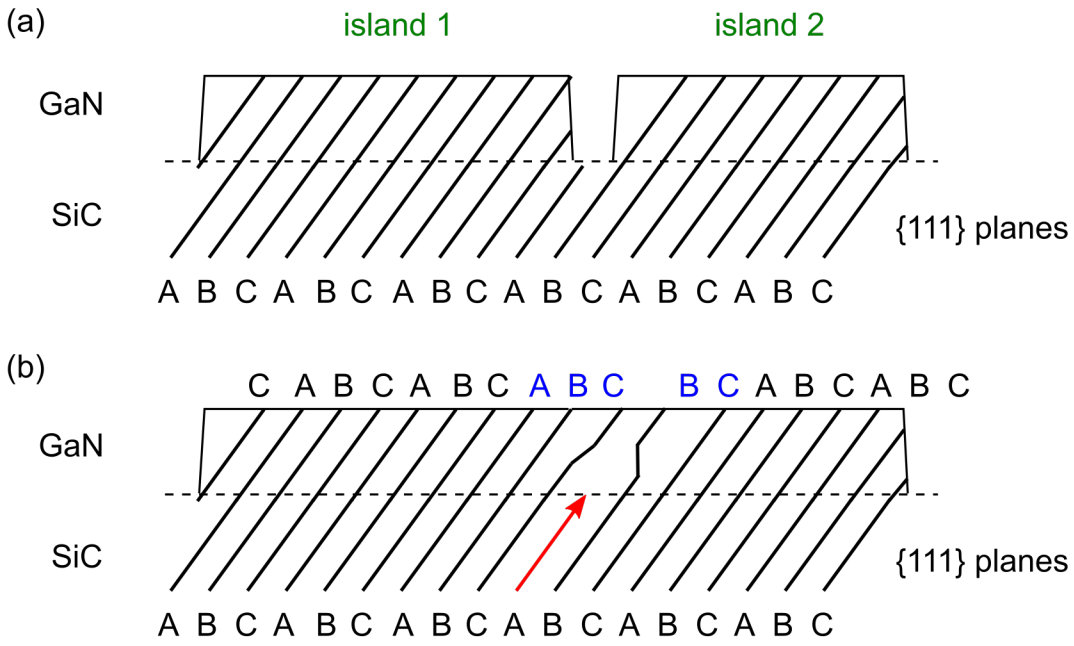

Figure 4.5 Schematic illustrating the island coalescence model to generate a misfit dislocation at the GaN/SiC interface and stacking fault in the GaN layer, with (a) prior and (b) after the coalescence of the two neighbouring islands.

While our data suggests that misfit dislocations can be formed close to island coalescence boundary, the misfit dislocations are also found within islands. Hence we also consider the possibility of diffusion and agglomeration of vacancies to form a misfit dislocation. Narayanan *et al.* [99] proposed that the diffusion of vacancies could facilitate the climb of basal plane dislocations to form a-type threading dislocations in wurtzite GaN. Wurtzite GaN grown by MOVPE at 950 °C – 1100 °C has been shown by Saarinen *et al.* [100] to contain significant concentrations of Ga vacancies, which increased from 10^{16} cm^{-3} to 10^{19} cm^{-3} as the V/III ratio was varied from 1000 to 10000. The low growth temperature of ~ 600 °C used for our NLs could also have the same effect of reducing the surface kinetics as increased amounts of N adatoms, which have a higher sticking

coefficient than Ga adatoms [32]. Hence it is reasonable to expect vacancies to be incorporated into the as-grown NLs. Such vacancies could diffuse to and agglomerate at a particular {111} lattice plane, as illustrated in Figure 4.6, especially during the anneal step. In this model, the misfit dislocation can be generated within an island, and a pair of dislocations (in red) may be generated with a faulted region between them (blue dotted rectangle).

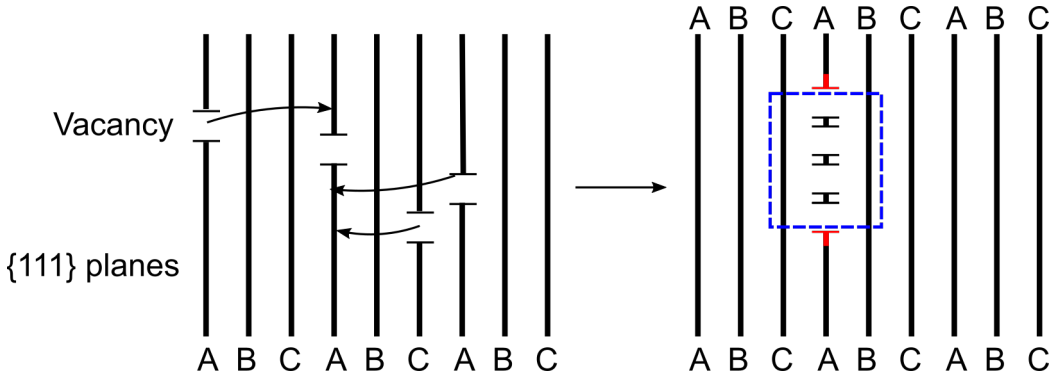

Figure 4.6 Vacancy agglomeration model to generate a pair of misfit dislocation (in red) and a stacking fault (blue dotted rectangle).

The third possible mechanism if the generation of misfit dislocation involves the glide of dislocations from the sample free surface, including the top and sides of an island. It could give rise to dislocations within islands and the dislocations do not have to occur in pairs, as shown in Figure 4.7.

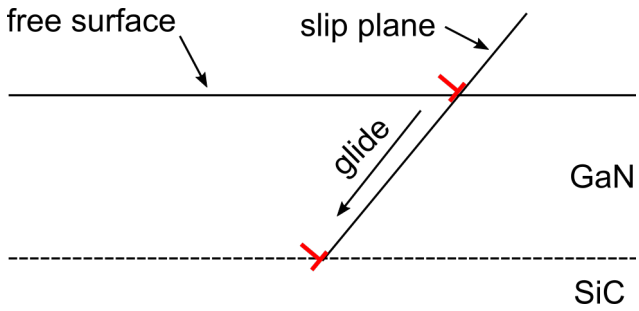

Figure 4.7 Glide of dislocation from the free surface of the sample. Figure adapted from Holec *et al.* [101]

The misfit dislocations are often found close to stacking faults in the perpendicular zone (blue circles). We are not clear on the reason for this, but it could simply be due to the high density of stacking faults at the GaN/SiC interface that makes it likely for a misfit dislocation to exist near a stacking fault.

The STEM images of the as-grown 22 nm thick zb-GaN NL in Figure 4.8 each

show a misfit dislocation, where the extra {111}-type half-plane is indicated by the red arrows. It was possible to draw a right-hand, finish-start Burgers circuit (yellow lines) in Figure 4.8 (a) to determine the Burgers vector (green arrow) of the misfit dislocation to be ½ [-1-10], which is a perfect dislocation in the fcc-based crystal structures like zincblende. However, it is much more common to find that the misfit dislocation is too close to a stacking fault in the perpendicular zone, as indicated by the blue circle in Figure 4.8 (b). In such cases, a Burgers circuit could not be drawn to determine the Burgers vector of the misfit dislocation, as the circuit would have to traverse the imperfect lattice.

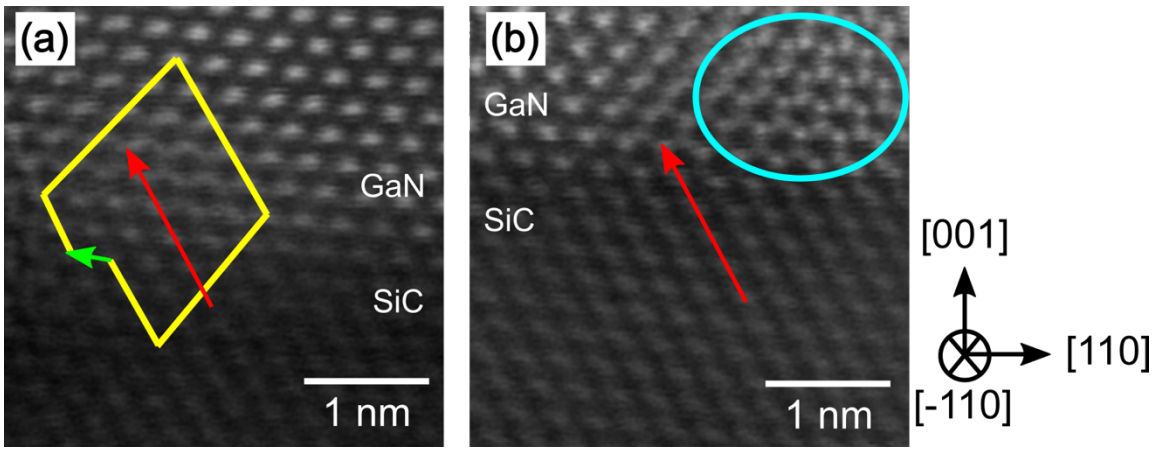

Figure 4.8 STEM images of the as-grown 22 nm thick zb-GaN NL, each showing a misfit dislocation where the extra {111}-type half-plane is indicated by the red arrows. (a) A Burgers circuit (yellow lines) is drawn to determine the Burgers vector (green arrow) of a misfit dislocation. (b) A misfit dislocation close to a stacking fault in the perpendicular [110] zone (blue circle), such that a Burgers circuit cannot be drawn to determine the Burgers vector of the misfit dislocation.

The distances between the misfit dislocations were measured for all three samples. Table 4.2 summarises the total length of sample parallel to the GaN/SiC interface analysed, together with the average and range of measured distances between misfit dislocations, expressed as the number of {111} planes. The average number of {111} planes between misfit dislocations for the 3 nm thick sample is just over half that for both the as-grown and annealed 22 nm thick samples. However, there are limited statistics on the 22 nm thick samples, since the lengths of their sampling areas are less than half that of the 3 nm thick sample, hence there is a larger sampling error for the measurements of the 22 nm thick samples compared with the 3 nm thick sample.

Thickness (nm)		Total length of sample parallel to GaN/SiC interface analysed (nm)	Average no. of {111} planes between extra half-planes	Range of no. of {111} planes between extra half-planes
3	as-grown	181.3	19	4 – 46
22	as-grown	61.7	33	25 – 48
22	annealed	51.2	29	18 – 46

Table 4.2 Summary of the analysis of distance between misfit dislocations in 3 nm thick as-grown, 22 nm thick as-grown and annealed NLs.

Trampert *et al.* [79] found that the misfit dislocations in zincblende GaN grown on GaAs were regularly spaced at every 5 {111} planes, which perfectly relieves the strain from the lattice mismatch of -20.3% between zb-GaN and GaAs at room temperature. As for our case, we would expect an extra {111} half-plane in the 3C-SiC lattice at every 30 {111} planes to accommodate the lattice mismatch strain of + 3.4 % with zb-GaN at room temperature. For the 3 nm thick sample, we found that the average distance between misfit dislocations is 19 {111} planes, resulting in a higher misfit dislocation density than expected theoretically. If we consider the XRD strain measurements of the NLs from Chapter 3, the 3 nm thick NL has the largest compressive strain which decreases in magnitude with increasing layer thickness. Hence we would expect a lower misfit dislocation density for the 3 nm thick NL compared with the 22 nm thick NL. However, the average distance for the 22 nm thick samples are 33 and 29 {111} planes which are much closer to the expected values, even though the sampling error is much larger than for the 3 nm thick sample. This suggests that either the formation of misfit dislocations is not only driven by the reduction of lattice mismatch strain of the islands, or that the areas sampled are not statistically representative of the sample.

Moreover, our experiments do not reveal a periodic array of misfit dislocations that was observed by Trampert *et al.* [79]; for example, the range in distances between misfit dislocations is 4 – 46 {111} planes for the 3 nm thick NL sample. For the growth of heteroepitaxial films, there is the concept that as the thickness of the thin film deposited on the substrate increases, the strain of the film increases until a critical thickness, at which the film becomes unstable and misfit dislocation are generated. [102] Since GaN/GaAs has a large lattice mismatch of – 20.3 %, it is possible that the critical thickness of the GaN layer is so small that GaN cannot be deposited on the GaAs substrate without misfit dislocations, and that the regular array of dislocations forms at the very start of the deposition. On the other hand, GaN/SiC has a much smaller lattice mismatch

of + 3.4 %, so it is probable that GaN can grow coherently at first, up to a critical thickness that may be more than a monolayer. Dislocations are then generated by a variety of mechanisms, such as the three suggested above, at random locations, as opposed to the regular array for GaN/GaAs. Also, it is less likely that the strain energy can be stored over the much larger distance of 30 {111} lattice planes for zb-GaN grown on 3C-SiC compared with 5 {111} lattice planes for zb-GaN grown on GaAs. Hence other forms of strain relief, such as partial dislocations that bound stacking faults, could exist, particularly for misfit dislocations.

4.3.3 Stacking faults

The majority of the {111}-type stacking faults identified in the three samples were of the intrinsic type where the stacking sequence of the planes is ABCBCABC, with a missing 'A' plane of atoms, two examples are shown in Figure 4.1 (f). The prevalence of intrinsic stacking faults in zb-GaN grown on 3C-SiC is likely related to the positive lattice mismatch between zb-GaN and the 3C-SiC substrate, as discussed in the Section 4.3.2. On the other hand, the dominance of extrinsic stacking faults observed by Trampert *et al.* [79] arises from a negative lattice mismatch between zb-GaN and a GaAs substrate. The formation energy of the two different types stacking faults may also play a role in their abundance in zb-GaN. Stampfl and Van der Walle [78] showed that the density-functional theory simulated formation energy of an extrinsic stacking fault was higher than that of intrinsic stacking faults in wurtzite III nitrides, but such calculations have not been performed for zincblende III nitrides.

From the STEM data, we have identified several sources of stacking faults in the zb-GaN NL. Firstly, a stacking fault in the underlying 3C-SiC layer can propagate into the GaN NL. 3C-SiC and Si have a high lattice mismatch of - 20%, and misfit dislocations and SFs are the dominant crystal defects to relief the strain at the heterointerface. [68] Approximately 5 SiC cells fit with 4 Si cells, and the 'extra cell' would require the formation of misfit dislocations and extrinsic stacking faults. The STEM image of a 3 μm thick 3C-SiC/Si substrate with a GaN epilayer in Figure 4.9 (a) shows that the stacking fault density reduces with increasing layer thickness, most likely due to the annihilation of the intersecting stacking faults. Only the occasional stacking faults, highlighted by the yellow lines, reach the surface of the 3 μm thick 3C-SiC layer. Therefore, from our STEM images of the NLs, we have only observed one extrinsic stacking fault with ABCBABC

stacking propagating from the 3C-SiC layer into the GaN NL, as shown in Figure 4.9 (b), but this is not the main source of stacking faults in our GaN NLs.

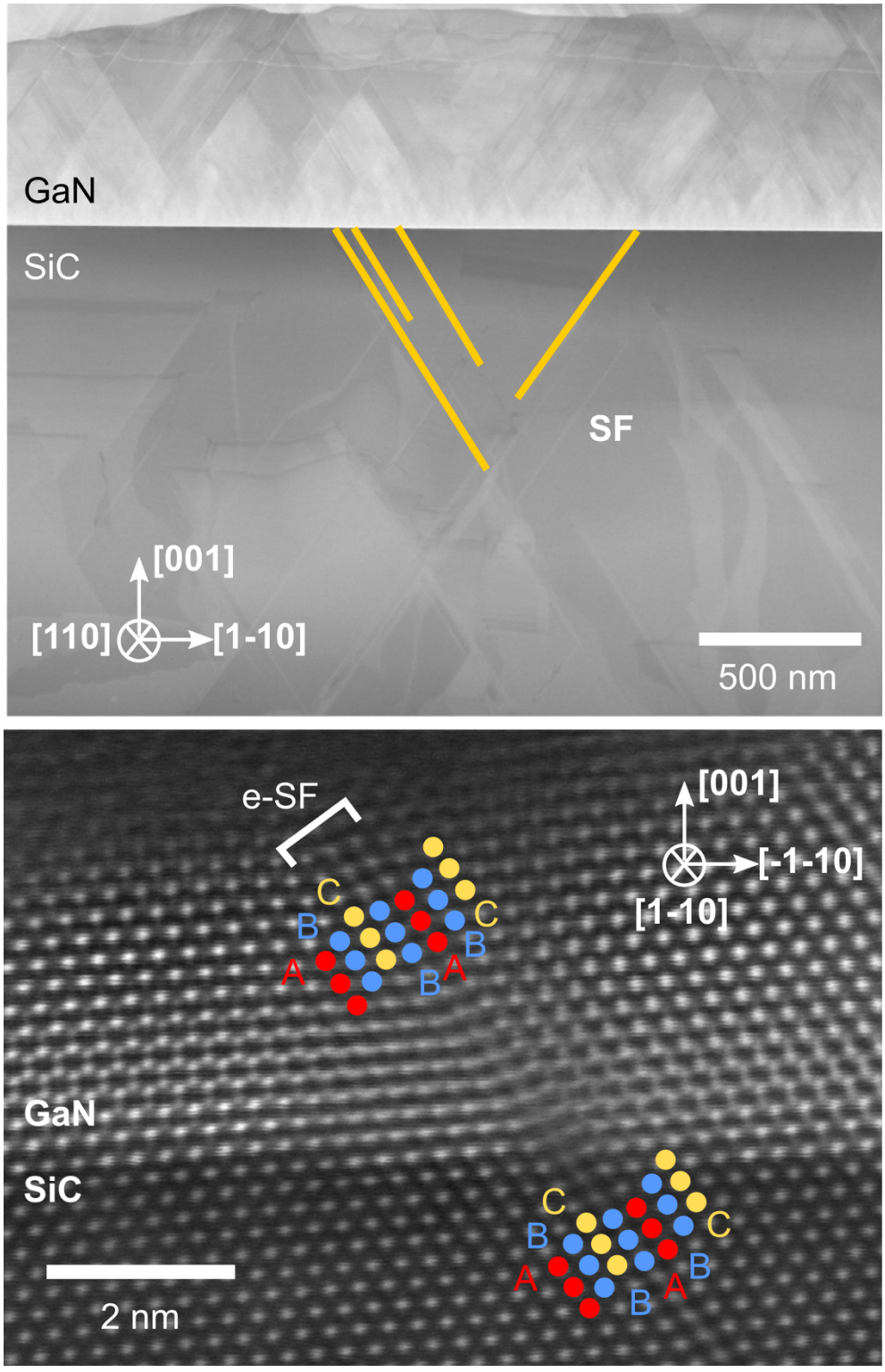

Figure 4.9 (a) STEM image of a 3C-SiC/Si substrate with a GaN epilayer. The yellow lines highlight stacking faults that reach the top of the SiC layer. Data from Boning Ding. (b) STEM image of an extrinsic stacking fault propagating from the SiC layer into the GaN nucleation layer.

In order to accommodate the positive lattice mismatch between zb-GaN and 3C-SiC, an intrinsic stacking fault can be formed from a misfit dislocation due to a missing {111} plane in the GaN NL, as shown in Figure 4.1 (a) and Figure 4.4 (b). However, from Figure 4.10 (a), we observe that this is not the only possible mechanism. Instead, the two intrinsic stacking faults propagating in opposite {111} directions appear to form a V-shape, as highlighted by the white lines, suggesting that they originate from the purple atom at the vertex of the 'V' close to the GaN/SiC interface. Such a configuration is an acute Lomer-Cotterell lock, with a stair-rod partial dislocation close to the GaN/SiC interface and two Shockley partial dislocations that normally bound the other side of the stacking faults pushed to the surface. [103] A Lomer-Coterell lock can be formed when two SFs intersect, and a Shockley partial dislocation from each of the SFs at the intersection react to form a stair-rod partial dislocation. It appears that the purple atom and all the atoms above the arms of the 'V' are slightly displaced towards the [001] direction due to the positive lattice mismatch between GaN and SiC. While this configuration generates two stacking faults, an inverted version of this configuration could represent the case where two intersecting stacking faults are annihilated, as will be discussed in Chapter 6.

At present, we do not have an explanation for the stacking faults that begin further away from the GaN/SiC interface, such as in Figure 4.10 (b), but we speculate that they result from the reactions of partial dislocations associated with stacking faults in the two perpendicular zones, [110] and [-110], which have been observed in cubic SiC films by Kaiser *et al.* [104]

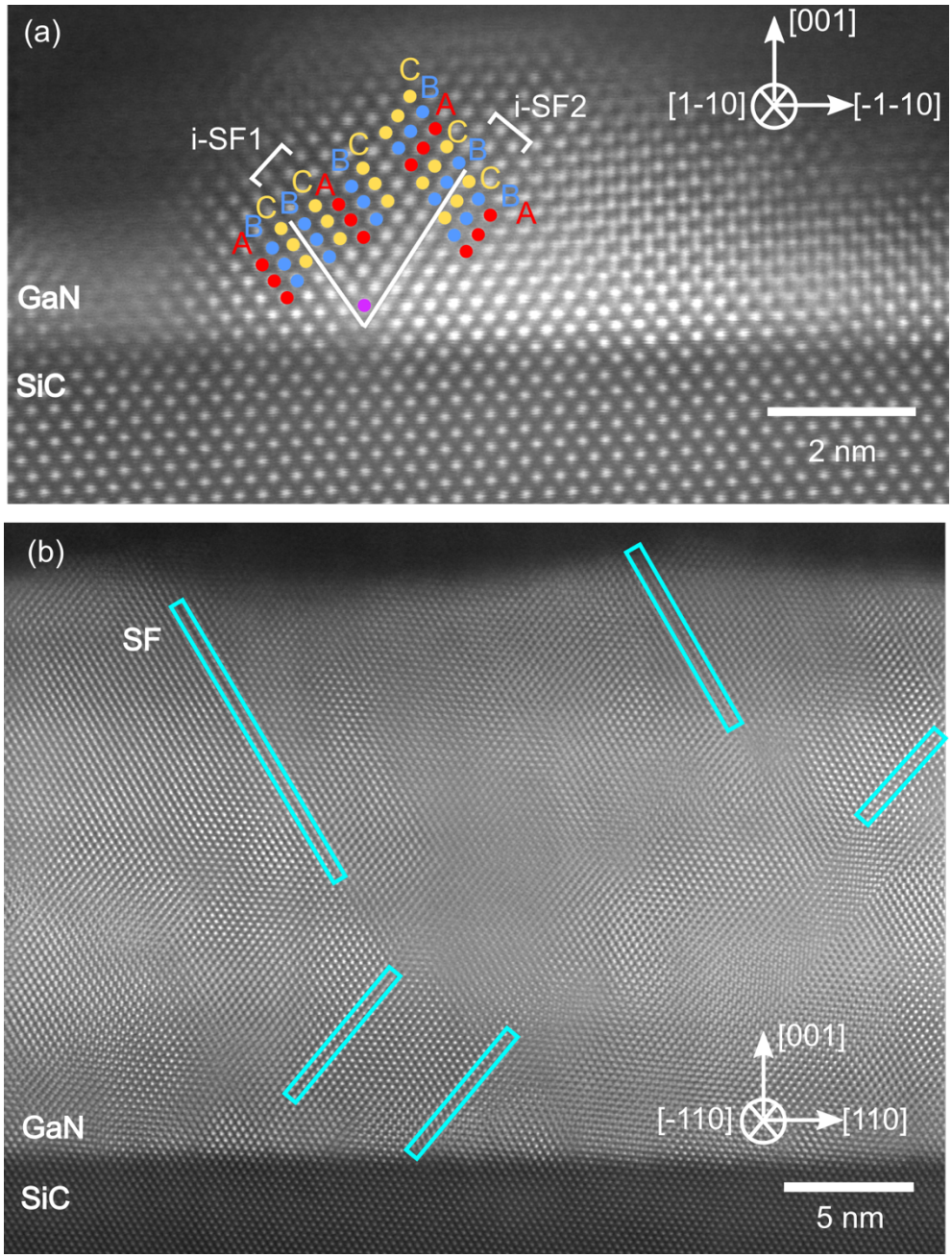

Figure 4.10 (a) STEM image of the as-grown 3 nm thick zb-GaN NL showing two stacking faults that originate from the GaN/SiC interface (b) STEM image of the as-grown 22 nm thick zb-GaN NL showing stacking faults beginning both at and away from the GaN/SiC interface.

A right-hand, finish-start Burgers circuit (yellow lines) was drawn around a stacking fault in the STEM image of the 22 nm thick as-grown zb-GaN NL sample in Figure 4.11. The closure failure is between the two green arrows, and the Burgers vector of the stacking fault has a length that is a fraction of ½ [112].

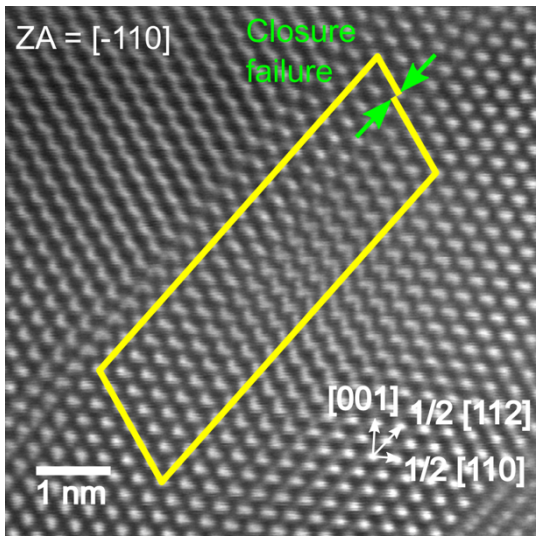

Figure 4.11 A Burgers circuit (yellow lines) drawn around a stacking fault to identify the closure failure (between the green arrows) in a STEM image of the as-grown 22 nm thick zb-GaN NL sample. The zone axis of the image is [-110] and the in-plane directions of the image are marked on the bottom right hand corner.

We found that the Burgers vector of the stacking fault in Figure 4.11 is a fraction of ½ [112]. From Figure 4.8, we identified that the misfit dislocation has a Burgers vector of -1/2 [110], which is a perfect dislocation in a fcc-based structure. Perfect ½ <110> dislocations in fcc structure tend to split into two Shockley 1/6 <112> partial dislocations as this leads to an overall decrease in energy of the system. [105] Therefore it is likely that the Burgers vector identified in Figure 4.11 is 1/6 [112]. This presents another potential way of generating stacking faults. The schematic in Figure 4.12 illustrates an example where a perfect ½ <110> dislocation *b* splits into two 1/6 <112> Shockley partial dislocations, *c* and *d*. The partial dislocations *c* and *d* separate as they repel one another. [105] The atoms in the area bounded by the partials dislocations *c* and *d* are in C positions, as they are not in the B positions of the atoms in the adjacent region, nor the A positions of the atoms in the plane underneath. The extended defect, an intrinsic stacking fault, is thus formed with the stacking sequence ABCACABC. For an extrinsic stacking fault with ABC**BA**BC stacking to form, the separation of a perfect dislocation into partials would have to occur on the successive B and A planes in bold, and this should be energetically less favourable than forming an intrinsic stacking fault. To investigate this further, the

intrinsic and extrinsic stacking faults in the zincblende structure can be modelled in the future and their formation energies can be compared. The fact that stacking faults are found to begin close to the GaN/SiC interface supports the idea that stacking faults form from the splitting of a perfect misfit dislocation into two partials, as misfit dislocations are also found close to the interface.

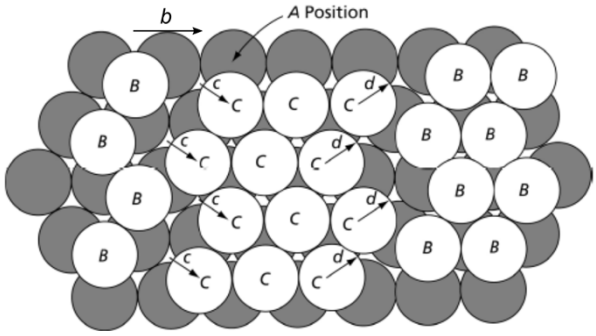

Figure 4.12 Schematic of the plan-view of close-packed {111} planes in a fcc lattice, showing the A, B and C stacking of the zincblende structure. The arrows indicate *b*, a ½ <110> perfect dislocation, and *c* and *d*, which are 1/6 <112> partial dislocations. Figure based on [106].

It was not possible to calculate the stacking fault density at the GaN/SiC interface from the bright-field images of our zb-GaN epilayers (see Chapters 6 and 7), as the stacking fault density is high within the first 100 nm of the GaN layer, making it difficult to clearly identify individual stacking faults (refer to the bright-field images in Chapter 6). Hence an attempt was made to calculate the stacking fault density at the GaN/SiC interface using the STEM images of the NLs. Table 4.3 summarises the total length of sample analysed, the numbers of (-1-11) and (111) stacking faults identified at the GaN/SiC interface and the total stacking fault density in each of the three samples. The average length sampled by STEM for each sample in this study is 186 nm, which is significantly smaller than the average of 10.7 µm sampled by bright-field TEM in Chapter 6. Moreover, we observed from bright-field TEM that the stacking fault density is much higher at the GaN/SiC interface than the rest of the epilayer. However, the calculated stacking fault density at the interface obtained from our STEM analysis is between 3×10^5 cm^{-1} and 7×10^5 cm^{-1}, which is lower than the epilayer stacking fault density of 7×10^5 cm^{-1} at a thickness of 380 nm calculated from bright-field images. Thus we conclude that our STEM analysis to obtain the stacking fault density at the GaN/SiC interface suffers from a large sampling error and the values calculated are not representative of the samples.

Thickness (nm)		Total length of sample analysed (nm)	No. of (-1-11) SFs	No. of (111) SFs	Total SF density at interface ($\times 10^5$ cm^{-1})
3	as-grown	362	4	5	3
22	as-grown	144	7	1	7
22	annealed	51	1	2	7

Table 4.3 Summary of the calculation of stacking fault (SF) density in 3 nm thick as-grown, 22 nm thick as-grown and annealed NLs.

Since both misfit dislocations (perfect dislocation) and stacking faults (partial dislocation) have been observed in the nucleation layers, we consider the extent to which each type of dislocation can provide strain relief. We would expect the strain relief provided by a dislocation in a particular direction should be proportional to the magnitude of the component of its Burgers vector in that direction. Using the perfect dislocation (½ [1-10]) and two partial dislocations (1/6 [1-21] and 1/6 [2-1-1]) as examples, the components of the perfect and partial dislocations along ½ [110], ½ [1-10] and [001] are calculated in Table 4.4. Since the partial dislocations have components along the [001] direction, their components along the [110] and [1-10] in-plane directions are smaller than the perfect dislocation. Hence partial dislocations are expected to provide less strain relief compared with a perfect dislocation.

	Component along		
Burgers vector	½ [110]	½ [1-10]	[001]
½ [1-10]	-	1	-
1/6 [1-21]	-1/6	½	1/6
1/6 [2-1-1]	1/6	½	-1/6

Table 4.4 The components of perfect and partial dislocations along ½ [110], ½ [1-10] and [001].

4.4 Conclusion

In summary, we have observed that zb-GaN NLs are crystalline, with no amorphous layer at the GaN/SiC interface. From STEM images, we can identify misfit dislocations and intrinsic stacking faults as the main defects in the zb-GaN NLs. Misfit dislocations were found close to the GaN/SiC interface, while stacking faults were found to begin close to and away from the GaN/SiC interface. No clear surface steps have been observed in the images, hence there is no evidence of their involvement with the generation of defects.

Misfit dislocations with Burgers vector ½ <110> that are not regularly spaced were found to occur within islands and close to island coalescence boundaries. In theory, misfit dislocations occurring at every 30 {111} planes along the <110> type directions can accommodate the lattice mismatch strain between zb-GaN and 3C-SiC. The absence of periodicity of the misfit dislocations is possibly due to the formation of defects at random locations in the film after a certain critical thickness of the NL. Three possible mechanisms for the formation of a misfit dislocation were suggested: (1) the gap closure during the coalescence of islands to form a misfit dislocation at the coalescence boundary of islands, (2) the diffusion and agglomeration of vacancies in the GaN NL to form a misfit dislocation within an island, and (3) the glide of dislocations from the free surfaces of the sample.

Stacking faults identified in the zb-GaN NL were mainly of the intrinsic type with Burgers vector 1/6 <112> were observed. Several sources of stacking faults that are close to the GaN/SiC interface were identified, including: propagation of extrinsic stacking fault from the underlying 3C-SiC layer; nucleation of an intrinsic stacking fault from a misfit dislocation; and a Lomer-Coterell lock. It is speculated that a stacking fault originating away from GaN/SiC interface is the product of the reaction between partial dislocations associated with stacking faults in perpendicular [110] and [-110] zones. Moreover it is possible for stacking faults to formed when a ½ <110> type perfect dislocation dissociates into two 1/6 <112> type partial dislocations, which then repel each other and separate out.

As for a strategy to reduce the defect density in the NL, defects were found to originate from within islands, hence we cannot simply reduce island size to reduce defect density. However, since misfit dislocations and stacking faults appear to arise from the lattice mismatch between zb-GaN and SiC, we could in the future attempt to reduce their

formation at the GaN/SiC interface by introducing another zincblende material with an intermediate lattice parameter, such as AlGaN, in between GaN and SiC to gradually reduce the lattice parameter. This suggestion is based on the success of AlN interlayers for the reduction of threading dislocation density in wurtzite GaN grown on sapphire [107], graded AlGaN layers for reduction in basal-plane stacking faults density in m-plane GaN grown in SiC [108], and lattice and thermal mismatch strain management of wz-GaN grown on Si (111) with AlGaN buffer layers [109].

5 Surface morphology and phase purity of zb-GaN epilayers

5.1 Introduction

Having investigated zb-GaN nucleation layers grown on 3C-SiC/Si substrates, we now focus our study on the subsequent zb-GaN epilayers. In this chapter, we report on the effect of substrate miscut, growth temperature, V/III-ratio and reactor pressure on the surface morphology and phase purity of zb-GaN epilayers grown on 3C-SiC/Si substrates. We analyse the size of surface features using AFM, and propose a model for the distinct growth regimes observed. The model considers the anisotropy of in-plane strain, reduced symmetry of the top monolayer of the (001)-oriented zb-GaN lattice, the diffusion of Ga and N adatoms on such a surface, and the relative energies of crystal facets.

5.2 Experimental methods

The GaN epilayers were grown by Dr Menno Kappers by MOVPE in a 6 × 2" Thomas Swan close-coupled showerhead reactor on ~ 2 × 2 cm^2 pieces of a 150 mm diameter (001) 3C-SiC/Si substrate provided by Anvil Semiconductors Ltd. The substrate consists of a 2.9 μm thick layer of 3C-SiC grown on a 1000 μm thick Si wafer with miscut of 0°, 1°, 2° or 4° towards the [110] in-plane direction. GaN nucleation layers that are 22 nm thick were grown on pieces of the 3C-SiC/Si substrate, followed by ~ 300 nm thick GaN epilayers grown under a range of growth temperatures and V/III-ratios.

The effect of substrate miscut was investigated by a series of samples grown on 3C-SiC/Si substrates with nominally 0°, 1°, 2° and 4° miscut in the [110] direction. The

GaN epilayers were grown at a temperature of 875 °C, V/III-ratio of 76, and reactor pressure of 100 Torr. It was not possible to determine *in-situ* whether a V/III-ratio of 76 resulted in a N-rich or Ga-rich growth condition.

Two series of samples were grown to investigate the influence of the MOVPE growth temperature and V/III-ratio in the reactor. For the growth temperature series, six samples were grown at temperatures ranging from 850 °C to 910 °C at a constant V/III-ratio of 76, reactor pressure of 100 Torr and a constant growth rate of about 0.54 nm s^{-1}. For the V/III-ratio series, eight samples were grown at V/III-ratios ranging from 15 to 1200 at a fixed growth temperature of 875 °C and reactor pressure of 100 Torr. The variation in V/III-ratio was achieved by keeping the gas flow of TMG into the reactor constant, while the gas flow of ammonia was adapted for each growth run. For the range of V/III-ratios investigated, the growth rate gradually decreased from 0.58 nm s^{-1} to 0.48 nm s^{-1} with increasing V/III-ratio. These two series of samples were also grown at a reactor pressure of 300 Torr to study the effect of reactor pressure.

The GaN surface morphologies were measured using a Digital Instruments Dimension 3100 AFM in tapping mode. MPP-11100-10 tips from Bruker Nano Inc. with a nominal tip radius of 8 nm were used. The topographic data obtained from the AFM was analysed using the free software package WSxM [88]. The fast scan direction for the samples grown on a 4° miscut substrate is along [110], unless otherwise stated. The image height (H) stated in the caption of each AFM scan is the height range from black to white in the image.

To quantify the typical sizes of the surface features along [110] and [1-10], which correspond to directions parallel and perpendicular to the miscut direction of the off-axis substrate, we used the 2D-FFT method described in Section 2.2.5. The average feature size was obtained from the average of five measurements, and the standard error of the mean from the five measurements was used to define the error bars of our measurements.

The facets present on the surface of the samples grown at V/III-ratios of 300 and 1200 were examined in more detail by cross-sectional bright-field TEM imaging, using a FEI Tecnai F20 operated at 200 kV.

As growth conditions and faceting could both significantly influence the crystal quality, Dr Martin Frentrup measured the phase purity of the samples by XRD, using the method described in Section 2.3.2.1.

5.3 Results and discussion

5.3.1 Effect of substrate miscut

The surface morphology of zb-GaN epilayers grown on substrates with nominally 0°, 1°, 2° and 4° miscut in the [110] direction is shown in the 30 × 30 μm^2 AFM height scans in Figure 5.1 (a) – (d). The GaN epilayer grown on the 0° and 1° miscut substrates (Figure 5.1 (a) and (b)) has distinct domains of elongated surface features, with neighbouring domains having surface features that are aligned along two perpendicular <110> directions. In contrast, the GaN epilayer grown on the 2° and 4° miscut substrate (Figure 5.1 (c) and (d)) shows surface features aligned only along the [1-10] direction. Since the surface morphology observed in the GaN epilayers grown on 0° and 1° miscut substrates is similar to that reported by Kemper *et al.* [64] for GaN grown on 0° miscut 3C-SiC/Si substrate, we likewise ascribe the presence of the two types of domains to the presence of antiphase domains (APDs). The absence of two types of domains for GaN epilayers grown on the 2° and 4° miscut substrates indicate that the APDs have been suppressed. Depending on growth conditions of SiC on Si, a 2° miscut can prevent APD formation (Figure 5.1 (c)), or does not prevent their formation (Figure 3.6).

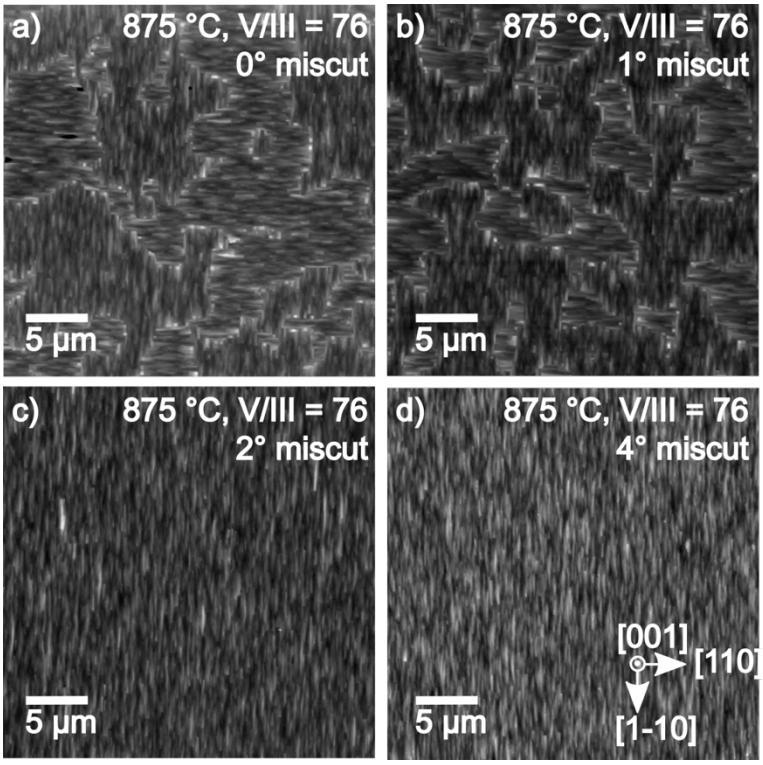

Figure 5.1 30 × 30 μm^2 AFM scans of zb-GaN surfaces grown on substrates with (a) 0°, (b) 1°, (c) 2° and (d) 4° miscut. From (a) – (d), H = 210 nm, 207 nm, 154 nm, 105 nm. All the samples were grown at 875 °C and V/III-ratio of 76.

The average sizes of the surface features and rms surface roughness were extracted from 5 × 5 μm^2 AFM height scans, and represented by the black data points in Figure 5.2 and Figure 5. (a). For the 0° and 1° miscut samples, the 5 × 5 μm^2 scans were selected such that they fit within a single domain and contain surface features that are aligned along the [1-10] direction as shown by the white dashed box in Figure 5.4 (a). Figure 5.2 (a) reveals that the widths of the features on the 0°, 2° and 4° miscut substrates are all similar with a value of 0.6 μm, while the width of the features on the 1° miscut substrate is larger with a value of 0.8 μm. As for the length of the features shown in Figure 5.2 (b), they were smaller on the 0° and 1° miscut substrates (1.4 μm – 2.1 μm) than on the 2° and 4° miscut substrates (2.0 μm to 2.7 μm). This has resulted in the aspect ratio (length/width) of the features to be larger on the 2° and 4° miscut substrates (3.0 – 4.5) than on the 1° and 0° miscut substrates (1.7 – 3.0), as presented in Figure 5.2 (c).

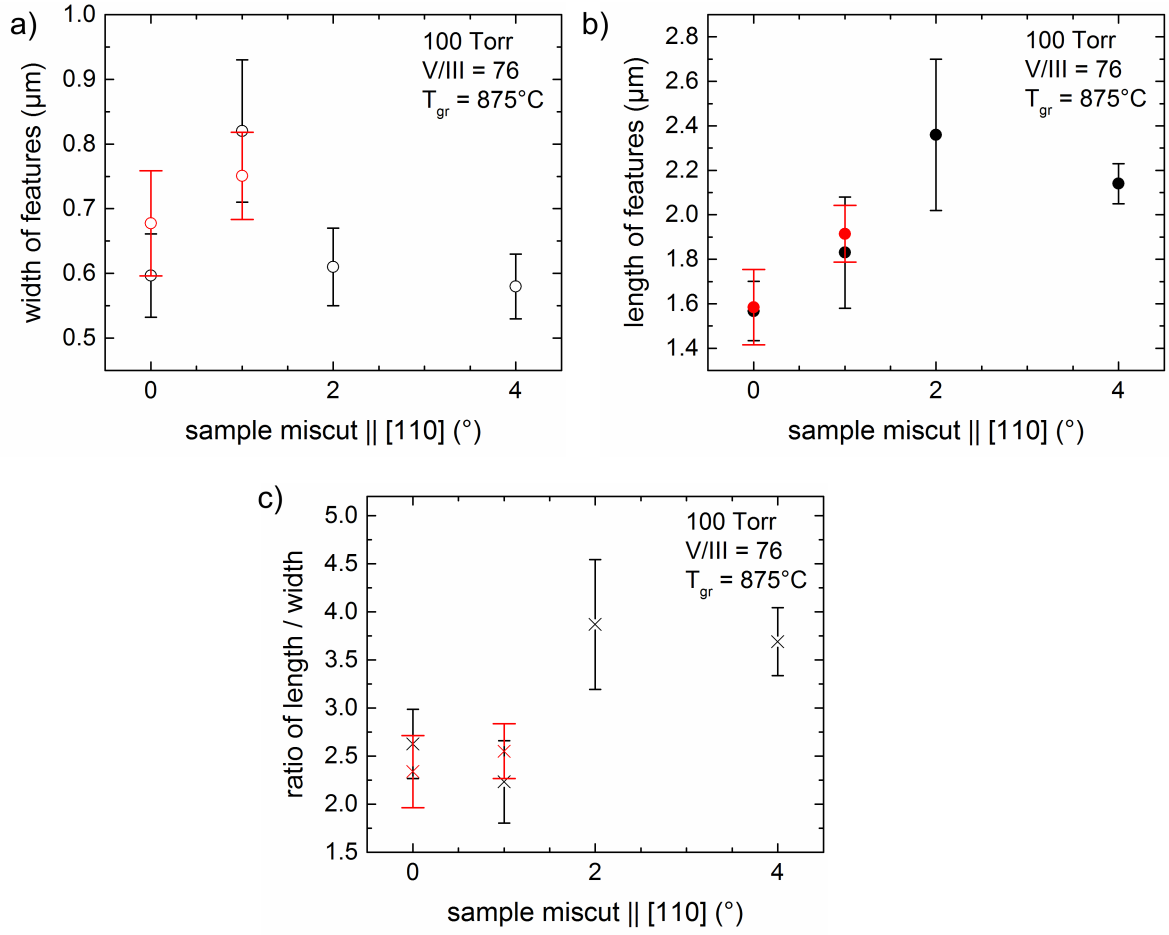

Figure 5.2 The (a) length and (b) width of surface features extracted from 2D-FFT of AFM height data of the zb-GaN epilayers grown on substrates with 0°, 1°, 2° and 4° miscut at 875 °C and V/III-ratio of 76. (c) Variation of aspect ratio of surface features with substrate miscut. The black and red data points are measured from domains where the surface features are aligned along the [1-10] and [110] directions, respectively. All measurements are made from 5 × 5 μm^2 AFM scans.

The root mean square (rms) surface roughness of 5 × 5 μm^2 AFM scans in Figure 5. (a) is lowest for 4° miscut with a value of (11.1 ± 0.3) nm, while that for 0°, 1° and 2° miscut is larger, ranging between 12.5 – 14.5 nm. Since the 30 × 30 μm^2 AFM scans image both the domains and their boundaries, the rms surface roughness obtained from such scans is significantly higher than from the 5 × 5 μm^2 AFM scans for the 0° and 1° miscut samples, as presented in Figure 5. (b). On the other hand, the rms surface roughness from the two sizes of AFM scans is similar for the 2° and 4° miscut samples, since such sample surfaces do not have domain boundaries.

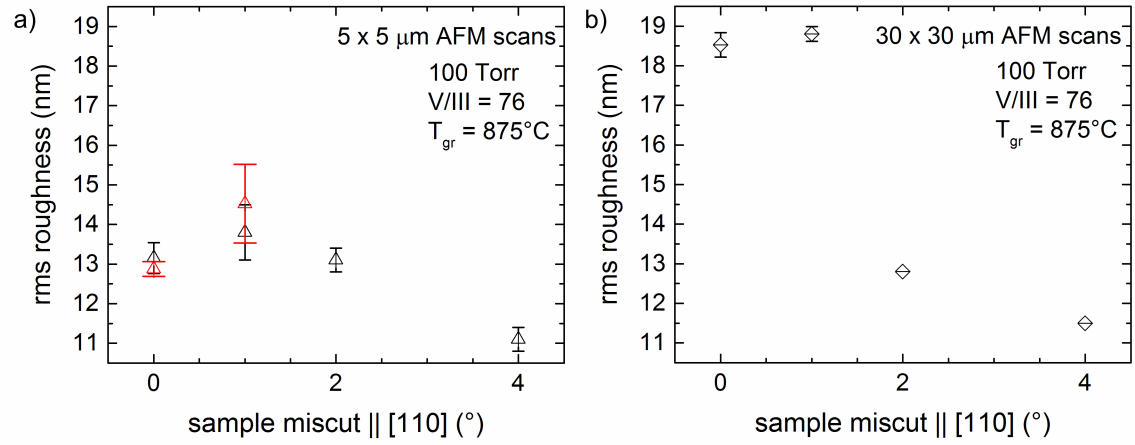

Figure 5.3 Variation of root mean square surface roughness with substrate miscut from (a) 5 × 5 μm^2 AFM scans and (b) 30 × 30 μm^2 AFM scans. The black and red data points in (a) are measured from domains where the surface features are aligned along the [1-10] and [110] directions, respectively.

If the domains observed in the 0° and 1° miscut samples are indeed APDs, the feature size, aspect ratio and surface roughness should be similar in the two types of domains with perpendicularly aligned features. To investigate this, AFM scans were also obtained from 5 × 5 μm^2 areas from domains where the surface features are aligned along the [110] direction in Figure 5.1 (a) and (b). This is achieved by rotating the samples by – 90° between scans of the two types of domains, such that the AFM fast scan direction is always perpendicular to the elongation direction of the features, as shown in Figure 5.4. An example of such a 5 × 5 μm^2 scan is highlighted by the red dashed box in Figure 5.4 (b). The information obtained from the domains where the elongated surface features are aligned along the [110] direction are represented by the red data points in Figure 5.2 and Figure 5. (a). There appears to be no significant difference between the properties of the two types of domains when we compare the black and red data points in these figures, supporting that they are APDs.

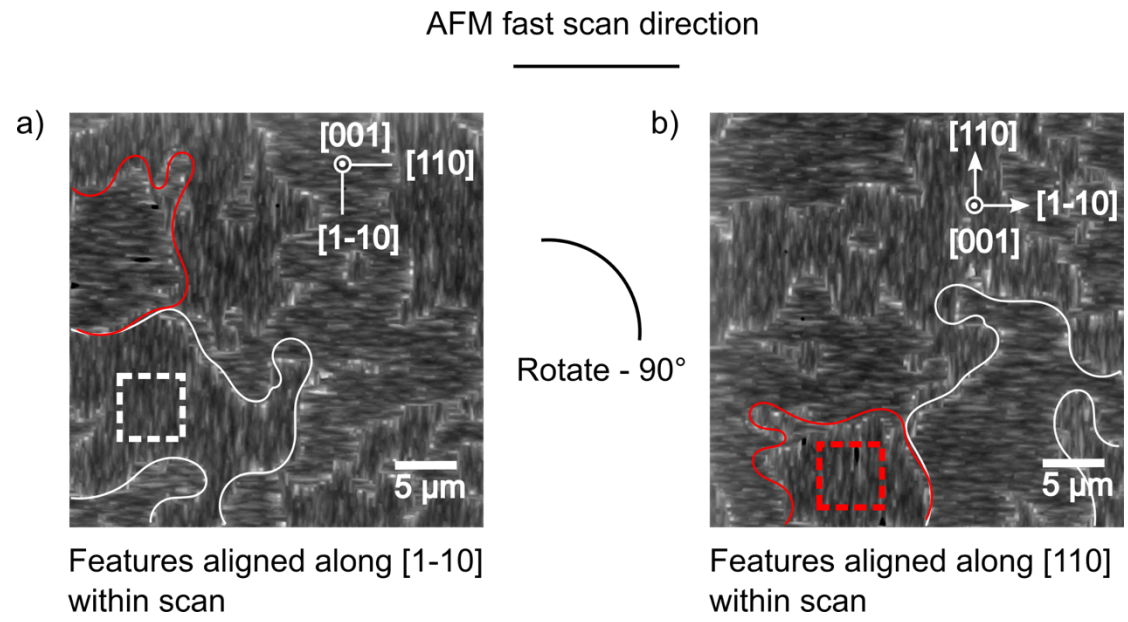

Figure 5.4 Method of obtaining AFM scans of the two types of domains in 0° and 1° miscut samples.

The AFM scan of the bare 3C-SiC/Si substrate with 0° miscut in Figure 5. (a) reveals meandering boundaries, highlighted in red in Figure 5. (b), which we believe are further evidence of antiphase domain boundaries in the 3C-SiC layer, although the as-grown surface morphology of the 3C-SiC is lost due to a chemical mechanical polish process prior to zb-GaN growth. Since the 3C-SiC layer templates the growth of the GaN epilayer, the APDs in the SiC layer are likely to extend into the GaN film.

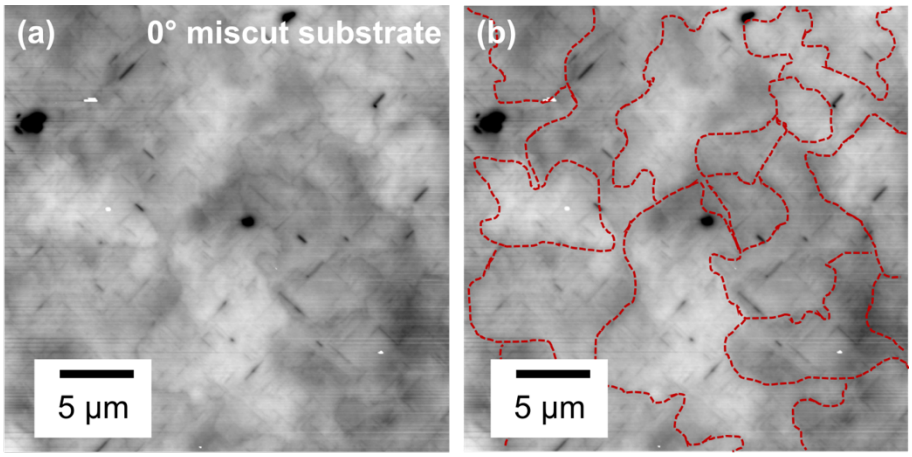

Figure 5.5 (a) 30 × 30 µm^2 AFM scan of the 3C-SiC-on-Si substrate with 0° miscut, and (b) the same image as (a) with the meandering boundaries highlighted in red. H = 7 nm.

The 40 × 40 µm^2 AFM scans of zb-GaN surface grown on substrates with 0° and 1° miscut are shown in Figure 5., with the domain boundaries highlighted in red. The average area of the domains is (50 ± 4) µm^2 for bare substrate with 0° miscut, and (131 ±

11) μm^2 for GaN grown on the same substrate, as calculated by dividing the total area of a scan by the number of domains in each scan. While we would expect the APDs in the SiC substrate to be templated onto the GaN epilayer and the area of domains on the two surfaces to be similar, it is possible that the area of APDs varies with position of the wafer resulting in the large difference measured.

As shown in Figure 5. (a) and (b), the areas of the two types of domains for the 0° miscut sample are similar, while the domain with surface features elongated along the [1-10] direction is the dominant one for the 1° miscut sample. This shows that a small angle miscut of 1° is already effective in reduce the formation of APDs.

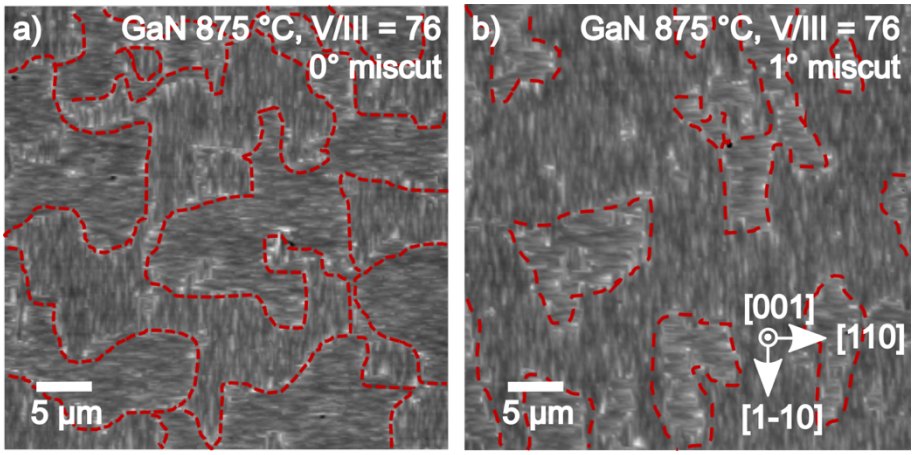

Figure 5.6 40 × 40 μm^2 AFM scan of zb-GaN surfaces grown on substrates with (a) 0° and (b) 1° miscut. Domain boundaries are highlighted in red. For (a) and (b), H = 228 nm and 331 nm.

Finally, we investigated the surface morphology of a GaN epilayer grown on a substrate with 4° miscut towards the [100] direction, instead of the [110] direction which has been used so far. From the AFM scans shown in Figure 5., the surface consists mainly of features elongated in the [110] direction with small areas where the features are elongated in the perpendicular [-110] direction.

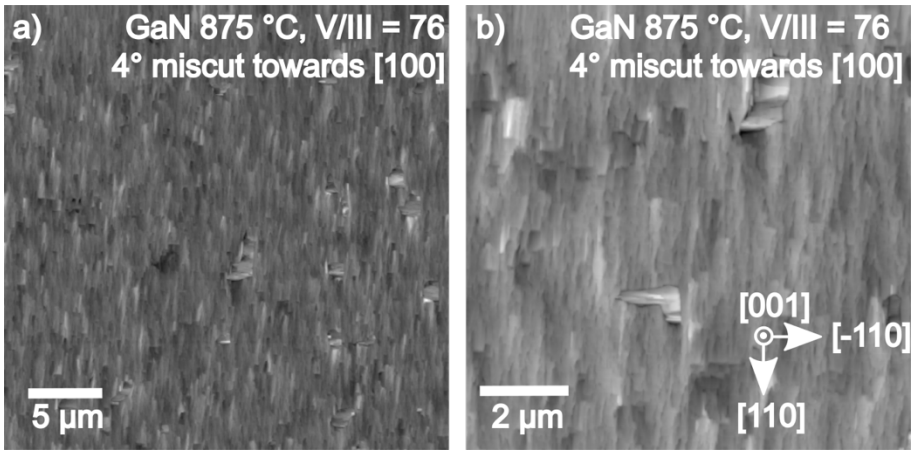

Figure 5.7 (a) 30 × 30 µm and (b) 5 × 5 µm^2 AFM scans of zb-GaN surfaces grown on substrates with 4° miscut towards [010]. For (a) and (b), H = 160 nm, 129 nm.

APDs are non-uniformities in the GaN film and are expected to be detrimental to device fabrication and thus should be avoided. This eliminates the use of 0° and 1° miscut substrates, and substrates with miscut along the [100] direction. Moreover, surfaces with the lowest rms roughness are expected produce better quantum well growth subsequently, and the 4° miscut substrates has a lower rms surface roughness compared with the 2° miscut substrate. In view of the results above, substrates with a 4° miscut along the [110] direction, free of APDs, were used for the rest of the study.

5.3.2 Effect of growth temperature

The change in surface morphology of the GaN epilayer with growth temperature is shown in the AFM scans in Figure 5. As the temperature was increased from 850 °C to 910 °C, the geometry of the surface features changes from elongated along [1-10] to become more square-like. This observation is reflected in the average feature sizes extracted from the AFM height data using the method described in Section 3.2. Figure 5. (a) reveals that the feature size in [110] direction ($f_{[110]}$) increases by a factor of two from (0.64 ± 0.04) µm to (1.31 ± 0.09) µm as the growth temperature increases from 850 °C to 910 °C. In contrast, the feature size in [1-10], ($f_{[1\text{-}10]}$) in Figure 5. (b), is approximately halved from (3.75 ± 0.38) µm to (2.08 ± 0.11) µm in the same increasing temperature range. Consequently, the aspect ratio ($f_{[1\text{-}10]}/ f_{[110]}$) decreases from 5.8 ± 0.7 (elongated) to 1.6 ± 0.1 (square-like) with increasing temperature as shown in Figure 5. (c). The root mean square (rms) surface roughness of 10 x 10 μm^2 AFM scans in Figure 5. (d) ranges from (10.4 ± 0.1) nm to (12.9 ± 0.3) nm, which is not a significant variation. The lowest rms roughness is observed at a growth temperature of 885 °C, which is in the middle of the temperature range investigated. Such rms roughness values are in the same order of magnitude as reported for semi-polar (11-22) GaN growth on sapphire, where similar surface undulations were observed [110]. The zb-GaN content determined by XRD is shown in Figure 5.10, which indicates that the zincblende content of all samples was above 98 %, with only a small deterioration in phase purity for growth temperatures above 885 °C.

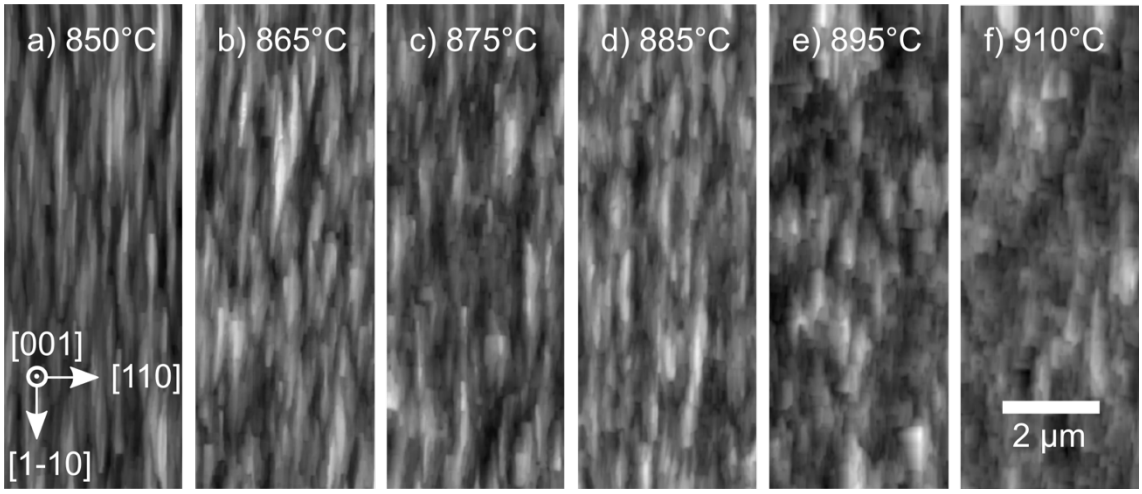

Figure 5.8 AFM scans of the surfaces of zb-GaN epilayers grown at varied growth temperatures and a constant V/III-ratio of 76. The growth temperature used is indicated at the top of each image. From (a) – (f), H = 117 nm, 85 nm, 90 nm, 72 nm, 79 nm and 103 nm.

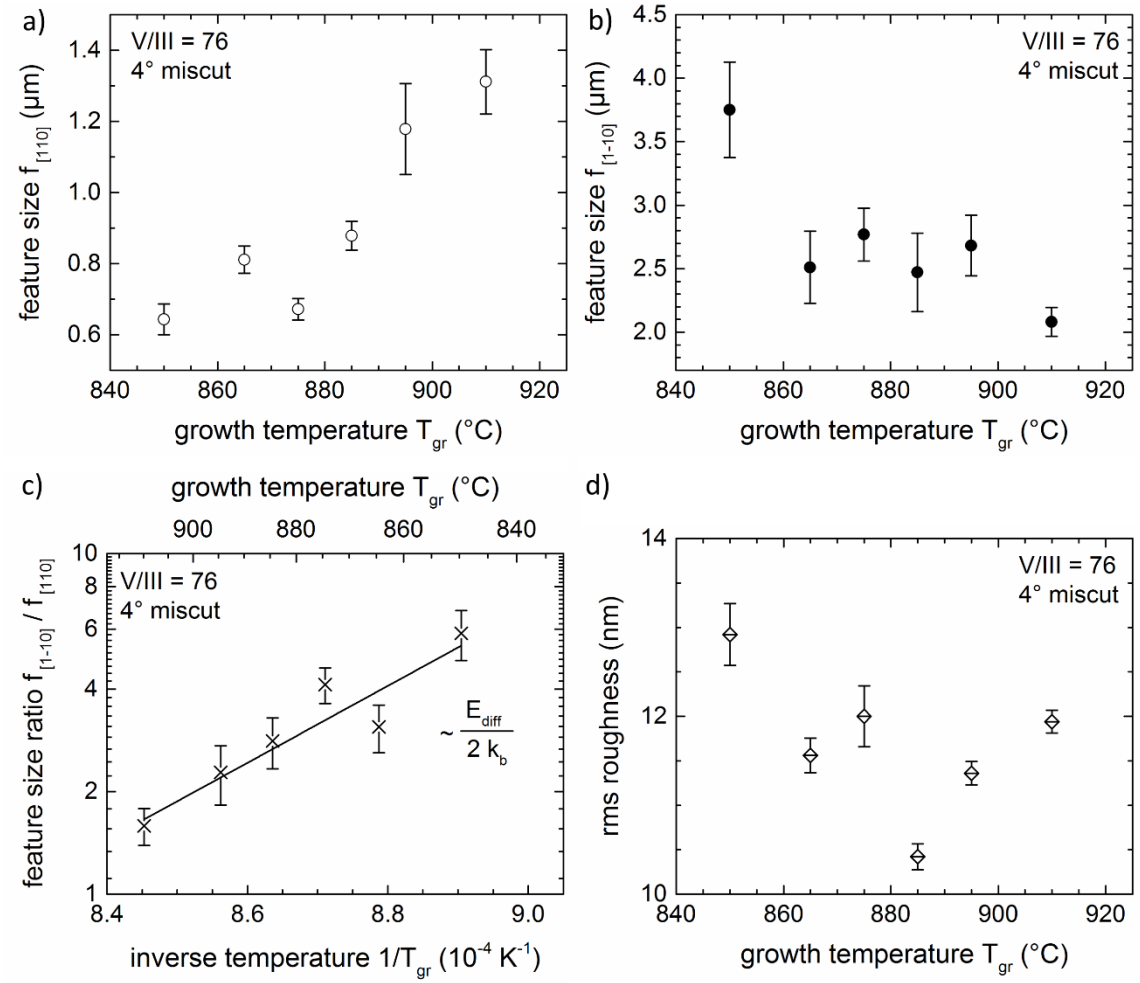

Figure 5.9 Feature sizes in (a) [110] and (b) [1-10] directions extracted from 2D-FFT of AFM height data of zb-GaN epilayers grown at different growth temperatures and a constant V/III-ratio of 76. (c) Variation of the aspect ratio of surface features with growth temperature. The function $y = A \exp\left(\frac{E_{diff}}{2k_b} \times \frac{1}{T}\right)$, where E_{diff} is the difference between the potential barriers for diffusion within the valley and across -Ga-N- chains, was fitted as shown by the line of best fit. (d) Variation of root mean square surface roughness with growth temperature.

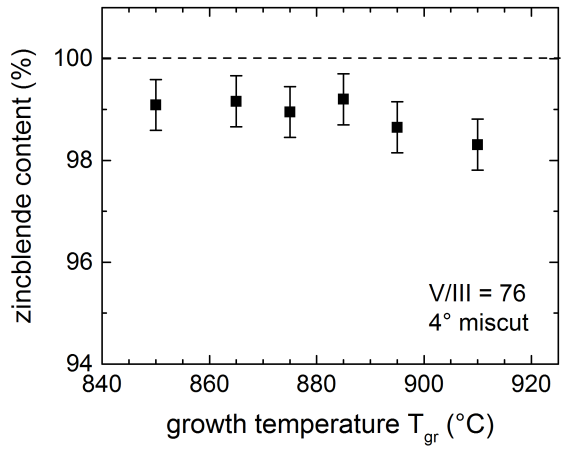

Figure 5.10 Zb-GaN content determined by XRD as a function of the GaN epilayer growth temperature. Data from Dr Martin Frentrup.

A similar surface morphology with elongated surface features is observed in both the zb-GaN film grown on a 4° miscut substrate and within an APD of the zb-GaN film grown on a 0° miscut substrate (Figure 5.1). This demonstrates that the surface morphology seen in the samples grown on a 4° substrate is not simply related to step-bunching driven by the substrate miscut, but must be determined by surface energy considerations. The 90° rotation of the surface morphology in neighbouring APDs of a zb-GaN film grown on a 0° miscut substrate further suggests that the surface morphology is controlled by the symmetry of the crystal surface.

It is worth noting that zb-GaN grown on 3C-SiC/Si by MBE under Ga-rich conditions do not display such elongated surface features. This could indicate that our MOVPE growth condition of V/III-ratio of 76 results in N-rich growth.

A common source of the periodic surface undulations observed is the self-organisation of the surface to minimise the thin film's total energy, given by its in-plane strain energy and surface energy. The surface atoms of the thin film redistribute to form periodic peaks and troughs, such that the in-plane strain is minimised at the cost of an increasing surface energy [111].

The striated GaN surface features observed indicate that the underlying diffusion process is anisotropic along the two in-plane directions, [110] and [-110]. For this behaviour, we have identified two possible causes for anisotropic diffusion on the surface: anisotropic in-plane strain as the driving force for the atom flux, and the reduced symmetry of the top monolayer of a (001)-oriented zb-GaN lattice.

For a (001) zb-GaN layer growing on a perfect (001) SiC/Si substrate, the lattice mismatch strain should be isotropic. However, in an earlier publication [58] we have shown that for a zb-GaN film grown on a 3C-SiC/Si substrate with 4° miscut towards [110], the in-plane strain in the [110] direction ($(3.65 \pm 0.11) \times 10^{-3}$) is slightly larger than that in the [1-10] direction ($(1.92 \pm 0.09) \times 10^{-3}$). We believe this small post-growth anisotropy in strain is related to plastic deformation of the Si substrate which occurs at the high temperatures used for growth of the SiC and results in a 'pringle' shaped bowing of the wafers. Since this anisotropy in strain is small we do not believe that it contributes significantly to the surface morphology seen and this is supported by the fact that a similar morphology is observed within each APD for a zb-GaN film grown on the on-axis substrate, where the in-plane strains are isotropic. Nevertheless, we note that, based on the work of Gao and Nix [111], the anisotropy of in-plane strain we observe would lead to a

larger degree of rearrangement per unit length along [110] than along [1-10], and consequently a shorter $f_{[110]}$ than $f_{[1\text{-}10]}$ as observed in our samples.

The schematic in Figure 5.11 shows the atomic arrangement of the Ga-N bilayers close to the surface of a (001)-oriented zb-GaN lattice, with (a) showing the top view of the (001) plane, and (b) the cross-sectional view along the [1-10] zone axis. The small and large circles represent the positions of Ga and N atoms, the red filled circles mark the atoms in the top-most monolayer, while the open circles show the underlying monolayer. It is clearly seen in the projection of the (001) plane in Figure 5.11 (a) that the surface has a two-fold symmetry, with the alternating Ga and N atoms in the top monolayer arranged in chains, which run along the [1-10] direction and are separated by ½ of the unit cell face diagonal. The atoms in the monolayer directly below are arranged in the same way, but the -Ga-N- chains are shifted by ½ of the unit cell length with respect to the top monolayer. Based on this reduction in symmetry, it is not unreasonable to expect surface adatoms to have different diffusion coefficients in the [110] and [1-10] directions. Within our MOVPE reactor, it is not possible to obtain detailed information about any surface reconstructions at the growth surface such as that given by reflection high energy electron diffraction (RHEED) in MBE growth, but it is speculated that potential valleys, highlighted in yellow in Figure 5.11 (a) and (b), are present between the -Ga-N- chains in the top monolayer. Within such valleys, adatoms can easily diffuse between local surface potential minima, whereas diffusion across the -Ga-N- chains is hindered.

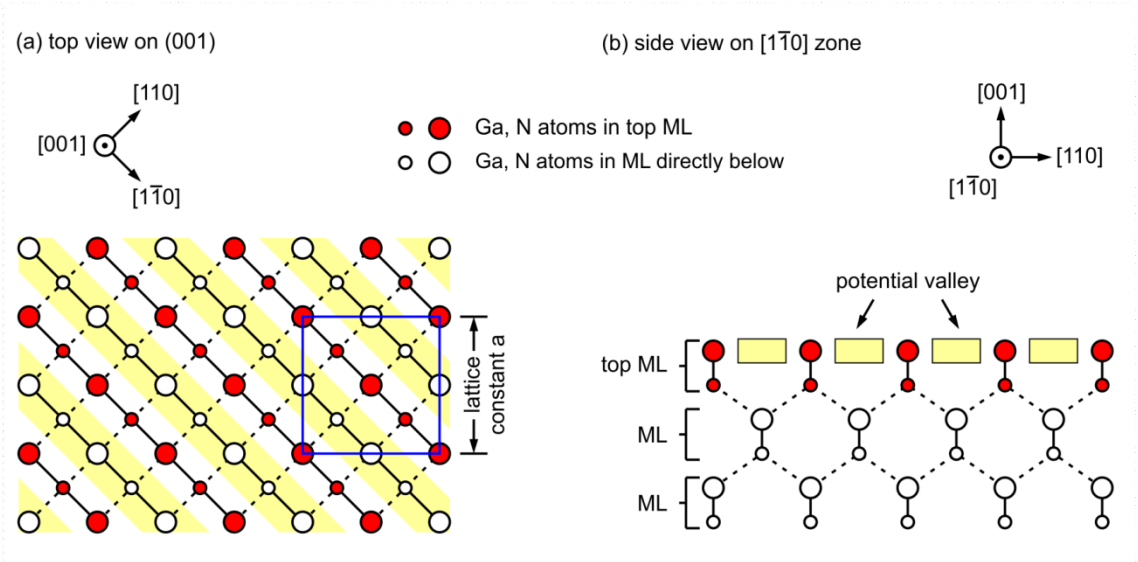

Figure 5.11 Arrangement of atoms of a (001)-oriented zb-GaN lattice. (a) Projection of the (001) plane, (b) cross-sectional view along the [1-10] zone axis. The blue square in (a) indicates the unit cell of zb-GaN. Figures from Dr Martin Frentrup.

In order to explain the evolution of the surface morphology, we propose that at relatively low growth temperatures, adatoms are likely to be trapped in the potential valleys, limiting diffusion along [110] and resulting in features being elongated along the potential valleys in the [-110] direction. With increasing temperature, it becomes more likely that adatoms can diffuse across the -Ga-N- chains, leading to the experimentally observed increase in $f_{[110]}$. We suppose that the activation of adatoms to diffuse across the -Ga-N- chains reduces the number of adatoms trapped in potential valleys for the diffusion within the valleys, thus explaining the reduction in $f_{[110]}$. Overall, the shape of the features becomes increasingly square-like at higher growth temperatures, as the diffusion along the two in-plane directions become more similar.

Based on the measured feature size change with growth temperature, the energy difference (E_{diff}) between the potential barriers for diffusion within the valley and across the -Ga-N- chains can be estimated. In a simplified model, the average diffusion length (λ) of an adatom at temperature (T) is given by the diffusion coefficient (D) and the average lifetime (τ) on the surface before it is incorporated into the lattice or desorbs: [112,113]

$$\lambda(T) \sim \sqrt{D\,\tau} = \sqrt{D_0\,\tau} \times e^{\frac{-\Delta E}{2k_bT}} \qquad \text{(Eq. 5.1)}$$

Here D_0 is the temperature independent diffusion constant and ΔE is the potential barrier energy. Using Eq. 1 and assuming that the feature sizes ($f_{[110]}$ and $f_{[1\text{-}10]}$) are proportional to λ, the ratio of the feature size in the [1-10] and [110] directions in Figure 5. (c) can be described by:

$$\frac{f_{[1-10]}}{f_{[110]}} \sim e^{\frac{-(\Delta E_{[1-10]}-\Delta E_{[110]})}{2k_bT}} = e^{\frac{-E_{diff}}{2k_bT}} \qquad \text{(Eq. 5.2)}$$

yielding the energy difference $|E_{diff}|$ = (4.3 ± 0.5) eV. Such a calculated potential barrier energy should be treated as an order of magnitude estimate, since the mathematics applied is not a complete solution of the diffusion equation, and furthermore, other processes including possible changes in the V/III-ratio with temperature may influence the morphology.

For non-polar a-plane and m-plane wz-GaN, Lymperakis *et al.* [112] calculated barrier energies between 0.21 eV and 0.93 eV, depending on the growth orientation and in-plane direction. Ploch *et al.* [114] measured barrier energies of ~ 0.8 eV and 1.3 eV for

semi-polar (11-22) GaN. Our result on the difference between the activation energies in the two perpendicular directions suggest that the actual activation energies, particularly across the potential valleys in [110] direction, are relatively high in comparison to values in the literature for wz-GaN, and the difference is possibly due to the difference in the arrangement of atoms and dangling bonds between zb-GaN and wz-GaN. Brandt *et al.* [36] measured an activation energy of 2.48 eV for diffusion of Ga on (001) zb-GaN, which accords with our suggestion that the activation energies for diffusion may be relatively high in the zb-GaN system. However, it is unclear whether differences in the activation energy in different directions influenced Brandt *et al.*'s analysis.

5.3.3 Effect of V/III-ratio

Another important parameter that controls the surface morphology of (001) zb-GaN thin films is the V/III-ratio in the gas phase during MOVPE growth. Figure 5.12 shows AFM scans of the surface morphology of a series of samples grown at V/III-ratios ranging from 15 to 1200, at a fixed growth temperature of 875 °C. For the samples grown at the lower V/III-ratios the surface morphologies show a significant difference to that seen at higher V/III-ratios. For a V/III ratio of 15, the surface features are aligned along two axes, at ~ ± 45° from the [110] direction, as marked by the bold white arrows in Figure 5.12 (a). For samples grown at a V/III-ratio of 38 and above (Figure 5.12 (c) – (h)), the surface morphologies consist of features elongated only along the [1-10] direction, similar to that observed in the temperature series. The sample grown at a V/III-ratio of 23 appears to be a transition between the two types of surface morphology.

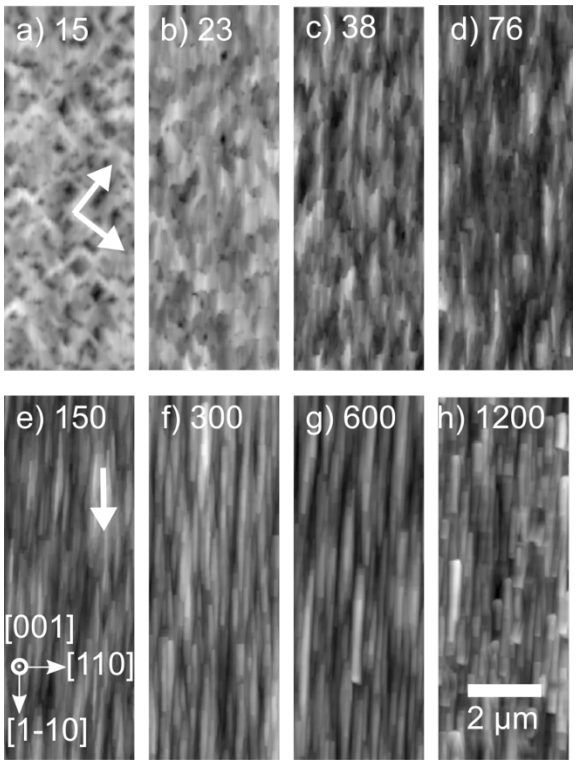

Figure 5.12 AFM scans of the surfaces of zb-GaN epilayers grown at various V/III-ratios and a constant growth temperature of 875 °C. The V/III-ratio used is indicated at the top of each image. From (a) – (h), H = 256 nm, 200 nm, 81 nm, 90 nm, 117 nm, 165 nm, 156 nm, 152 nm. The bold white arrows in (a) and (e) indicate the predominant in-plane orientations of the surface features.

The change in surface morphology with V/III-ratio is also apparent in the quantitative data extracted from the AFM height scans, as presented in Figure 5.13, which reveals three regimes that we label as i, ii and iii. It is not meaningful to extract features

sizes along [110] and [1-10] in the case of the sample grown at a V/III ratio of 15 (in regime i) since for this sample the predominant orientation of the features is along neither of these two directions which dominate the other samples.

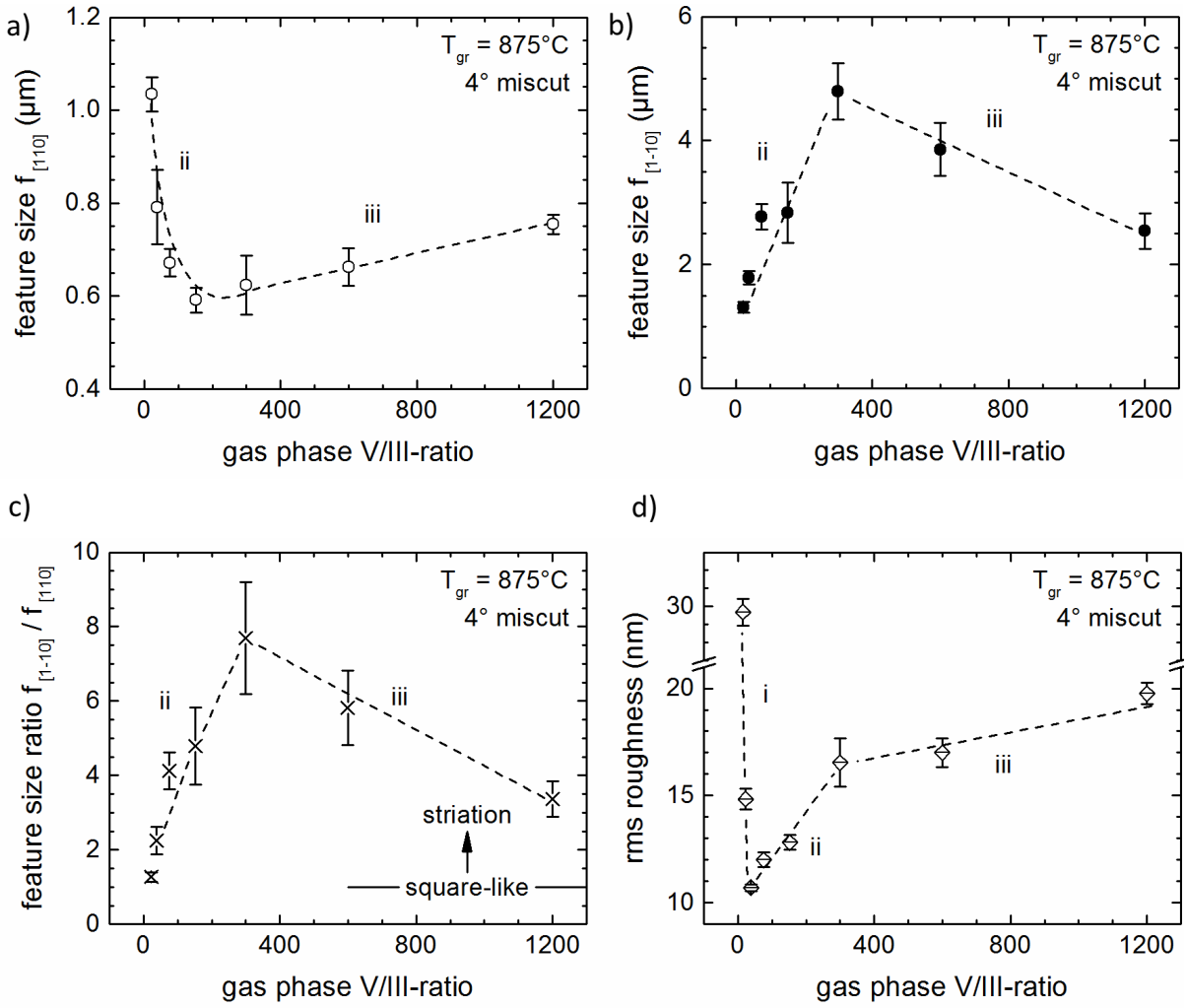

Figure 5.13 Feature sizes in (a) [110] and (b) [1-10] directions extracted from 2D-FFT of AFM height data of the zb-GaN epilayers grown at different V/III-ratios and a constant growth temperature of 875 °C. (c) Variation of aspect ratio of surface features with V/III ratio. For (a) to (c), there are no data points for the sample grown at a V/III-ratio of 15, as it was not possible to extract feature sizes using the same 2D-FFT method as for other sample in the series. (d) Variation of root mean square surface roughness with V/III-ratio. The labels i, ii and iii indicate the proposed growth regimes.

Regime i

The distinction between regimes i and ii is only apparent from the comparison of rms roughnesses in Figure 5.13 (d), and is unclear from feature sizes in Figure 5.13 (a) – (c). The sample grown at a V/III-ratio of 15, with the long axes of surface features at ~ ± 45° to the [110] direction (marked by the bold white arrows in Figure 5.14 (a)), has a particularly high rms surface roughness of (29.7 ± 0.7) nm. As the V/III-ratio increases

and the surface features become increasingly aligned in [1-10] direction along the potential valleys (as discussed in Section 0), the rms roughness decreases to the lowest value in the series of (10.7 ± 0.1) nm at a V/III-ratio of 38. Figure 5.14 (b) is a 2 × 2 μm^2 AFM scan of a surface feature typically observed in the sample grown at a V/III-ratio of 15 in Figure 5.14 (a). Note that the fast scan direction is along [010], perpendicular to the longer facet of the surface feature. The steepest slope of several similar facets is measured to be between 45° – 55° with respect to the bottom surface of the substrate, as determined from line profiles of AFM height scans such as in Figure 5.14 (c). Such facet angles, together with the fact that the facets are aligned along the <100> in-plane directions, suggest that the facets observed in Figure 5.14 (a) are (-101), (101), (011), or (0-11) facets. From Figure 5.14 (b), we also note the existence of surface features with axes along [110] and [1-10], which become predominant at higher V/III-ratios in the growth regimes ii and iii. This suggests that we are approaching the point where the facet energies are approximately equal, and as we further decrease the V/III-ratio the {101}-type facets mentioned above become more prominent.

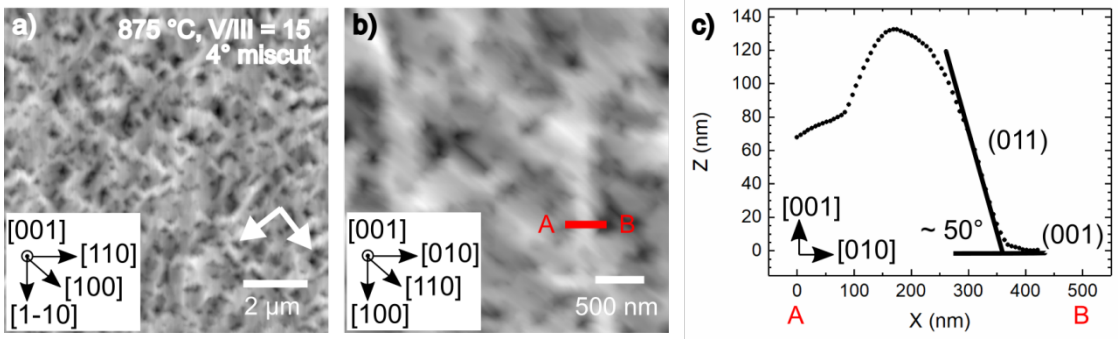

Figure 5.14 (a) 10 × 10 μm^2 AFM scan (fast scan direction = [110]) of the sample grown at the lowest V/III-ratio of 15 showing surface features with their long axes at ~ ± 45° to [110]. The bold white arrows on the image indicate the predominant orientations of the surface features. H = 256 nm. (b) 3.3 × 3.3 μm^2 AFM scan (fast scan direction = [010]) of a typical surface feature in (a) with its long axis at ~ + 45 ° to the [110]. H = 207 nm. (c) Line profile of the facet indicated by the red line (AB) in (b).

Regime ii

In regime ii, as the V/III-ratio increases from 38 to 300, the feature size parallel to the [110] direction ($f_{[110]}$) decreases from (0.79 ± 0.08) μm to about (0.62 ± 0.06) μm (Figure 5.13 (a)), while the feature size in [1-10] direction ($f_{[1-10]}$) increases from (1.78 ± 0.11) μm to (4.8 ± 0.45) μm (Figure 5.13 (b)). As a result, the ratio of $f_{[1-10]}/ f_{[110]}$ increases from 1.8 ± 0.1 at a V/III-ratio of 38 to a maximum of 7.7 ± 1.1 at a V/III-ratio

of 300 (Figure 5.13 (c)). Moreover, the rms roughness increases from (10.7 ± 0.1) nm to (16.5 ± 1.1) nm with increasing V/III-ratio from 38 to 300 (Figure 5.13 (d)).

The feature size results indicate that the formation of the surface morphology is diffusion limited in regime ii. Since N adatoms tend to have a higher sticking coefficient on GaN surfaces than Ga adatoms [32], an increasing density of N adatoms at higher V/III-ratios inhibits diffusion across the -Ga-N- chains on the surface, along the [110] direction. Therefore increasing the V/III-ratio in regime ii has the same diffusion-limiting effect as decreasing the growth temperature in the temperature series (Section 0).

The facets present in regime ii can be identified from the bright-field TEM image (zone axis = [-110], g = 111) of the sample grown at a V/III-ratio of 300 in Figure 5.15 (a), by measuring the angles between the facets and the {111} stacking faults, a sample of which are indicated by the white dashed lines. The TEM images in Figure 5.15 (a) and (b) view along the elongated features shown in the AFM scans in Figure 5.12 (f) and (h), respectively, and it is assumed that any projection issues can be ignored. The (001) surface is marked by the blue dotted lines; {116}, {113} and {112} facets by yellow dashed lines; and {111} facets by red dashed lines. The marked change in surface morphology between regimes i and ii can thus be explained by a change in the relative facet energies between {101} facets in regime i, and {116}, {113}, {112} and {111} facets in regime ii, although surface energies are likely to control the surface morphology in all three regimes. Despite the appearance of a range of facets, we note that the most predominant facet orientation is still (001), and that anisotropic diffusion on this facet will still be a significant factor in controlling the morphology.

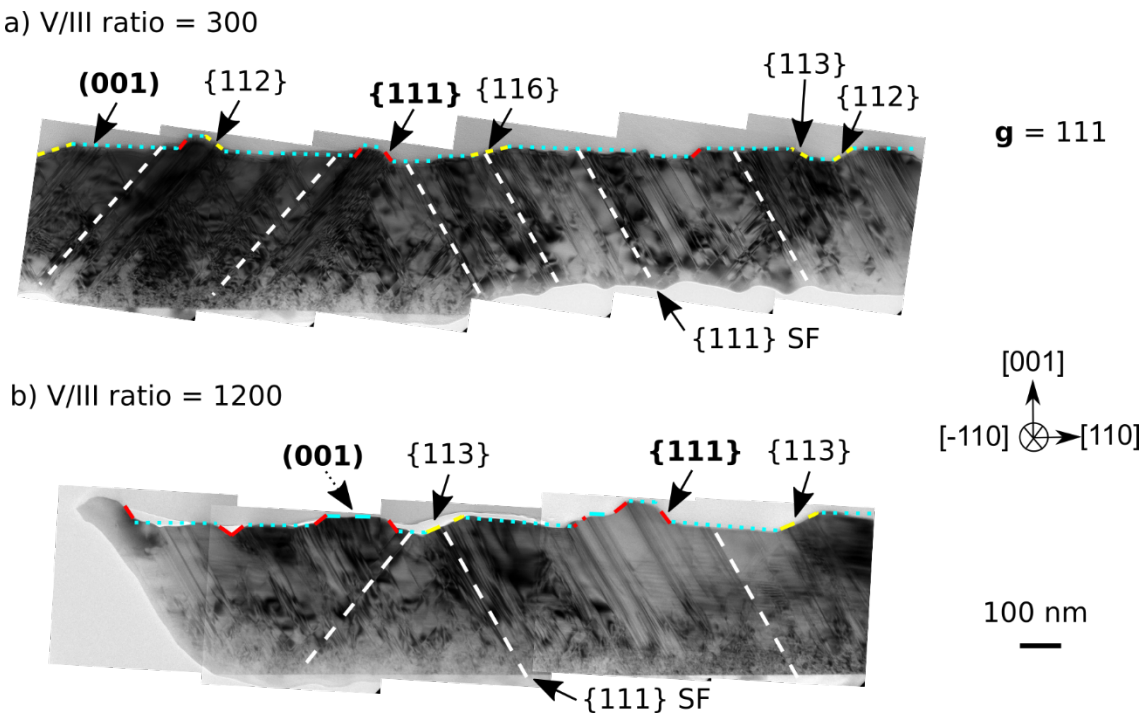

Figure 5.15 Bright-field TEM images of the samples grown at a temperature of 875 °C and (a) V/III-ratio of 300, (b) V/III-ratio of 1200. Imaging conditions: zone axis = [-110], g = 111. For both (a) and (b), the typical {111} stacking fault orientations are indicated by the white dashed lines, the (001) surface by the blue dotted lines, {111} facets by the red dashed lines, and other facets by yellow dashed lines. The facets in (b), the {111} facets in particular, are larger and more pronounced than in (a).

Regime iii

In regime iii, as the V/III-ratio increases from 300 to 1200, the feature size parallel to the [110] direction ($f_{[110]}$) increases from (0.62 ± 0.06) µm to (0.75 ± 0.02) µm (Figure 5.13 (a)), while the feature size in [1-10] direction ($f_{[1\text{-}10]}$) decreases from (4.80 ± 0.45) µm to (2.54 ± 0.29) µm (Figure 5.13 (b)). Hence the feature size ratio, $f_{[1\text{-}10]}/ f_{[110]}$, decreases from (7.7 ± 1.1) at V/III-ratio of 300 to (3.4 ± 0.4) at V/III-ratio of 1200 (Figure 5.13 (c)), displaying the opposite trend to growth regime ii. The rms roughness shown in Figure 5.13 (d) increases only slightly from (16.5 ± 1.1) nm to (19.8 ± 0.5) nm, indicating a much lower dependence on the V/III-ratio than in regime ii.

We propose that in regime iii, the surface becomes saturated with N adatoms, therefore the diffusion limited model of regime ii breaks down. Instead the N-saturated zb-GaN surface seems to encourage the formation of {111} facets. Figure 5.15 (b) shows the bright-field TEM images (zone axis = [-110], g = 111) of the sample grown at the highest V/III-ratio of 1200. The (001) surface is marked by the blue dotted lines; {113} facets by yellow dashed lines; and {111} facets by red dashed lines. The sample grown

at a V/III-ratio of 1200 has larger and more pronounced {111} facets compared with the sample grown at a V/III-ratio of 300 in Figure 5.15 (a). It is thought that the formation of such exposed {111} facets in the zb-GaN epilayer increases the likelihood for the nucleation of wurtzite inclusions, since the {111} zincblende planes and {0002} wurtzite planes differ only in their stacking sequence [79]. Hence, the {111} facets are expected to lead to the presence of a significant proportion of wurtzite phase within the thin film.

Results from XRD analysis in Figure 5.16 show that the proportion of the zincblende phase is between > 98 % and 100 % for the samples grown in regime i and ii. In regime iii, as the V/III-ratio increases from 300 to 1200, the proportion of the zincblende phase decreases to ~ 81 %, with increased proportions of the wurtzite phase and highly defective zb-GaN material. Such results support the view that {111} facets encourage the formation of wurtzite inclusions.

Furthermore, we should note that although the two samples grown at the highest V/III-ratios of 600 and 1200 have lower zincblende phase purity, they have elongated surface morphologies similar to samples with higher zincblende phase purity. This indicates that the surface morphology is not significantly influenced by the presence of wurtzite inclusions. This is consistent with the findings by Kemper *et al.* [64], who observed characteristic elongated surface features in both types of APDs of a zb-GaN sample grown on an on-axis substrate similar to our on-axis sample, as shown in Figure 1.9 (a) and Figure 5.1 (a). Using electron backscatter diffraction (EBSD), they found that one type of APD has a high wurtzite content close to the surface, while the other type of APD has little or no wurtzite content. This again shows that the formation of the surface morphology is not driven by the wurtzite content of the sample.

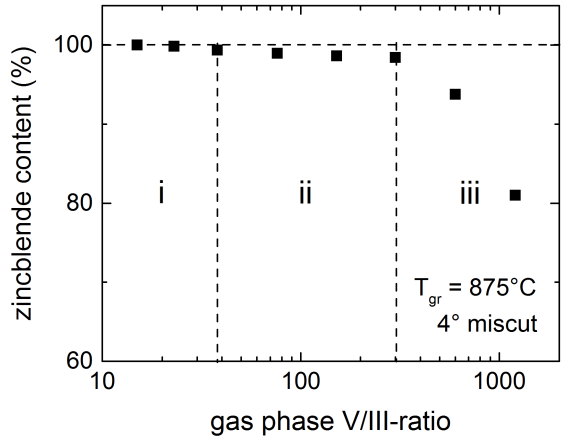

Figure 5.16 Relative intensities of the zb-GaN XRD peaks for samples in the V/III-ratio series at a constant growth temperature of 875 °C. The three different growth regimes are labelled with i, ii and iii. Data from Dr Martin Frentrup.

5.3.4 Effect of reactor pressure

The Normarski optical images of the two series of samples grown at a reactor pressure of 300 Torr where the (a) growth temperature and (b) V/III-ratio are varied are shown in Figure 5.17. The variation of the surface morphology with growth temperature is similar to the samples grown at 100 Torr in Figure 5, where the elongated surface features become more square-like at higher temperatures. As for the V/III-ratio set of samples, the typical elongated features are observed for V/III ratios between 38 and 300, while different regimes appear to operate on the surface for V/III-ratios < 23 and > 600. Such a variation in surface morphology is also comparable to the V/III-ratio series grown at 100 Torr in Figure 5.12.

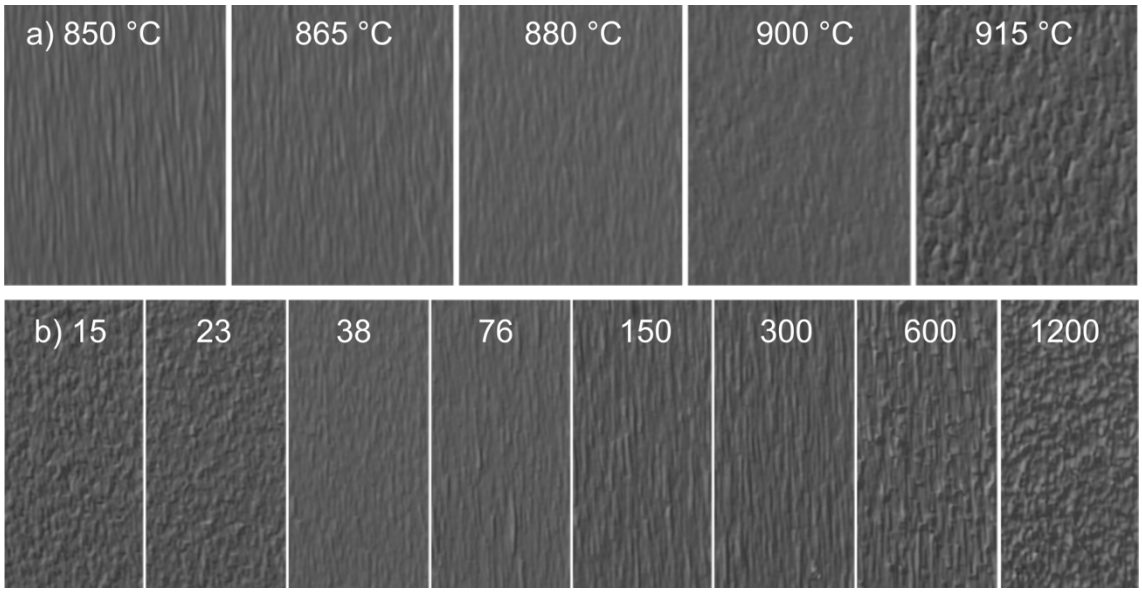

Figure 5.17 Normarski optical images of two sets of samples grown at a reactor pressure of 300 Torr with the variation of (a) growth temperature and (b) V/III-ratio. Data from Dr Menno Kappers.

The wurtzite content of the temperature and V/III ratio series of GaN epilayers grown at 100 Torr and 300 Torr are compared in Figure 5.18. The wurtzite content of samples grown at 100 Torr have consistently lower wurtzite content compared with those grown at 300 Torr, showing that the growth window for high phase purity zb-GaN is larger at the lower reactor pressure of 100 Torr.

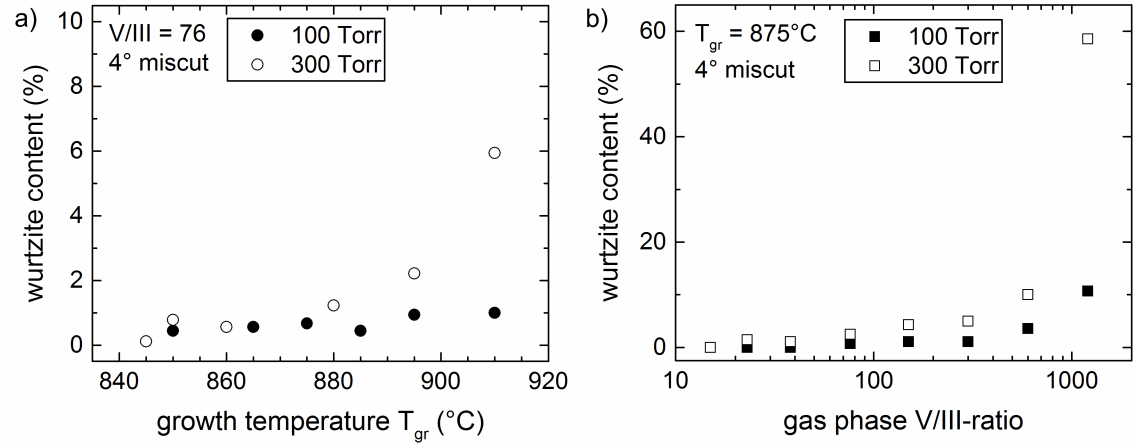

Figure 5.18 Wurtzite content of the (a) growth temperature and (b) V/III-ratio series of GaN epilayers at reactor pressures of 100 Torr and 300 Torr, as determined by XRD. Data from Dr Martin Frentrup.

5.4 Conclusion

We have grown zb-GaN thin films with zincblende phase purities higher than 98 % that exhibit an undulating surface morphology. A substrate miscut angle greater than or equal to 2° in the [110] direction can suppress the formation of undesirable antiphase domains in the GaN epilayer. The surface morphology is similar for zb-GaN grown on 4° and 0° miscut substrates, which indicates that it is not determined by the step-bunching associated with the miscut. The 90° rotation of the surface morphology in neighbouring antiphase domains of zb-GaN grown on a 0° miscut substrate further suggests that the surface morphology is controlled by the symmetry of the crystal surface. The size of the surface features and the rms surface roughness of the thin films can be controlled by the growth temperature and gas-phase V/III-ratio. The dependence on temperature indicates that the formation of such surface features is diffusion limited, which we have explained by considering the atomic structure of the zb-GaN (001) surface plane and the two-fold symmetry of the Ga-N bilayers. The dependence on V/III-ratio revealed three distinct growth regimes, of which the regime at moderate V/III-ratios (regime ii: V/III-ratio of 38 to 300) is diffusion limited. A lower V/III-ratio of 15 resulted in features with {101}-type facets, but we do not have data available to understand the role of surface diffusion in controlling such a surface morphology. At V/III-ratios greater than 600, pronounced {111} facets are believed to increase the likelihood of formation of wurtzite inclusions. For optimised growth of zb-GaN with low surface roughness, we recommend a growth temperature around 885 °C, a V/III-ratio of 38 in the gas phase and a reactor pressure of 100 Torr.

6 Effect of substrate miscut on stacking faults in zb-GaN epilayers

6.1 Introduction

In this chapter, we investigate the influence of the substrate miscut on the distribution and density of {111}-type SFs present in a zb-GaN epilayer grown on a 3C-SiC/Si (001) substrate with a 4° miscut, using analyses by XRD and cross-sectional bright-field TEM. Based on the TEM experimental observations, a simple model of the SF propagation and annihilation in a zincblende epilayer is used to investigate the local distribution of SFs, and to determine how a difference in the densities of two orientations of intersecting {111} SFs at the GaN/SiC interface influences the SF density reduction with increasing epilayer thickness.

6.2 Experimental methods

The zb-GaN epilayer sample investigated was grown by Dr Menno Kappers by MOVPE in a 6 × 2'' Thomas Swan close-coupled showerhead reactor on a ~ 2 × 2 cm^2 piece of a 150 mm diameter 3C-SiC/Si substrate provided by Anvil Semiconductors Ltd. The substrate consisted of a 2.9 μm thick layer of 3C-SiC grown on a 1000 μm thick Si (001) wafer with a nominal 4° miscut towards the [110] in-plane direction. A thin GaN nucleation layer was followed by a ~ 380 nm thick zb-GaN epilayer grown under conditions which suppress the formation of the thermodynamically more stable wurtzite phase. The zb-GaN epilayer growth was carried out at a temperature of 875 °C, a V/III-ratio of 300 with a growth rate of approximately 1.8 μm h^{-1}.

XRD was used to investigate the zincblende phase purity and the global distribution of SFs in the GaN epilayer by Dr Martin Frentrup. Reciprocal space maps of the SF-related diffuse scattering around the on-axis 002 and off-axis 113-type zb-GaN and 3C-SiC reflections were obtained. The XRD measurements were performed in coplanar geometry, in the direction perpendicular to the miscut to investigate the SFs in the [110] zone, and parallel to the miscut to study the [-110] zone. Each measurement collected data from an area of ~ 2 cm^2, which is illuminated by the X-ray beam.

In order to investigate the local SF distribution, two cross-sectional TEM specimens were prepared where the zone axes were either (A) parallel or (B) perpendicular to the miscut direction by mechanical polishing and dimple grinding, followed by precision ion polishing with Ar^+ ions. Cross-sectional bright-field TEM was performed on a FEI Tecnai F20 operated at 200 kV to investigate a total of nine different regions from the two TEM specimens. The schematic in Figure 6.1 shows the (001)-oriented zb-GaN epilayer grown on a 3C-SiC/Si substrate with a miscut in the [110] direction. The black lines in the cross-sections of the GaN layer illustrate the alignment of the four different {111} SFs. The oppositely inclined (-111) and (1-11) SFs which are edge-on when viewed in the [110] zone (shaded blue) are not directly affected by the substrate miscut and thus are both at a theoretical angle of 55° to the GaN/SiC interface. In contrast, the pair of oppositely inclined (-1-11) and (111) SFs which are edge-on when viewed in the [-110] zone (shaded green) have their relative angles to the GaN/SiC interface inclined by the 4° miscut: the (-1-11) SFs are at a shallower angle (51°) and the (111) SFs at a steeper angle (59°) with respect to the GaN/SiC interface.

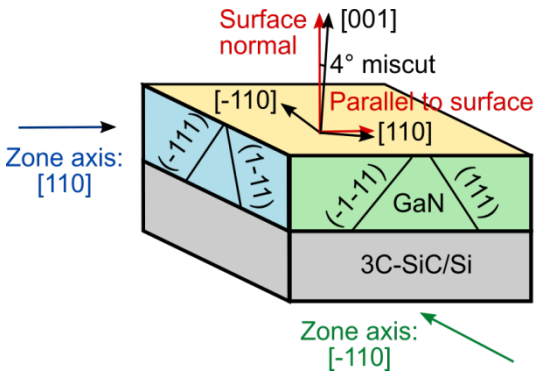

Figure 6.1 Schematic showing the alignment of the four {111}-type SFs in zb-GaN grown on a 3C-SiC/Si substrate with a 4° miscut towards [110]. The [110] zone is shaded blue, while the [-110] zone is shaded green.

The density of a particular orientation of SF was determined at a distance of 380 nm from the GaN/SiC interface, with the consideration of the inclination angle of the SF with respect to the GaN/SiC interface such that the SF density calculated is reflective of the normal distance between the SFs. If we assume that the volume of a sample is a cuboid with the dimensions $L \times w \times t$, the {111}-type SFs of the same orientation are inclined at angle α from the GaN/SiC interface, as shown in Figure 6.2 (a). The area of a SF is $\frac{w}{sin\alpha} \times t$, while the volume of the sample is $L \times w \times t$. Since the SF density is defined as the area of SFs per unit volume of sample, SF density is given by $\frac{n}{sin\alpha \times L}$, where n is the number of SFs in the sample. As our TEM images are two-dimensional projections of such a sample along the thickness t (Figure 6.2 (b)), we can estimate the local stacking fault density $\frac{n}{sin\alpha \times L}$ in units of length^{-1} by counting the number of SFs n (red lines) inclined at angle α from the GaN/SiC interface that cross a reference line (blue dotted line) with length L at a distance 380 nm from the GaN/SiC interface. The blue circles indicate where the SFs cross the reference line.

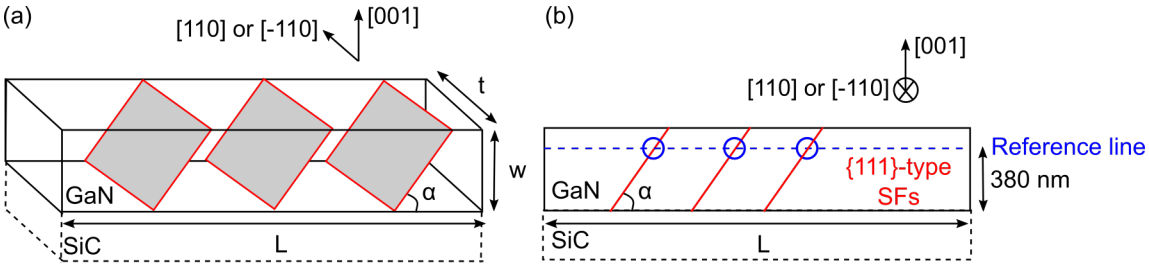

Figure 6.2 (a) 3D schematic of a cuboid sample with the dimensions $L \times w \times t$, containing {111}-type SFs (traced in red) of the same orientation inclined at an angle α from the GaN/SiC interface. (b) 2D schematic of the projection of (a) along the thickness t, where the {111}-type SFs appear as lines (in red) inclined at an angle α from the GaN/SiC interface. The local stacking fault density can be estimated by counting the number of SFs that cross a reference line (blue dotted line).

6.3 Results and discussion

6.3.1 SF distribution in the [110] zone

First, we consider the SF distribution in the [110] zone, in which the inclination angle for both the (-111) and (1-11) SFs is 55° with respect to the GaN/SiC interface and is not affected by the substrate miscut.

Figure 6.3 shows the XRD reciprocal space maps of the off-axis (a) -113 and (b) 1-13 reflections, and (c) the on-axis 002 reflections of zb-GaN and 3C-SiC in the [110]

zone, with the schematic in (d) illustrating their positions in reciprocal space. The low-intensity streaks along the <111> directions that pass through the reflections are caused by diffuse scattering on the {111}-type SFs. The degree of broadening of a reflection is believed to depend strongly on the density of SFs [115]. Since a SF always produces diffuse scattering in the directions normal to its plane, it is possible to attribute a streak to a particular orientation of SF and hence qualitatively compare the densities between the two {111}-type SFs in the zone. The yellow circles in Figure 6.3 mark the expected positions of wurtzite reflections, which are absent in all three reciprocal space maps, revealing that the zb-GaN epilayer has a high phase purity. It is interesting to note that the SF streaks always have a larger broadening towards the nearest wurtzite reflection on the <111> streaks. This is believed to be due to the mixed wz and zb stacking of randomly-spaced SFs leading to an enhanced diffuse scattering in between zb reflections and expected wz reflections.

The 002 zb-GaN reflection in Figure 6.3 (c) is broadened to a 4-pointed star-like shape. It is fairly mirror-symmetrical about the Q_z-axis, and the (1-11) and (-111) SF streaks have similar intensities. This indicates a similar density of the (1-11) and (-111) SFs in the sample. The slightly higher intensity in the bottom left part of the space map ($Q_x < 0.3$) in Figure 6.3 (c) is caused by scattering from surface features as the incident beam was at a very low angle (~1°) to the sample surface. However this does not affect the interpretation of the SF scattering, since there is sufficient distance between the surface scattering and the 002 zb-GaN reflection spot. The observations made from the 002 reflection are also seen from the -1-13 and 113 zb-GaN reflections in Figure 6.3 (a) and (b) respectively. Both 113-type reflections are broadened in the directions of the SF streaks, and are mirror-symmetrical about the surface normal Q_z. Since XRD collects data from a large area of the sample, the results reveal that there is no global preference of the SF inclination in the [110] zone, indicating similar densities of (1-11) and (-111) SFs.

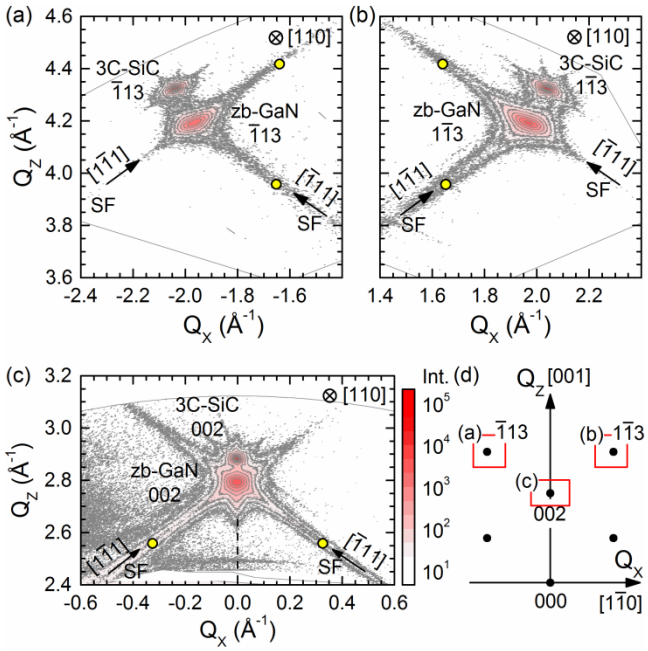

Figure 6.3 XRD reciprocal space maps showing the (a) -113, (b) 1-13, and (c) 002 reflections of zb-GaN and 3C-SiC in the [110] zone, where Q_x and Q_z are parallel and normal to the sample surface respectively. The yellow circles mark the expected positions of wz-GaN reflections, in the case of phase contamination. (d) A schematic illustrating the positions of the reflections in reciprocal space. Figures from Dr Martin Frentrup.

To gain an insight into the local defect distribution, TEM was used to investigate the distribution and density of the different orientations of SFs in the [110] zone. Figure 6.4 shows the cross-sectional bright-field TEM images (zone axis = [110], g = -111) of two of the regions studied. The planar SFs are visible as dark lines running through the thickness of the epilayer. The yellow solid lines highlight examples of (-111) and (1-11) SFs, which are both inclined at 55° from the GaN/SiC interface (white dotted line). The density of SFs near the GaN/SiC interface is very high, but as a result of annihilation, there is a large reduction in SF density within the first 100 nm of the GaN epilayer. Close to the surface of the ~ 380 nm thick epilayer, both orientations of SFs are not distributed evenly and often occur as bunches, as indicated by the arrows in Figure 6.4.

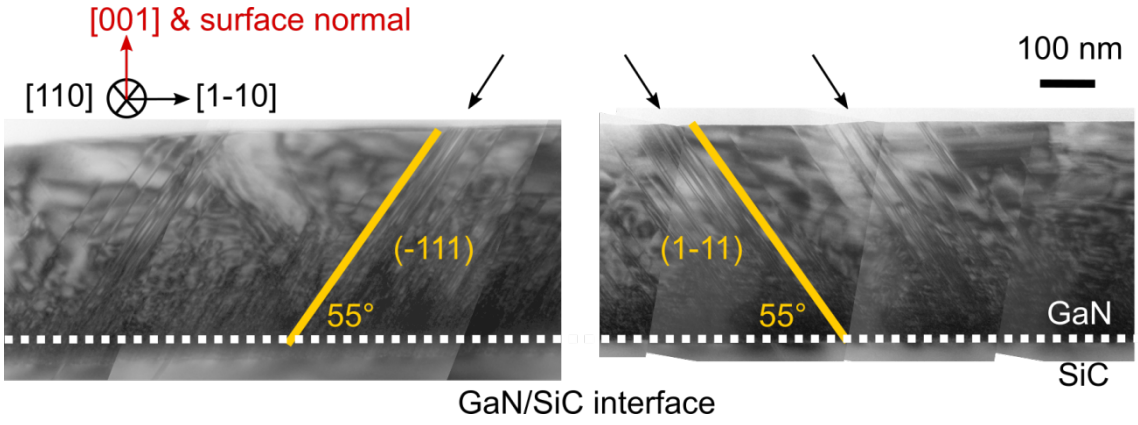

Figure 6.4 Cross-sectional bright-field TEM images of the GaN epilayer with zone axis = [110], g = -111, where the SFs appear as dark lines. The yellow lines highlight the inclinations of the (-111) and (1-11) SFs with respect to the GaN/SiC interface, and the arrows indicate bunches of SFs.

The properties of SFs close to the surface of the 380 nm thick epilayer from four distinct regions of the sample with a total length of 11.2 μm were studied quantitatively. For example, for the TEM images shown in Figure 6.4 with a total length of 2.06 μm, 45 SFs are clearly identifiable in the GaN epilayer measured at distance of 380 nm from the GaN/SiC interface. Note that SFs separated by less than 4 nm cannot be resolved from the TEM images, and hence were counted as a single SF. SF bunches in the four regions contained between 4 and 17 SFs, and the average distance between SFs within a bunch is 16 nm. Table 6.5 provides a summary for each of the four regions studied in the [110] zone, including their length, the ratio of the number of (-111) SFs to the number of (1-11) SFs, and the total SF density. The local density of a particular orientation of SF varies strongly: in three regions (A1 to A3), there are more (-111) SFs than (1-11) SFs. However, in region A4, there are significantly more (1-11) SFs than (-111) SFs. The total SF density does not differ significantly between the four regions and varies from 2.4×10^5 cm $^{-1}$ to 3.0×10^5 cm $^{-1}$. The average SF density of the four regions weighted by their respective lengths is $(2.8 \pm 0.1) \times 10^5$ cm $^{-1}$, while the average density of (-111) SFs and (1-11) SFs are $(1.8 \pm 0.6) \times 10^5$ cm $^{-1}$ and $(0.9 \pm 0.6) \times 10^5$ cm $^{-1}$, respectively. The errors quoted here are the standard error of the mean of the measurements from the four regions.

The results of the TEM analysis show that there is a local anisotropy in the SF inclination. Although somewhat limited by the sampling area of TEM, our results also suggest that there is no global preference for (-111) or (1-11) SFs, supporting the results from the XRD analysis. Later, in Section 3.3, we will use a model to simulate the possibility of a local anisotropy in the SF inclination, arising from the formation of SF bunches in a material which has no global anisotropy of SF inclination.

Region	Length parallel to GaN/SiC interface (μm)	No. of (-111) : No. of (1-11) SFs	Total SF density (× 105 cm -1)
A1	4.9	6.1 : 1	3.0
A2	2.9	4.8 : 1	2.7
A3	1.7	16 : 1	2.4
A4	1.7	1 : 12	2.9

Table 6.5 Summary of the results obtained from the TEM analysis of the [110] zone from four distinct regions.

6.3.2 SF distribution in the [-110] zone

Next, we consider the SF distribution in the [-110] zone, in which the inclination angle of the (-1-11) and (111) SFs with respect to the GaN/SiC interface is affected by the 4° substrate miscut.

Figure 6.5 shows the XRD reciprocal space maps of the off-axis (a) -1-13 and (b) 113 reflections, and (c) the on-axis 002 reflections of zb-GaN and 3C-SiC in the [-110] zone, with the schematic in (d) illustrating their positions in reciprocal space. Due to the miscut, the reflections are tilted by 4° about the [-110] zone axis. This is apparent from a comparison of the schematics in Figure 6.3 (d) and Figure 6.5 (d) which show the positions of the 002 and 113-type reflections. The axes Q_y and Q_z represent the directions parallel and normal to the sample surface respectively, and thus do not coincide perfectly with the [110] and [001] crystal axes due to the 4° substrate miscut. The 4° tilt of the 002 reflection away from the surface normal is marked in the reciprocal space map in Figure 6.5 (c).

In contrast to the [110] zone, the 4-pointed star-like shape of the 002 reflection in Figure 6.5 (c) is not mirror-symmetrical along the Q_z-axis but broadened along the [111] direction, and the (-1-11) SF streak has a significantly lower intensity than the (111) SF streak. A similar anisotropy in the broadening of reflections can be observed in the reciprocal space maps of the -1-13 and 113 zb-GaN reflections in Figure 6.5 (a) and (b) respectively, where the (111) SF streak is more intense than the (-1-11) SF streak.

Hence from XRD analysis, we can conclude that there is a global anisotropy in SF inclination in the [-110] zone, with a significantly higher density of (111) SFs compared with (-1-11) SFs. From the rotation of the reflections and SF streaks in the reciprocal space map, we can determine that SFs tend to form preferentially on the steeper {111} plane with respect to the growth surface.

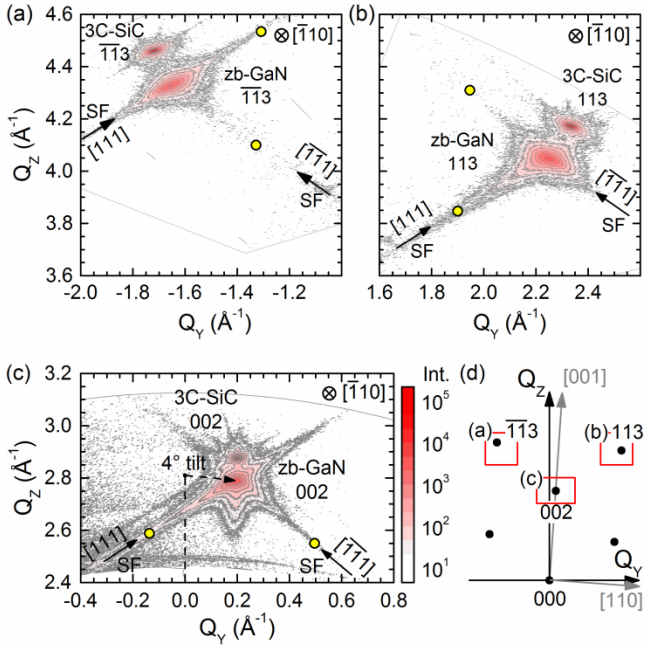

Figure 6.5 XRD reciprocal space maps showing the (a) -1-13, (b) 113, and (c) 002 reflections of zb-GaN and 3C-SiC in the [-110] zone. The yellow circles mark the expected positions of wz-GaN reflections, in the case of phase contamination. (d) A schematic illustrating the positions of the reflections in reciprocal space. Figures from Dr Martin Frentrup.

The observations made by XRD are also supported by the TEM analysis. A cross-sectional bright-field TEM image of a region of the GaN epilayer with zone axis = [-110], g = 111 is shown in Figure 6.6. The yellow solid lines highlight examples of (-1-11) and (111) SFs, which are at ~ 51° and ~ 59° respectively to the GaN/SiC interface (black dotted line); the different inclination angles of the SFs in the [-110] zone are a result of the substrate miscut, as observed in XRD measurements. Note that parts of the GaN/SiC interface and the first 100 nm of the GaN epilayer were milled away during the TEM sample preparation. However, the same two main observations made from the TEM image of the [110] zone (Figure 6.4) can be made in the TEM images of the [-110] zone (Figure 6.6): the high density of SFs in GaN close to the GaN/SiC interface rapidly decreases within the first 100 nm of the epilayer, and the occurrence of SF bunches close to the surface of the epilayer.

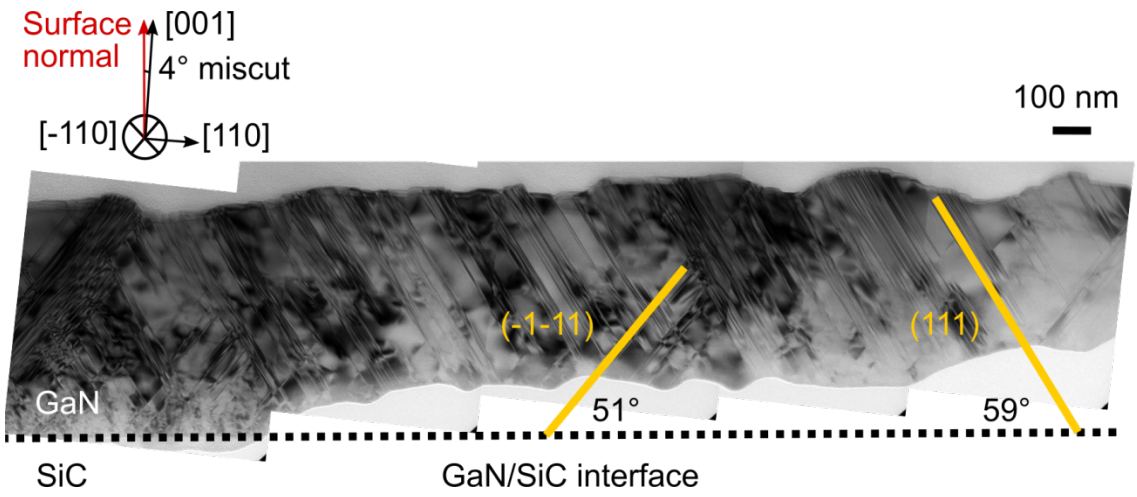

Figure 6.6 Cross-sectional bright-field TEM image of the GaN epilayer with zone axis = [-110], g = 111. The yellow lines highlight the inclinations of the (-1-11) and (111) SFs with respect to the GaN/SiC interface.

The number and orientation of SFs close to the surface of the 380 nm thick epilayer from five distinct regions of the sample with a total length of 10.2 µm were studied. For example, for the TEM image shown in Figure 6.6 with a total length of 2.9 µm, 155 (111) SFs and only 20 (-1-11) SFs are clearly identifiable in the GaN layer at a thickness of ~ 380 nm. Table 6.6 provides a summary of the approximate length of each region studied, the ratio of the number of (-1-11) SFs to the number of (111) SFs, and the total SF density. In all five regions of the sample studied, there are significantly more (111) SFs than (-1-11) SFs, with ratio of (-1-11) to (111) ranging from 1 : 3 to 1 : 29, suggesting a global anisotropy in the SF inclination. There is a significant range in the total SF density between the five regions, from 4.8×10^5 cm $^{-1}$ to 9.4×10^5 cm $^{-1}$, due to the presence of SF bunches in regions B4 and B5. The average SF density across all five regions, weighted by the length of each region, is $(6.5 \pm 1.0) \times 10^5$ cm $^{-1}$, while the average density of (-1-11) SFs and (111) SFs are $(1.1 \pm 0.2) \times 10^5$ cm $^{-1}$ and $(5.8 \pm 1.0) \times 10^5$ cm $^{-1}$, respectively. The error quoted for the SF density values is the standard error of the mean of the measurements from the five regions.

Region	Length parallel to GaN/SiC interface (μm)	No. of (-1-11) : No. of (111) SFs	Total SF density ($\times 10^5$ cm $^{-1}$)
B1	4.7	1 : 3.4	5.2
B2	1.3	1 : 3.0	6.3
B3	1.1	1 : 4.1	4.8
B4	1.6	1 : 6.4	9.4
B5	1.6	1 : 29	9.0

Table 6.6 Summary of the results obtained from the TEM analysis of the [-110] zone from five distinct regions.

Comparing all four orientations of {111} SFs across both zones in Table 6.7, the average density of (111) SFs of $(5.8 \pm 1.0) \times 10^5$ cm $^{-1}$ is significantly higher than that of the other three orientations of SFs, which range from 0.9×10^5 cm $^{-1}$ to 1.8×10^5 cm $^{-1}$. Due to the miscut, the (111) plane is the steepest {111} plane with respect to the GaN/SiC interface. Hence the results from both XRD and TEM lead to the same observation: SF formation occurs more frequently on the {111} plane with the steepest angle to the GaN/SiC interface, and the mis-orientation of the growth surface has a significant influence on the SF density. One possible explanation for the influence of the miscut on the SF density might be that on the miscut SiC surface, step bunches form with {111} microfacets and SFs are preferentially formed on these facets. However, this would be expected to lead to increased stacking fault density on the shallower {111} facet, and not on the steeper facet as we observe in experiments. An alternative explanation might involve differences in strain relaxation mechanisms parallel and perpendicular to the miscut direction, and we are still investigating this possibility.

Zone axis	SF plane	Density ($\times 10^5$ cm $^{-1}$)
[110]	(-111)	1.8 ± 0.6
[110]	(1-11)	0.9 ± 0.6
[-110]	(-1-11)	1.1 ± 0.2
[-110]	(111)	5.8 ± 1.0

Table 6.7 Summary of the average density of all four orientations of {111} SFs in the zb-GaN epilayer at a distance of 380 nm from the GaN/SiC interface, obtained from cross-sectional bright-field TEM images with zone axes [110] and [-110].

The significantly higher density of (111) SFs compared to the other three ((-1-11), (-111), (1-11)) may originate from a preferential formation of (111) SFs during the initial stages of GaN growth, making it less likely for these planar defects to intersect with opposing (-1-11) SFs and annihilate. In Section 6.3.3, we use an SF annihilation and propagation model to test whether this hypothesis is consistent with our observations.

6.3.3 Modelling of the SF annihilation

Our cross-sectional bright-field TEM analysis of the sample shows that when SFs on oppositely inclined {111} planes meet, e.g. when a (-1-11) SF intersects with a (111) SF, there are three possibilities: (a) the two SF lines annihilate each other, (b) one of the SF lines is annihilated while the other propagates through the intersection point, or (c) both of the SF lines propagate, as indicated by the yellow arrows in Figure 6.7. It is possible that each line consists of more than one SF, since the minimum separation between SFs that can be resolved from the TEM images shown here is 4 nm, and SF separations less than this have been observed in zb-GaN epilayers by high-resolution TEM data previously [116]. Hence for Figure 6.7 (b), it could be the case that two SFs intersect with one oppositely inclined SF, resulting in the annihilation of only a pair of SFs. Petr Vacek and Dr Martin Frentrup developed a SF propagation and annihilation model to investigate how the preferential formation of one orientation of {111} SF affects the reduction in SF density with increasing epilayer thickness. The model uses a two-dimensional projection of a face-centred cubic (fcc) lattice viewed from <110> direction and only considers SFs of the same zone. The interactions between both intrinsic and extrinsic SFs are modelled by reactions of Shockley partial dislocations that commonly bound SFs in fcc materials [105], and we have observed Shockley partials dislocations experimentally in our zb-GaN samples by high-resolution scanning TEM (Section 4.3.3). Each SF generated at the SiC/GaN interface is randomly assigned to one of the two {111} planes, and to one of six possible Shockley partial dislocations with Burgers vectors $\mathbf{b}$ = 1/6 <112> on the {111} plane. The spacings between SFs at the SiC/GaN interface are assumed to have a normal distribution described by the mean distance and variance, which are used as input parameters of the model. With increasing epilayer thickness, the SFs are modelled to propagate on {111} planes. At the intersection of two SFs, Frank's rule is applied to determine whether it is energetically favourable for the two partial dislocations associated with the SFs with Burgers vectors $\mathbf{b}_1$ and $\mathbf{b}_2$ to react and form a new dislocation with Burgers vector $\mathbf{b}_3$. [105] If the reaction is energetically favourable ($|\mathbf{b}_3|^2$

$< |\mathbf{b}_1|^2 + |\mathbf{b}_2|^2$), the two SFs annihilate each other; if the reaction is energetically unfavourable ($|\mathbf{b}_3|^2 \geq |\mathbf{b}_1|^2 + |\mathbf{b}_2|^2$), the two SFs continue to propagate into the epilayer. Since the model is two-dimensional and only considers reactions between SFs on oppositely inclined {111} planes of the same zone, it does not cover all the possible reactions between dislocations on all four {111} planes. Despite this simplification, the model is sufficient to make predictions on the distribution and density of SFs.

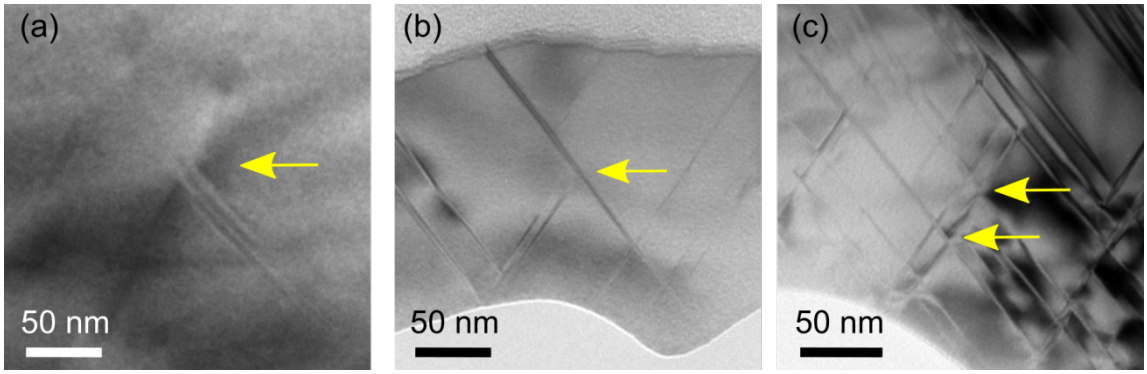

Figure 6.7 Cross-sectional bright-field TEM images of the zb-GaN epilayer with the yellow arrows indicating the three possibilities when oppositely inclined {111} SF lines intersect: (a) the two SF lines annihilate each other, (b) one of the SF lines is annihilated while the other propagates through, and (c) both SF lines propagate through.

Using our SF propagation and annihilation model, we simulated a 400 nm thick and ~ 3.5 μm wide GaN epilayer, with a total of 720 SFs that have a mean separation of 4.78 nm parallel to the GaN/SiC interface (equal to a total SF density of about 2.6×10^6 cm^{-1}) and the variance of the separations is 0.40 nm.

We first simulated the case where the ratio between the two oppositely inclined {111} SFs at the GaN/SiC interface, or the '*starting SF anisotropy*', is 1. The simulation was repeated multiple times to generate different defect arrangements in the GaN epilayer, and a typical result of the simulation is presented in Figure 6.8 (a). In this example, the SF density at the GaN/SiC interface is 2.6×10^6 cm^{-1} and reduces dramatically within the first 100 nm of the GaN epilayer by a factor of 5 to 0.5×10^6 cm^{-1}, reflecting the TEM experimental observations. More significantly, one can observe bunches of both orientations of oppositely inclined {111} SFs close to the surface of the 400 nm thick epilayer, even when the densities of the two orientations of SFs at the GaN/SiC interface are similar. This highlights that even if the SF inclination is essentially isotropic globally in the epilayer, a local anisotropy of inclination due to the presence of SF bunches can result from a normal distribution of the separation between SFs at the GaN/SiC interface. The results of this model are consistent with our observations of the

SFs in the [110] zone from both XRD and TEM.

The situation changes when the densities of the two orientations of oppositely inclined SFs are dissimilar at the GaN/SiC interface, as illustrated in Figure 6.8 (b) where the starting SF anisotropy is 1.5. As with the previous case, a large number of SFs are annihilated within the first 100 nm of the GaN epilayer as they intersect with oppositely inclined SFs. However, with increasing epilayer thickness, bunches of the same orientation of SF preferentially formed at the GaN/SiC interface dominate, since there are not enough of the oppositely inclined SFs in the vicinity to allow annihilation to proceed. The more dominant SF bunches continue to propagate through the thickness of the epilayer and no further reduction in SF density occurs globally. The results of the model in this case are also consistent with our observations of the SFs in the [-110] zone from both XRD and TEM.

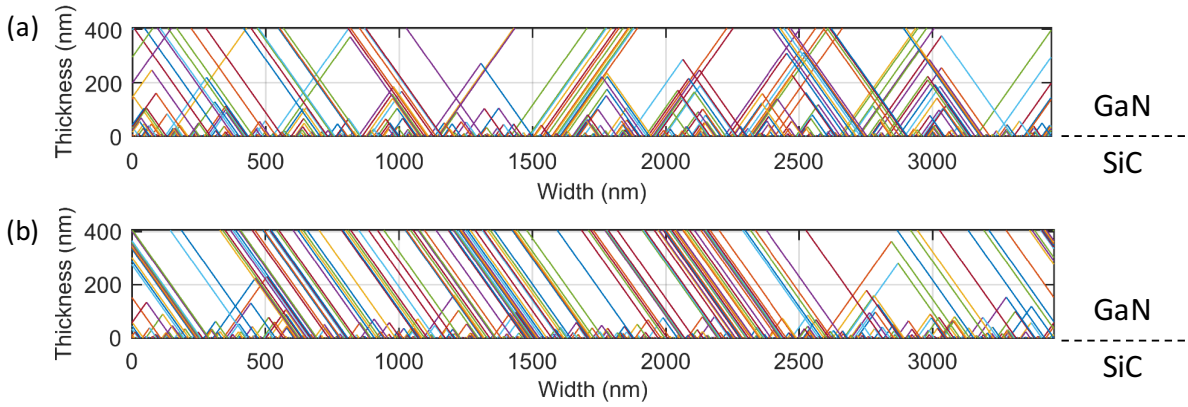

Figure 6.8 Simulation of SF annihilation in a zincblende epilayer that is 400 nm thick and ~ 3.5 µm wide, with (a) no starting SF anisotropy and (b) a 3:2 starting SF anisotropy.

To investigate the effect of a disparity in the density of oppositely inclined SFs at the GaN/SiC interface on the reduction in SF density with epilayer thickness, we simulated the SF densities at a thickness of 380 nm for different starting SF anisotropies, as shown in Figure 6.9. The SF density at the GaN/SiC interface was kept constant at 3.9 $\times$ 10^6 cm^{-1}, by defining the input parameters of the model SF separation mean and variance to be 3.19 nm and 0.25 nm respectively. The SF density at the GaN/SiC interface was selected to be 3.9 $\times$ 10^6 cm^{-1} so that the graph has a point at (1, 2.8 $\times$ 10^5 cm^{-1}) to match with experimental data. Each data point in Figure 6.9 is the average of 10 different SF configurations for a given starting SF anisotropy, and the error bars shown represent the standard error of the mean. The simulations show that the isotropic case, where the starting SF anisotropy is 1, results in the lowest SF density at the surface of the GaN

epilayer. However, as the degree of the starting anisotropy increases and the starting SF anisotropy differs from 1, the SF density measured at a thickness of 380 nm increases. Such results are consistent with the TEM data, where the [110] zone with notionally no starting SF anisotropy has a lower SF density at 380 nm away from the interface than the [-110] zone with an anisotropy related to the miscut. The results also support our hypothesis that a disparity in the density of oppositely inclined SFs at the GaN/SiC interface results in a lower chance of annihilation for the orientation of SF that has a higher starting density, thus reducing the efficiency of the SF annihilation process, and limiting the reduction in SF density with epilayer thickness.

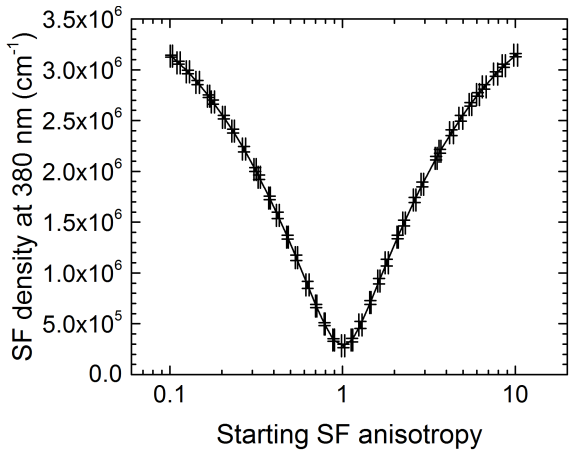

Figure 6.9 Plot of simulated SF densities for a GaN epilayer at a thickness of 380 nm against the starting SF anisotropy. The SF density at the GaN/SiC interface is 3.9×10^6 cm^{-1}. Note the logarithmic scale of the x-axis.

Figure 6.10 is a zoomed-in plot of Figure 6.9, focussing on the starting SF anisotropy values between 0.5 and 2. If we assume that the SF density at the GaN/SiC interface is constant irrespective of starting SF anisotropy, the model predicts a starting SF anisotropy of 0.72 ± 0.05 for a SF density at 380 nm of $(6.5 \pm 1.0) \times 10^5$ cm^{-1}, which was measured for the [-110] zone experimentally.

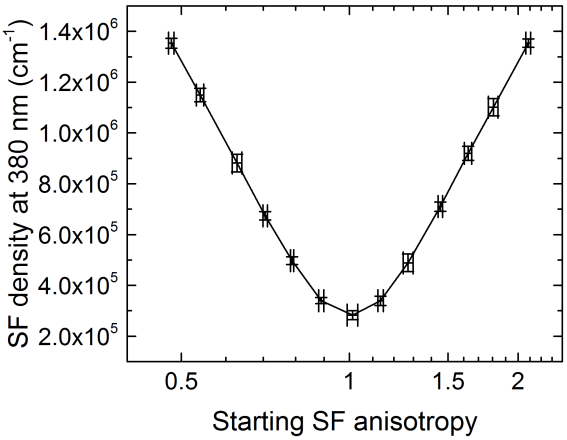

Figure 6.10 Zoomed-in plot of Figure 6.9, focussing on the starting SF anisotropy values between 0.5 and 2.

6.4 Conclusions

A miscut is necessary to suppress the formation of APDs in zincblende GaN grown on 3C-SiC/Si substrates. XRD and TEM results both show a higher SF density in the [-110] zone than the [110] zone of a zincblende GaN epilayer grown on a 3C-SiC/Si (001) substrate with a 4° miscut towards [110], and that this global anisotropy in SF inclination is caused by a higher density of SFs lying on the steeper {111} plane to the GaN/SiC interface. A model simulating the SF propagation and annihilation confirms the occurrence of local SF density fluctuations due to the formation of bunches of one orientation of SF while the SF density remains isotropic globally, as was experimentally observed. The model further shows that a difference in the density of oppositely inclined SFs at the GaN/SiC interface results in a significantly higher density near the GaN surface at a thickness of 380 nm of the orientation of SF that had a higher starting density at the interface. The combined experimental and theoretical results imply that the miscut of the substrate affects the relative densities of {111}-type SFs generated at the GaN/SiC interface, reduces the efficiency of the SF annihilation process, and hence the global reduction of SF density with increasing epilayer thickness. For a good balance between preventing the formation of APDs and efficient SF annihilation, further investigation on a miscut series is required to find an optimal miscut angle. If, in the application of SiC/Si substrates, it proves impossible to avoid APD formation without introducing a miscut, then our results suggest that the miscut will define the minimum SF density which can be achieved by increasing the layer thickness. Therefore, other methods of SF density reduction will need to be explored, either in terms of changes to the nucleation layer which reduce the starting SF density, or alternative methods to block SF propagation

through the layer. An amorphous interlayer might be successful in stopping the propagation of SFs but could result in the nucleation of wz-GaN.

7 Effect of stacking fault bunches on the optical properties of zb-GaN epilayers

7.1 Introduction

The low-temperature photoluminescence (PL) spectra of two zb-GaN epilayers grown at different temperatures consist of peaks and bands with different intensities, in particular a high energy band (HEB) with energies between the band gaps of zincblende and wurtzite GaN is present for the sample grown at the higher temperature and absent for the sample grown at the lower temperature.

In literature, narrow peaks [53,117,118] and a broader emission band [119] within such a range of energies in low-temperature PL spectra of zb-GaN films have been attributed to wurtzite inclusions.

Basal plane stacking faults (BSFs) in wurtzite GaN are known to act as emitters [120]. Such BSFs are suggested to be type-II quantum wells [77], hence stacking faults (SFs) in zinblenede GaN should also act as type-II quantum wells with opposite band alignment. The band alignments near a BSF in wurtzite GaN and a SF in zincblende GaN are illustrated in the schematics in Figure 7.1 (a) and (b), respectively. Therefore, it has also been suggested that SFs in zb-GaN films could confine carriers and result in the HEB. [121] Since stacking faults are the main planar defect in zb-GaN and have been observed to occur in bunches in Chapter 6, it is likely that they will have a role in PL emission processes.

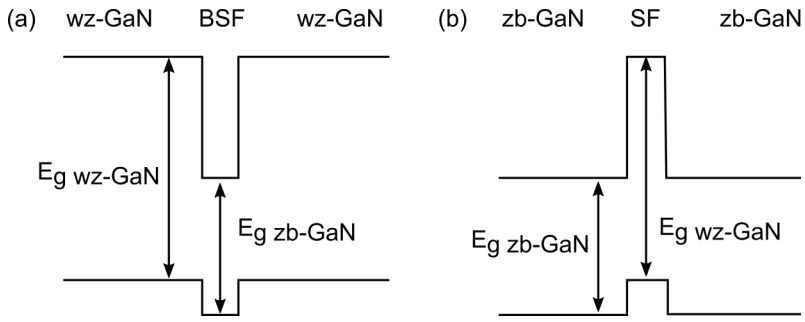

Figure 7.1 Schematics of the band alignment near (a) a basal plane stacking fault in wurtzite GaN and (b) a stacking fault in zincblende GaN.

The aim of this chapter is to investigate whether structural factors, including the wurtzite content, the density and spatial distribution of stacking faults in the epilayers, could explain the HEB and the discrepancy of the PL spectra between the two samples. The impact of impurity incorporation at different growth temperatures on the optical properties is also considered.

7.2 Experimental methods

The zb-GaN epilayer samples investigated were grown by MOVPE in a 6 × 2'' Thomas Swan close-coupled showerhead reactor by Dr Menno Kappers. The 3C-SiC/Si substrate provided by Anvil Semiconductors Ltd consists of a 2.9 μm thick layer of (001)-oriented 3C-SiC grown on a 1000 μm thick Si wafer with 4° miscut towards the [110] in-plane direction. For each ~ 2 × 2 cm^2 sample, a thin GaN nucleation layer was grown on the 3C-SiC/Si substrate, followed by a 650 nm thick GaN epilayer grown under conditions which suppress the formation of the thermodynamically more stable wurtzite phase. The zb-GaN epilayer growth was carried out at a temperature of 950 °C and 885 °C, a V/III-ratio of 300, and a reactor pressure of 100 Torr with a growth rate of approximately 1.5 μm h^{-1}. Trimethylgallium (TMG) and ammonia (NH_3) were used as Ga and N sources, and hydrogen was used as the carrier gas during growth.

Photoluminescence (PL) spectroscopy of the two samples was performed by Stephen Church at 10 K in a temperature controlled closed-cycle helium cryostat, and exciting it with a continuous-wave 325 nm He-Cd laser with a power density of 10 W cm^{-2}.

The proportions of zincblende, wurtzite and highly defective zincblende phases of the GaN epilayers were determined by XRD by Dr Martin Frentrup using a PANalytical

Empyrean diffractometer equipped with a two-bounce hybrid monochromator (λ = 1.54056 Å), 1/4° primary beam slit, and a PIXcel solid-state area detector. Reciprocal space maps of the 113 zb-GaN and 1-103 wz-GaN reflections with their stacking fault-related intensity streaks were collected in asymmetric geometry. These intense reflections were chosen, since they are relatively close to each other, and are unaffected by or do not contain contributions from surface scattering effects.

Cross-sectional TEM samples with a zone axis parallel to the [-110] direction were prepared by mechanical grinding and polishing, and ion milling with Ar^+ ions. Bright-field TEM by a FEI Tecnai F20 operated at 200 kV was used to image the stacking faults (SFs) in the GaN epilayer of the samples. High-resolution TEM was performed on the FEI Tecnai F20 and a JEOL 4000 operated at 400 kV. Since the penetration depth of the laser used for PL is around 100 nm, the key area of interest for comparison with the PL data is approximately within the top 100 nm of the epilayer. Hence the stacking fault density of the sample was measured at 100 nm from the surface of the epilayer from the bright-field TEM images. As explained in Section 6.2 and referring to Figure 7.2, the local stacking fault density $\frac{n}{sin\alpha \times L}$ in units of length^{-1} was estimated by counting the number of SFs n (red lines) inclined at angle α from the GaN/SiC interface that cross a reference line (blue dotted line) with length L at 100 nm from the surface of the epilayer.

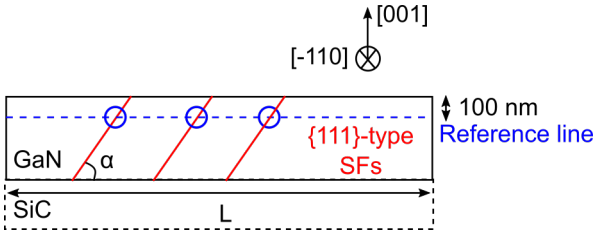

Figure 7.2 Schematic of a cross-sectional bright-field image of a GaN epilayer sample studied in this chapter. The {111}-type SFs appear as lines (in red) inclined at an angle α from the GaN/SiC interface. The local stacking fault density can be estimated by counting the number of SFs that cross a reference line (blue dotted line).

7.3 Results and discussion

The PL spectra for the zb-GaN epilayer samples grown at 950 °C and 885 °C are shown in red and blue respectively in Figure 7.3, with the peaks and bands of the spectra labelled. A peak refers to a narrower region of the PL spectrum and is centred at a particular energy, while a band is a wider region of the spectrum and spans over a range of energies. The PL spectrum of the sample grown at 950 °C has a low energy band (LEB)

at energies below 3.1 eV; a donor-acceptor pair (DAP) peak at 3.175 eV; a donor-bound excitons (D^0X) peak at 3.225 eV; and a high energy band (HEB) with a peak energy of around 3.4 eV and a FWHM of 200 meV that extends above the band gaps of zb-GaN (3.3 eV) and wz-GaN (3.5 eV) at 10K. As for the PL spectrum of sample grown at a lower temperature of 885 °C, the HEB is absent. Compared with the sample grown at 950 °C, the DAP peak is more intense and blueshifted, and the LEB is of lower intensity. A D^0X peak could be concealed by the DAP peak.

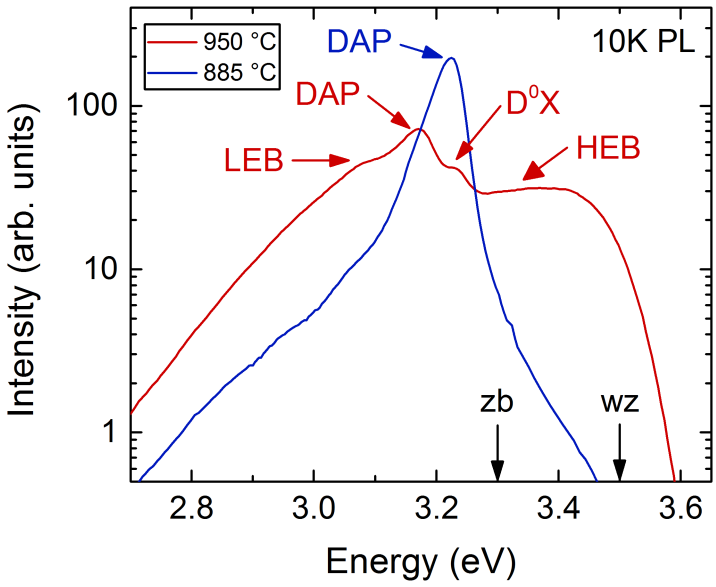

Figure 7.3 The photoluminescence spectra for the zb-GaN epilayers grown at 950 °C and 885 °C obtained under continuous-wave excitation with a 325nm He-Cd laser. The peaks and bands of the spectra are labelled: low energy band (LEB), donor-acceptor pair (DAP) peak, donor-bound excitons (D^0X) peak, high energy band (HEB). The nominal band gaps of zb-GaN (3.3 eV) and wz-GaN (3.5 eV) are labelled on the x-axis. Data from Stephen Church.

The HEB has been attributed to inclusions of wz-GaN in literature [25,53,118,119,122], hence XRD is used to investigate any differences in the proportion of wurtzite and zincblende phases in the GaN epilayer of the two samples. From the XRD reciprocal space maps of the 113 zb-GaN and 1-103 wz-GaN reflections, the intensity profiles along the [111] direction (grey circles) were extracted and are shown in Figure 7.4. The contributions of the zincblende (blue) and wurtzite (green) phases were modelled by fitting Pseudo-Voigt functions to the intensity profile at the theoretical positions of ~ 4.03 $Å^{-1}$ and ~ 3.64 $Å^{-1}$, respectively. A third Pseudo-Voigt function was fitted in between the zincblende and wurtzite fits to consider the contributions from highly defective zb-GaN regions (orange). The integrated intensities of these fits were then used to quantify the

proportions of each phase.

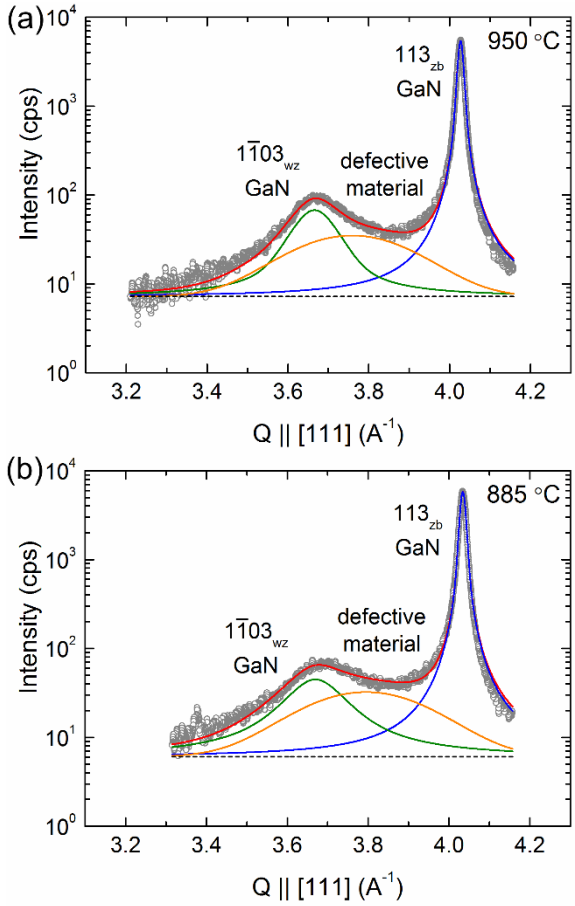

Figure 7.4 XRD intensity profile through the 1-103$_{wz}$ and 113$_{zb}$ reflections (grey circles) for the samples grown at (a) 950 °C, and (b) 885 °C. Pseudo-Voigt fits for the zb-phase (blue), wz-phase (green), and defective zb-GaN material (orange) were used to estimate the proportions of each phase. Data from Dr. Martin Frentrup.

The proportions of zincblende, wurtzite and highly defective zincblende phases in the GaN epilayers determined from XRD analysis are presented in Table 7.8. The proportions of wurtzite in the samples grown at 950 °C and 885 °C are (7.5 ± 1) % and (6.6 ± 1) % respectively, showing that there is no significant difference in the wurtzite proportions between the two samples. Therefore XRD reveals that the difference in the PL spectra cannot be attributed to differences in the wurtzite content between the two samples.

	Proportion (%)		
Growth temperature (°C)	zb-GaN	wz-GaN	Highly defective zb-GaN
950	85.0	7.5	7.5
885	86.6	6.6	6.8

Table 7.8 Proportions of zincblende, wurtzite and highly defective zincblende phases in the GaN epilayers grown at 950 °C and 885 °C determined from XRD analysis. Data from Dr. Martin Frentrup.

We then proposed that the difference in the PL spectra between the two samples could arise from the difference in density or spatial distribution of stacking faults (SFs) in the zb-GaN epilayer. The latter suggestion stems from the TEM data in Chapter 6, which has shown the presence of bunches of SFs with a range of separations between SFs from less than 4 nm to ~ 40 nm. Stephen Church [116] developed a model for the band alignment next to SFs to investigate how the separation between SFs can affect PL emission energies. In the model, SFs act as quantum well barriers and the zincblende GaN material in between the SFs act as quantum wells, since a SF in a zincblende lattice consists of two monolayers of wurtzite material, and wurtzite GaN has a larger band gap than zincblende GaN. The time-independent Schrödinger equation was solved for the electrons and holes in the quantum wells or quantum well-like regions created by the SFs and zb-GaN regions, for a range of different SF separations. The difference in the energies between electrons and holes (or the electron-hole energy) is presented in Figure 7.5, which shows that for SF separations between 1.5 nm and 37 nm, the range of calculated electron-hole energies varies by 230 meV, corresponding well with the width of the HEB observed in the PL spectrum of the sample grown at 950 °C. Therefore, the model and calculations show that SF separations can affect PL emission energies, and predicts that the HEB in the PL spectrum of the higher temperature sample arises from a range of separations between SFs between 1.5 nm and 37 nm that is absent for the lower temperature sample. Hence TEM and HRTEM were used to investigate any differences in the density and spatial distribution of SFs between the two samples, with the results presented below.

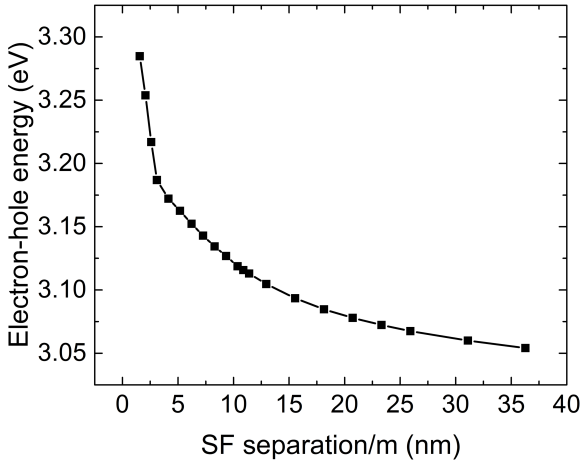

Figure 7.5 Electron-hole energies calculated for different SF separations using the model developed by Stephen Church. Graph from Stephen Church.

The selected-area TEM diffraction patterns of both samples do not indicate the presence of large wurtzite inclusions, supporting the XRD analysis of a zincblende phase purity of at least 85%. The cross-sectional bright-field TEM images of (a) the sample grown at 950 °C (zone axis = [1-10], **g** = 002) and (b) the sample grown at 885 °C (zone axis = [-110], **g** = 002) are shown in Figure 7.6. The SFs in the [-110] zone are visible as dark lines through the thickness of the epilayer. The yellow solid lines highlight examples of (-1-11) and (111) SFs, where the (-1-11) SF and (111) SF are at angles of ~ 51° and ~ 59° from the GaN/SiC interface (white dotted line), respectively, due to the 4° substrate miscut. Similar to the TEM observations made in Chapter 6, the density of SFs close to the GaN/SiC interface is very high, but as a result of annihilation, there is a large reduction in SF density within the first 100 nm of the GaN epilayer. The SFs are not evenly distributed close to the surface of the GaN epilayer and occur as bunches, with a range of separations between SFs. This has also been observed in the TEM data and the SF propagation and annihilation model in Chapter 6.

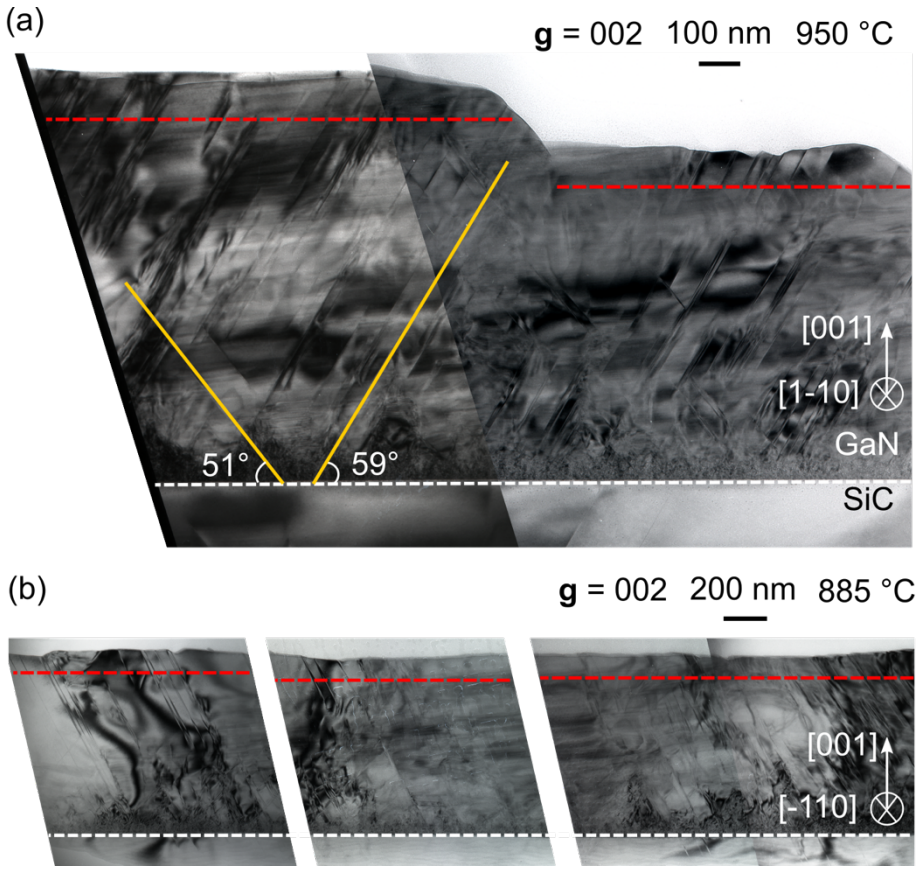

Figure 7.6 (a) Cross-sectional bright-field TEM images of the sample grown at 950 °C used to determine the SF density of the sample. Imaging conditions: zone axis = [1-10], **g** = 002. (b) Cross-sectional bright-field TEM images of the sample grown at 885 °C used to determine the SF density of the sample. Imaging conditions: zone axis = [-110], **g** = 002.

The number of SFs close to the surface of the epilayer of the samples were measured. For the sample grown at 950 °C, two distinct regions with a length of 2.1 μm parallel to the GaN/SiC interface was studied; while for the sample grown at 885 °C, three distinct regions with a total length of 3.9 μm parallel to the GaN/SiC interface were studied. Table 7.9 provides a summary of number of SFs, length, and SF density of each region studied.

Growth temperature (°C)	Region	No. of SFs	Length of reference line (nm)	SF density (× 10^5 cm^{-1})
950	1	11	625	2.1
	2	6	553	1.3
	3	14	858	1.9
885	1	19	1087	2.0
	2	14	1082	1.5
	3	22	1718	2.3

Table 7.9 Summary of number of SFs, length, and SF density of the regions studied in the GaN epilayers grown at 950 °C and 885 °C.

The average SF density is $(1.7 \pm 0.2) \times 10^5$ cm^{-1} for the sample grown at 950 °C, and $(2.0 \pm 0.3) \times 10^5$ cm^{-1} for sample the sample grown at 885 °C, where the errors quoted are the standard errors. Another source of error for the determination of the SF density from the bright-field images is the minimum separation between SFs that can be resolved in the TEM images of the sample. SFs that were separated by less than 7 nm could not be clearly distinguished, and would be imaged as one SF in the bright-field images. From the high-resolution TEM analysis presented later in this chapter, around 20% of the SFs are separated by less than 7 nm apart (see Table 7.10). Therefore, the stacking fault densities may be underestimated by approximately 0.3×10^5 cm^{-1} for the sample grown at 950 °C, and 0.4×10^5 cm^{-1} for the sample grown at 885 °C.

The difference between SF densities of the two samples is 0.3×10^5 cm^{-1}, which is smaller than the errors associated with the SF densities. With small sampling sets for both samples consisting of only three data points, a Student's t-test [123] was employed to determine if the difference between the SF densities of the two samples were statistically significant. The null hypothesis was that the means of the SF densities from the two samples are the same. The outcome of the Student's t-test shows that the probability for the null hypothesis is 0.6, which is greater than 0.5, indicating that the null hypothesis is valid. Hence analysis of the bright-field TEM data shows that there is no significant difference in SF density between the two samples.

High resolution TEM was then used to investigate the distribution of the separation between SFs, including those which are less than 7 nm for the two samples. Figure 7.7 shows an example of a high resolution TEM image of one of the regions in the sample grown at 950 °C. A bunch of SFs may be observed, while the surrounding area has zincblende stacking. The separations between SFs within the bunch are labelled and vary between 1.1 nm to 3.0 nm. For the sample grown at 950 °C, 10 distinct regions were imaged, which contain in total 17 SFs, each with a length of 28 nm. 8 out of the 10 regions imaged contain only a single SF, hence while the minimum separation with a neighbouring SF can be determined, the exact separation between SFs cannot be measured. For the sample grown at 885 °C, 7 SFs were identified in 2 distinct regions, each with a length of 105 nm.

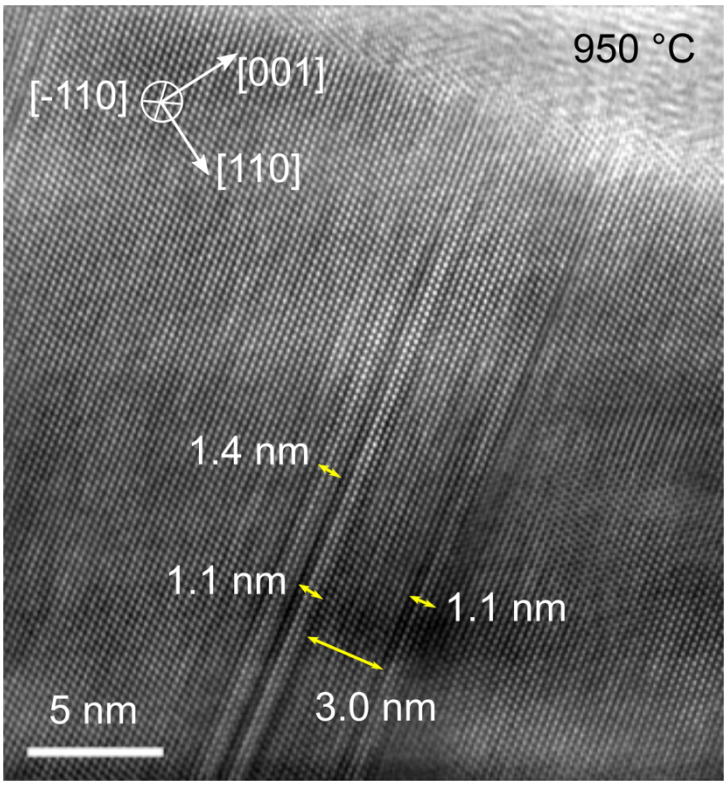

Figure 7.7 High-resolution TEM image of a bunch of stacking faults in the GaN epilayer grown at 950 °C, with the separation between stacking faults in the bunch labelled.

The separation between SFs was measured from both bright-field and high-resolution TEM images of the two samples, including 31 SF separations imaged in regions of the sample grown at 950 °C with a total length of 2.0 μm, and 29 SF separations imaged in regions of the sample grown at 885 °C with a total length of 2.4 μm. The proportion of SF separations that are less than 7 nm, and hence cannot be resolved from the bright-field TEM images, is calculated to be ~ 20 %, as shown in Table 7.10.

Growth temperature (°C)	No. of SF separations	No. of SF separations < 7nm	% of SF separations < 7 nm	Total length of regions (nm)
950	30	6	20	2038
885	29	5	17	2407

Table 7.10 Summary of the SF separation analysis on the GaN epilayers grown at 950 °C and 885 °C.

To compare the distribution of SF separations between the two samples, the SF separations are plotted in normalised histogram with a bin size of 10 nm, as presented in Figure 7.8. The histograms do not appear to show a significant difference in the distribution of SF separations between the two samples.

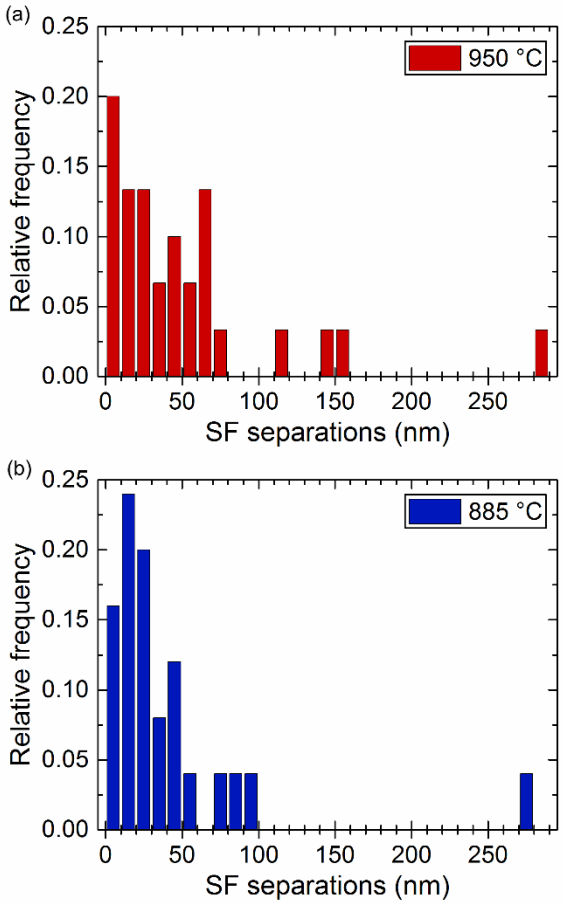

Figure 7.8 Normalised histogram of the stacking fault separations in the GaN epilayers grown at (a) 950 °C and (b) 885 °C.

Overall, TEM analysis does not show any significant structural differences in the density and spatial distribution of SFs between the two samples that could explain the presence of the HEB and the difference in intensities of the peaks and bands in their PL spectra. Therefore our proposal that the differences in the PL spectra between the two samples arose from a difference in density or spatial distribution of the SFs is unlikely to be correct.

With the elimination of wurtzite content, SF density and SF distribution as the factors that result in the differences in PL spectra between the two samples, we have a final alternative explanation. Comparing the PL spectra of the two samples, an increase in the intensity of the DAP peak for the sample grown at 885 °C was coupled with the absence of a HEB and a decrease in intensity of the rest of the spectrum, compared with the sample grown at 950 °C. Therefore we speculate that the differences in the intensities of the different bands and peaks between the PL spectra of the two samples are due to competition for carriers between the various PL recombination processes. Since impurities, such as O and C, can contribute to the DAP peak, the differences observed

between the two samples grown at different temperatures could be related to different impurity levels. It has been shown in literature that growth temperature affects the concentration of O and C impurities in GaN films. For example, Parish *et al.* [124] found that the concentration of C increased from 6×10^{16} cm^{-3} to 2×10^{17} cm^{-3} as the growth temperature decreased from 1070 °C to 1000 °C for wurtzite GaN films grown by MOVPE. Secondary-ion mass spectrometry (SIMS) performed on the samples show that the O concentrations in the samples grown at 950 °C and 885 °C are 3×10^{19} cm^{-3} and 9×10^{16} cm^{-3} respectively. To verify if the concentrations of the impurities do indeed result in the differences in the PL spectra between the two samples, a future PL study could be performed on a series of samples where the variable is O content, and another series of samples where the variable is C content, with the growth temperature kept constant in both series. Moreover, it would also be worthwhile for future studies to consider whether there is any interaction between the stacking faults or wurtzite regions and the impurities at the two growth temperatures, and if so how this might affect understanding of the data in this study.

While XRD showed ~ 7% wurtzite material present in the two zb-GaN samples, we have not obtained TEM evidence of such inclusions in the two samples. Since TEM probes a much smaller local area than XRD, it is most likely that we have sampled too small a volume of material to encounter the wurtzite inclusions in the HRTEM data.

7.4 Conclusion

The PL spectrum of the GaN epilayer grown at 950 °C, has a high energy band (HEB) with a peak energy of around 3.4 eV and a FWHM of 200 meV; while for the PL spectrum of the GaN epilayer grown at a lower temperature of 885 °C, the HEB is absent but the donor-acceptor pair (DAP) peak is more intense. The HEB is usually attributed to wurtzite inclusions in zincblende GaN in literature, but XRD shows similar wurtzite contents of 85.0 % and 86.6 % for the samples grown at 950 °C and 885 °C respectively, showing that differences in wurtzite content alone cannot explain the differences between the PL spectra. The SF densities of the samples from TEM, where the minimum resolvable SF separation is 7 nm, show no significant differences between the two samples. A model, where the SFs act as quantum well barriers and the zincblende material between SFs act as quantum wells, shows that the HEB could arise from SF bunches where the range of separation between SFs is from 1.5 nm to 37 nm. However, the

distributions of SF separations from TEM and high-resolution TEM of the two samples are also similar, therefore the differences in the stacking fault distribution alone cannot explain the differences in the spectra between the two samples. The difference in the intensities of the peaks and bands in the PL spectra of the samples, in particular the DAP peak and HEB, are instead speculated to be due to the differences in the concentration of impurities, such as O and C, which could result in changes in the competition for carriers between the various PL recombination processes associated with the different peaks and bands.

8 Conclusion and future work

8.1 Conclusion

The structural properties of zb-III-nitride grown on 3C-SiC/Si substrates by MOVPE have been investigated, with the aim of realising a zb-GaN-based green-wavelength LED. This work has studied the surface morphology and defects (stacking faults in particular) of zb-GaN nucleation layers that were less than 44 nm thick, and thicker epilayers that were more than 300 nm thick.

We determined that the optimal GaN nucleation layer thickness above which the substrate becomes fully covered is 22 nm (Chapter 3). Full coverage of the substrate by the nucleation layer was important to ensure a high phase purity and pit-free epilayer grown subsequently. Both as-grown and annealed GaN nucleation layers were revealed to be crystalline (Chapter 4).

Antiphase domains in the GaN nucleation layers and epilayers can be suppressed by introducing a miscut angle greater than or equal to 2° in the [110] direction to the 3C-SiC/Si substrate (Chapters 3 & 5). The surface morphology of the nucleation layers grown on substrates with a 4° and 2° substrate miscut consisted of elongated features (Chapter 3). Such an anisotropic surface morphology was also observed on thicker GaN epilayers grown on substrates with the same miscut, and were found to be controlled by the reduced symmetry of the top monolayer of the (001)-oriented zb-GaN lattice (Chapter 5). The size of the surface features and the rms surface roughness of the thin films can be controlled by the growth temperature and gas-phase V/III-ratio. A growth temperature of around 885 °C, a V/III-ratio of 38 in the gas phase and a reactor pressure of 100 Torr were recommended (Chapter 5).

Although substrate miscut can prevent the formation of antiphase domains, combined experimental and theoretical results implied that the 4° substrate miscut resulted in the preferential formation of stacking faults lying on the steeper {111} plane to the GaN/SiC interface (Chapter 6). This has several consequences:

(1) the efficiency of the annihilation process between oppositely inclined {111} stacking faults is reduced, and hence the reduction of stacking fault density with increasing epilayer thickness becomes smaller;
(2) we cannot simply grow thicker epilayers to eliminate stacking faults, as there are not enough pairs of stacking faults to annihilate each other, and the stacking fault density tends to a certain value with increasing layer thickness;
(3) stacking faults occur in bunches, which were modelled to act as quantum wells and were shown to result in photoluminescence energies above the band gaps of zb- and wz-GaN (Chapter 7).

The annihilation of stacking faults in thick epilayers also depends on the starting stacking fault density at the GaN/SiC interface (Chapter 6). Stacking faults are suggested to arise from the lattice mismatch between zb-GaN and SiC, since stacking faults and misfit dislocations were found close to the GaN/SiC interface and within islands prior to the coalescence of nucleation layer islands (Chapter 4).

The main challenges to the development of a zb-GaN-based LED identified in this work are the relatively rough zb-GaN surface morphology compared with wurtzite GaN, and the high density of stacking faults in the GaN epilayer.

GaN epilayers with smooth surfaces are required for the subsequent growth of InGaN/GaN quantum wells. However, we have shown that the surface roughness of our zb-GaN films arises from the elongated surface features, which are formed as a result of the crystallography of zb-GaN. Although the anisotropic surface morphology would be difficult avoid, future work could focus on ways to reduce the amplitude of the surface roughness.

Stacking faults were the dominant defect found in zb-GaN epilayers. It is important to reduce the high density of stacking faults, which are likely to have an impact on the light emission of an LED. This could be achieved by a better balance between substrate miscut with the efficient annihilation of stacking faults, and a reduction of stacking fault density at the nucleation layer.

In the following section, we provide suggestions to address the above challenges.

8.2 Future work

A possible strategy of decreasing the stacking fault density generated at the GaN/SiC interface involves the introduction of an interlayer between SiC and zb-GaN with an intermediate lattice parameter, such as zb-AlGaN, to gradually reduce the lattice mismatch. However AlGaN nucleation layers require higher growth temperatures than GaN, which may result in wurtzite inclusions and faceting. Studies on the surface morphology by AFM, and on defects by cross-sectional TEM can be performed on the AlGaN nucleation layers to identify optimum growth conditions and determine whether they are effective in reducing defect densities.

A 2° miscut has the same effect of suppressing the formation of antiphase domains as a 4° miscut, and the feature sizes of zb-GaN nucleation layers and thicker epilayers grown on 2° and 4° miscut substrates are similar, although the surface roughness of the epilayers is slightly higher on 2° than the 4° miscut substrates. It would be worth investigating whether a 2° miscut reduces the preferential formation of stacking faults on the steeper {111} plane to the GaN/SiC interface compared with a 4° miscut, and to what degree. This can be answered by characterisation with XRD and cross-sectional TEM, similar to Chapter 6.

Apart from the aim of reducing stacking fault densities, we should also try to gain a better understanding of the impact of stacking faults on the structural and optical properties of an LED. While we have begun to investigate the effect that stacking faults have on the optical properties in GaN epilayers in Chapter 7, we have yet to study the effect of stacking faults in doped layers and InGaN quantum wells. It is possible that dopant atoms and/or indium will segregate to the stacking faults, which could affect optical properties. This could be investigated using a combination of STEM, photoluminescence spectroscopy and modelling. An improved understanding of the above could also lead us to think about the extent to which it is necessary to reduce the stacking fault densities. For example in wurtzite LEDs, the reduction of dislocation density did not prove to be as vital as expected.

While it is important to address the challenges that have been identified from this work, we should also press on with the development of the actual building blocks of an LED, which include p- and n-doped layers, InGaN/GaN quantum wells, and p- and n-type contacts.

P- and n-type doping in GaN can be achieved with Mg and Si, respectively. The presence of Mg and Si adatoms could affect the diffusion processes that take place on the GaN epilayer surface. Therefore, the effect of doping by such elements on the surface morphology and roughness of the GaN epilayers should be studied with the AFM. Our preliminary data has shown that Mg doping is able to decrease the surface roughness.

In conclusion, there are clearly a number of challenges that need to be overcome before a successful zincblende GaN green-wavelength LED can be achieved. There is still a lot left to develop, including doped layers and InGaN/GaN quantum wells, that provide room for creative ways to improve the material and more interesting scientific studies.

References

1. R. Gunn and M. Griffiths, “Lighting Technology,” 2010, <https://researchbriefings.parliament.uk/ResearchBriefing/Summary/POST-PN-351#fullreport> (accessed 11 August 2017).

2. H. F. Ford, “Seeing Blue: The Impact of Excessive Blue Light Exposure,” Review of Optometry, 2016, <https://www.reviewofoptometry.com/article/seeing-blue-the-impact-of-excessive-blue-light-exposure> (accessed 19 November 2016).

3. H. Morkoç, “Electronic Band Structure and Polarization Effects,” in Handbook of Nitride Semiconductors and Devices, pp. 131–321, Wiley-VCH [doi:10.1002/9783527628438.ch2].

4. I. Vurgaftman and J. R. Meyer, “Band parameters for nitrogen-containing semiconductors,” J. Appl. Phys. **94**(6), 3675–3696 (2003) [doi:10.1063/1.1600519].

5. D. J. As, “Recent developments on non-polar cubic group III-nitrides for optoelectronic applications,” in Proc. SPIE 7608, Quantum Sensing and Nanophotonic Devices VII **7608**, pp. 1–15 (2010) [doi:10.1117/12.846846].

6. M. R. Krames et al., “Status and future of high-power light-emitting diodes for solid-state lighting,” IEEE/OSA J. Disp. Technol. **3**(2), 160–175 (2007) [doi:10.1109/JDT.2007.895339].

7. P. Lefebvre et al., “High internal electric field in a graded-width InGaN/GaN quantum well: Accurate determination by time-resolved photoluminescence spectroscopy,” Appl. Phys. Lett. **78**(9), 1252–1254 (2001) [doi:10.1063/1.1351517].

8. C. X. Ren, “Polarisation fields in III-nitrides: effects and control,” Mater. Sci. Technol. **32**(5), 418–433 (2016) [doi:10.1179/1743284715Y.0000000103].

9. M. Zhu et al., “Inclined dislocation-pair relaxation mechanism in homoepitaxial green GaInN/GaN light-emitting diodes,” Phys. Rev. B - Condens. Matter Mater. Phys. **81**(12), 1–6 (2010) [doi:10.1103/PhysRevB.81.125325].

10. F. C. P. Massabuau et al., “The impact of trench defects in InGaN/GaN light emitting diodes and implications for the ‘green gap’ problem,” Appl. Phys. Lett. **105**(11), 18–23 (2014) [doi:10.1063/1.4896279].

11. T. Langer et al., “Strain-induced defects as nonradiative recombination centers in green-emitting GaInN/GaN quantum well structures,” Appl. Phys. Lett. **103**(2) (2013) [doi:10.1063/1.4813446].

12. A. M. Armstrong, M. H. Crawford, and D. D. Koleske, “Contribution of deep-level defects to decreasing radiative efficiency of InGaN/GaN quantum wells with increasing emission wavelength,” Appl. Phys. Express **7**(3) (2014) [doi:10.7567/APEX.7.032101].

13. T. Hanada, “Basic Properties of ZnO, GaN, and Related Materials,” in Oxide and Nitride Semiconductors - Processing, Properties, and Applications, 1st ed., T. Yao and S. K. Hong, Eds., pp. 1–19, Springer-Verlag Berlin Heidelberg (2009) [doi:10.1007/978-3-540-88847-5_1].

14. J. Schörmann et al., “Near ultraviolet emission from nonpolar cubic AlxGa1-xN/GaN quantum wells,” Appl. Phys. Lett. **89**, 131910 (2006) [doi:10.1063/1.2357587].

15. D. J. As and C. Mietze, “MBE growth and applications of cubic AlN/GaN quantum wells,” Phys. Status Solidi A **210**(3), 474–479 (2013) [doi:10.1002/pssa.201200653].

16. M. Abe et al., “Cubic GaN/AlGaN HEMTs on 3C-SiC Substrate for Normally-Off Operation,” IEICE Trans. Electron. **E89–C**(7), 1057–1063 (2006) [doi:10.1093/ietele/e89-c.7.1057].

17. D. J. As, “Cubic group-III nitride-based nanostructures — basics and applications in optoelectronics,” Microelectronics J. **40**, 204–209 (2009) [doi:10.1016/j.mejo.2008.07.036].

18. P. Gibart, “Metal organic vapour phase epitaxy of GaN and lateral overgrowth,” Reports Prog. Phys. **67**(5), 667–715 (2004) [doi:10.1088/0034-4885/67/5/R02].

19. D. Gerthsen et al., “Molecular beam epitaxy (MBE) growth and structural properties of GaN and AlN on 3C-SiC(001) substrates,” J. Cryst. Growth **200**(3–4), 353–361 (1999) [doi:10.1016/S0022-0248(99)00060-3].

20. D. J. As et al., “Cubic GaN epilayers grown by molecular beam epitaxy on thin β-SiC/Si (001) substrates,” Appl. Phys. Lett. **76**(13), 1686–1688 (2000) [doi:10.1063/1.126136].

21. H. Yang, O. Brandt, and K. Ploog, “MBE growth of cubic GaN on GaAs substrates,” Phys. Status Solidi B **194**, 109–120 (1996) [doi:10.1002/pssb.2221940112].

22. C. H. Wei et al., “MOCVD growth of cubic GaN on 3C-SiC deposited on Si (100) substrates,” J. Electron. Mater. **29**(3), 317–321 (2000) [doi:10.1007/s11664-000-0070-z].

23. T. Kitamura et al., “Growth and characterization of cubic InGaN epilayers on 3C-SiC by RF MBE,” J. Cryst. Growth **227–228**, 471–475 (2001) [doi:10.1016/S0022-0248(01)00745-X].

24. L. Y. Lee et al., “Effect of growth temperature and V/III-ratio on the surface morphology of MOVPE-grown cubic zincblende GaN,” J. Appl. Phys. **124**, 105302 (2018) [doi:10.1063/1.5046801].

25. A. Nakadaira and H. Tanaka, “Growth of zinc-blende GaN on GaAs (100) substrates at high temperature using low-pressure MOVPE with a low V/lll molar ratio,” J. Electron. Mater. **26**(3), 320–324 (1997) [doi:10.1007/s11664-997-0171-z].

26. J. Wu et al., “Crystal structure of GaN grown on 3C-SiC substrates by metalorganic vapor phase epitaxy,” Jpn. J. Appl. Phys. **36**, 4241–4245 (1997) [doi:10.1143/JJAP.36.4241].

27. Y. Hiroyama and M. Tamura, “Effect of very thin SiC layer on heteroepitaxial growth of cubic GaN on Si (001),” Jpn. J. Appl. Phys. **37**, L 630-L 632 (1998) [doi:10.1143/JJAP.37.L630].

28. H. Gamez-Cuatzin et al., “Electroluminescence characterization of cubic gallium nitride p-n junctions grown on SiC/Si substrates by MBE,” Phys. Status Solidi A **176**(1), 131–135 (1999) [doi:10.1002/(SICI)1521-396X(199911)176:1<131::AID-PSSA131>3.0.CO;2-D].

29. M. Häberlen et al., “Structural characterization of cubic and hexagonal GaN thin films grown by IBA – MBE on SiC / Si,” J. Cryst. Growth **312**, 762–769 (2010) [doi:10.1016/j.jcrysgro.2009.12.048].

30. J. G. Kim et al., “Growth by molecular beam epitaxy and electrical characterization of Si-doped zinc blende GaN films deposited on beta-SiC coated (001) Si substrates,” Appl. Phys. Lett. **65**(1), 91–93 (1994) [doi:10.1063/1.113085].

31. H. Tsuchiya et al., “Growth condition dependence of GaN crystal structure on (001)GaAs by hydride vapor-phase epitaxy,” J. Cryst. Growth **189–190**, 395–400 (1998) [doi:10.1016/S0022-0248(98)00322-4].

32. D. Wang et al., “Heteroepitaxial growth of cubic GaN on Si(001) coated with thin flat SiC by plasma-assisted molecular-beam epitaxy,” Appl. Phys. Lett. **76**(13), 1683 (2000) [doi:10.1063/1.126135].

33. M. Moret et al., “MOCVD growth of cubic gallium nitride: Effect of V/III ratio,” Phys. Status Solidi A **176**(1), 493–496 (1999) [doi:10.1002/(SICI)1521-396X(199911)176:1<493::AID-PSSA493>3.0.CO;2-6].

34. M. Mizuta et al., “Low Temperature Growth of GaN and AlN on GaAs Utilizing Metalorganics and Hydrazine,” Jpn. J. Appl. Phys. **25**(Part 2, No. 12), L945–L948, IOP Publishing (1986) [doi:10.1143/JJAP.25.L945].

35. H. Okumura et al., “Growth and characterization of cubic GaN,” J. Cryst. Growth **178**, 113 (1997) [doi:10.1016/S0022-0248(97)00084-5].

36. O. Brandt et al., “Growth of cubic GaN on (001) GaAs,” Mater. Res. Soc. Symp. Proc. **395**, 27–37 (1996) [doi:10.1557/PROC-395-27].

37. Z. H. Feng et al., “Effect on the optical properties and surface morphology of cubic GaN grown by metalorganic chemical vapor deposition using isoelectronic indium surfactant doping,” J. Cryst. Growth **235**, 207–211 (2002) [doi:10.1016/S0022-0248(01)01914-5].

38. D. Wang, S. Yoshida, and M. Ichikawa, “Si-doped cubic GaN grown on a Si(001) substrate with a thin flat SiC buffer layer,” Appl. Phys. Lett. **80**(14), 2472 (2002) [doi:10.1063/1.1467971].

39. D. J. As, D. Schikora, and K. Lischka, “Molecular beam epitaxy of cubic III-nitrides on GaAs substrates,” Phys. Status Solidi C **0**(6), 1607–1626 (2003) [doi:10.1002/pssc.200303133].

40. D. G. Pacheco-Salazar et al., “Growth and characterization of cubic InxGa1−xN epilayers on two different types of substrate,” J. Cryst. Growth **284**(3–4), 379–387 (2005) [doi:10.1016/j.jcrysgro.2005.07.049].

41. S. Li et al., “Room temperature green light emission from nonpolar cubic InGaN⁄GaN multi-quantum-wells,” Appl. Phys. Lett. **90**(7), 071903 (2007)

[doi:10.1063/1.2475564].

42. S. V Novikov et al., “Growth and characterization of free-standing zinc-blende (cubic) GaN layers and substrates,” Semicond. Sci. Technol **23**, 15018–5 (2008) [doi:10.1088/0268-1242/23/1/015018].

43. C. J. M. Stark et al., “Green cubic GaInN/GaN light-emitting diode on microstructured silicon (100),” Appl. Phys. Lett. **103**(23), 232107 (2013) [doi:10.1063/1.4841555].

44. S. Strite et al., “An investigation of the properties of cubic GaN grown on GaAs by plasma-assisted molecular-beam epitaxy,” J. Vac. Sci. Technol. B **9**(4), 1924–1929 (1991) [doi:10.1116/1.585381].

45. H. Okumura et al., “Observation of MBE-grown cubic-GaN/GaAs and cubic-GaN/3C-SiC interfaces by high resolution transmission electron microscope,” J. Cryst. Growth **164**, 149–153 (1996) [doi:10.1016/0022-0248(95)01073-4].

46. D. Schikora et al., “Epitaxial growth and optical transitions of cubic GaN films,” Phys. Rev. B **54**(12), R8381–R8384 (1996) [doi:10.1103/PhysRevB.54.R8381].

47. S. V Novikov et al., “Growth and characterization of free-standing zinc-blende (cubic) GaN layers and substrates,” Semicond. Sci. Technol. **23**, 015018 (2008) [doi:10.1088/0268-1242/23/1/015018].

48. J. N. Kuznia et al., “Low pressure metalorganic chemical-vapor deposition of cubic GaN over (100) GaAs substrates,” Appl. Phys. Lett. **65**(19), 2407–2409 (1994) [doi:10.1063/1.112690].

49. J. Wu et al., “Metalorganic vapor phase epitaxy growth of high quality cubic GaN on GaAs (100) substrates,” Jpn. J. Appl. Phys. **37**, 1440–1442 (1998) [doi:10.1143/JJAP.37.1440].

50. H. Yang et al., “Cubic-phase GaN light-emitting diodes,” Appl. Phys. Lett. **74**(17), 2498 (1999) [doi:10.1063/1.123019].

51. H. Vilchis, V. M. Sanchez-R., and A. Escobosa, “Cubic GaN layers grown by metalorganic chemical vapor deposition on GaN templates obtained by nitridation of GaAs,” Thin Solid Films **520**(16), 5191–5194 (2012) [doi:10.1016/j.tsf.2012.03.123].

52. M. J. Paisley et al., “Growth of cubic phase gallium nitride by modified molecular-

beam epitaxy," J. Vac. Sci. Technol. A **7**(3), 701 (1989) [doi:10.1116/1.575869].

53. B. Daudin et al., "How to grow cubic GaN with low hexagonal phase content on (001) SiC by molecular beam epitaxy," J. Appl. Phys. **84**(4), 2295–2300 (1998) [doi:10.1063/1.368296].

54. E. Martinez-Guerrero et al., "Structural properties of undoped and doped cubic GaN grown on SiC(001)," J. Appl. Phys. **91**(8), 4983–4987 (2002) [doi:10.1063/1.1456243].

55. D. J. As et al., "Spatially resolved optical emission of cubic GaN/AlN multi-quantum well structures," Mater. Res. Soc. Symp. Proc. **1736** (2014) [doi:10.1557/opl.2014.944].

56. R. M. Kemper et al., "Growth of cubic GaN on nano-patterned 3C-SiC / Si (001) substrates," J. Cryst. Growth **323**, 84–87 (2011) [doi:10.1016/j.jcrysgro.2010.12.042].

57. R. C. Powell et al., "Heteroepitaxial wurtzite and zinc-blende structure GaN grown by reactive-ion molecular-beam epitaxy: Growth kinetics, microstructure, and properties," J. Appl. Phys. **73**(1), 189–204 (1993) [doi:10.1063/1.353882].

58. M. Frentrup et al., "X-ray diffraction analysis of cubic zincblende III-nitrides," J. Phys. D. Appl. Phys. **50**, 433002 (2017) [doi:10.1088/1361-6463/aa865e].

59. O. Madelung, U. Rössler, and M. Schulz, Eds., "Silicon carbide (SiC) lattice parameters," in Group IV Elements, IV-IV and III-V Compounds. Part a - Lattice Properties. Landolt-Börnstein - Group III Condensed Matter (Numerical Data and Functional Relationships in Science and Technology), vol 41A1a., Springer, Berlin, Heidelberg [doi:10.1007/10551045_253].

60. O. Madelung, U. Rössler, and M. Schulz, Eds., "Gallium arsenide (GaAs) lattice parameters, thermal expansion," in Group IV Elements, IV-IV and III-V Compounds. Part a - Lattice Properties. Landolt-Börnstein - Group III Condensed Matter (Numerical Data and Functional Relationships in Science and Technology), vol 41A1a., Springer, Berlin, Heidelberg [doi:10.1007/10551045_104].

61. C. Bayram et al., "Cubic Phase GaN on Nano-grooved Si (100) via Maskless Selective Area Epitaxy," Adv. Funct. Mater. **24**, 4492–4496 (2014) [doi:10.1002/adfm.201304062].

62. P. Pirouz, C. M. Chorey, and J. A. Powell, “Antiphase boundaries in epitaxially grown beta-SiC,” Appl. Phys. Lett. **50**(4), 221–223 (1987) [doi:10.1063/1.97667].

63. H. Nagasawa and K. Yagi, “3C-SiC Single-Crystal Films Grown on 6-Inch Si Substrates,” Phys. Status Solidi B **202**(1), 335–358 (1997) [doi:10.1002/1521-3951(199707)202:1<335::AID-PSSB335>3.0.CO;2-Y].

64. R. M. Kemper et al., “Anti-phase domains in cubic GaN,” J. Appl. Phys. **110**, 123512 (2011) [doi:10.1063/1.3666050].

65. J. S. Song et al., “Optimization of ZnSe growth on miscut GaAs substrates by molecular beam epitaxy,” J. Cryst. Growth **249**(1–2), 128–143 (2003) [doi:10.1016/S0022-0248(02)02129-2].

66. S. H. Huang et al., “Simultaneous interfacial misfit array formation and antiphase domain suppression on miscut silicon substrate,” Appl. Phys. Lett. **93**, 071102 (2008) [doi:10.1063/1.2970997].

67. P. Kidd, *XRD of gallium nitride and related compounds: strain, composition and layer thickness*, Panalytical, ISBN: 978-90-809086-7-3, www.malvernpanalytical.com (2011).

68. F. La Via et al., “From thin film to bulk 3C-SiC growth: Understanding the mechanism of defects reduction,” Mater. Sci. Semicond. Process. **78**, 57–68 (2018) [doi:10.1016/J.MSSP.2017.12.012].

69. C. Long, S. a. Ustin, and W. Ho, “Structural defects in 3C–SiC grown on Si by supersonic jet epitaxy,” J. Appl. Phys. **86**(1999), 2509 (1999) [doi:10.1063/1.371085].

70. A. Severino et al., “Structural defects in (100) 3C-SiC heteroepitaxy: Influence of the buffer layer morphology on generation and propagation of stacking faults and microtwins,” Diam. Relat. Mater. **18**(12), 1440–1449 (2009) [doi:10.1016/j.diamond.2009.09.012].

71. A. Mantzari et al., “Some Recent Results on the 3C – SiC Structural Defects,” Acta Phys. Pol. A **121**(1), 187–189 (2012) [doi:10.1002/anie.199721111].

72. A. Trampert, O. Brandt, and K. H. Ploog, “Phase Transformations and Phase Stability in Epitaxial β-GaN Films,” Angew. Chem. Int. Ed. Engl. **36**(19), 2111–2112 (1997) [doi:10.1002/anie.199721111].

73. D. Chandrasekhar et al., “Characterization of Group III-nitride semiconductors by high-resolution electron microscopy,” J. Cryst. Growth **152**(3), 135–142 (1995) [doi:10.1016/0022-0248(95)00041-0].

74. F. Ruiz-Zepeda et al., “Precession electron diffraction-assisted crystal phase mapping of metastable c-GaN films grown on (001) GaAs,” Microsc. Res. Tech. **77**(12), 980–985 (2014) [doi:10.1002/jemt.22424].

75. R. M. Kemper, D. J. As, and J. Lindner, “Cubic GaN on nanopatterned 3C-SiC/Si (001) substrates,” in Silicon-based Nanomaterials, H. Li, J. Wu, and Z. M. Wang, Eds., pp. 381–406, Springer (2013) [doi:10.1007/978-1-4614-8169-0].

76. R. M. Kemper et al., “STEM-CL investigations on the influence of stacking faults on the optical emission of cubic GaN epilayers and cubic GaN/AlN multi-quantum wells,” Phys. Status Solidi C **12**(4–5), 469–472 (2015) [doi:10.1002/pssc.201400154].

77. M. Albrecht et al., “Luminescence Related to Stacking Faults in Heterepitaxially Grown Wurtzite GaN,” Mat. Res. Soc. Symp. Proc. V **468**, 293–298 (1997) [doi:10.1557/PROC-468-293].

78. C. Stampfl and C. G. Van de Walle, “Energetics and electronic structure of stacking faults in AlN , GaN , and InN,” Phys. Rev. B **57**(24), 52–55 (1998) [doi:10.1103/PhysRevB.57.R15052].

79. A. Trampert et al., “Direct observation of the initial nucleation and epitaxial growth of metastable cubic GaN on (001) GaAs,” Appl. Phys. Lett. **70**(5), 583–585 (1997) [doi:10.1063/1.118281].

80. J. P. Hirth and J. Lothe, *Theory of Dislocations, Second Edition*, New York: McGraw-Hill (1982).

81. A. T. Blumenau et al., “Dislocations in hexagonal and cubic GaN,” J. Phys. Condens. Matter **12**, 10223–10233 (2000) [doi:10.1088/0953-8984/12/49/322].

82. T. Zhu, “Nanoscale electrical characterization of gallium nitride,” PhD Thesis, Department of Materials Science and Metallurgy, University of Cambridge (2010).

83. P. Eaton and P. West, “Atomic Force Microscopy,” p. 55, Oxford University Press Inc., New York (2010).

84. B. Pittenger, N. Erina, and C. Su, “Application Note #128 Quantitative Mechanical

Property Mapping at the Nanoscale with PeakForce QNM," 2012, <https://www.bruker.com/fileadmin/user_upload/8-PDF-Docs/SurfaceAnalysis/AFM/ApplicationNotes/AN128-RevB0-Quantitative_Mechanical_Property_Mapping_at_the_Nanoscale_with_PeakForceQNM-AppNote.pdf> (accessed 15 January 2019).

85. H. Schillers et al., "PeakForce Tapping resolves individual microvilli on living cells" (2015) [doi:10.1002/jmr.2510].

86. Bruker Inc, "PeakForce Tapping - How AFM Should Be," <https://www.bruker.com/products/surface-and-dimensional-analysis/atomic-force-microscopes/modes/modes/imaging-modes/peakforce-tapping/overview.html> (accessed 15 January 2019).

87. F. Massabuau, "The impact of the nanostructure of InGaN/GaN quantum wells on LED efficiency," PhD Thesis, Department of Materials Science and Metallurgy, University of Cambridge (2014).

88. I. Horcas et al., "WSXM: A software for scanning probe microscopy and a tool for nanotechnology," Rev. Sci. Instrum. **78**(1), 013705, American Institute of Physics (2007) [doi:10.1063/1.2432410].

89. D. B. Williams and C. B. Carter, *Transmission Electron Microscopy: A Textbook for Materials Science*, 2nd ed., Springer US (2009) [doi:10.1007/978-0-387-76501-3].

90. S. E. Bennett, "Nitride Semiconductors Studied By Atom Probe Tomography and Correlative Techniques," PhD Thesis, Department of Materials Science and Metallurgy, University of Cambridge (2010).

91. O. Brandt et al., "Optimized growth conditions for the epitaxial nucleation of beta-GaN on GaAs(001) by molecular beam epitaxy," Appl. Phys. Lett. **71**(4), 473–475 (1997) [doi:10.1063/1.119583].

92. X. H. Wu et al., "Nucleation layer evolution in metal-organic chemical vapor deposition grown GaN," Appl. Phys. Lett. **1371**(1996), 1371 (1995) [doi:10.1063/1.116083].

93. V. Narayanan et al., "Gallium nitride epitaxy on (0001) sapphire," Philos. Mag. A **82**(5), 885–912 (2002) [doi:10.1080/01418610208240008].

94. J. Wu et al., “Optical Properties of Cubic GaN Grown on 3C-SiC (100) Substrates by Metalorganic Vapor Phase Epitaxy,” Phys. Status Solidi A **180**(1), 403–407 (2000) [doi:10.1002/1521-396X(200007)180:1<403::AID-PSSA403>3.0.CO;2-A].

95. D. Nečas and P. Klapetek, “Gwyddion: an open-source software for SPM data analysis,” Cent. Eur. J. Phys. **10**(1), 181–188, SP Versita (2012) [doi:10.2478/s11534-011-0096-2].

96. U. W. Pohl, “Thermodynamics of Epitaxial Layer-Growth,” in Epitaxy of Semiconductors, pp. 154–155, Springer-Verlag Berlin Heidelberg (2013).

97. K. Lorenz et al., “Comparative study of GaN and AlN nucleation layers and their role in growth of GaN on sapphire by metalorganic chemical vapor deposition,” Appl. Phys. Lett. **77**(21), 3391 (2000) [doi:10.1063/1.1328091].

98. H. Gao et al., “Atomistic models of dislocation formation at crystal surface ledges in Si1-xGex/Si(100) heteroepitaxial thin films,” Philos. Mag. A **79**(2), 349–370 (1999) [doi:10.1080/01418619908210303].

99. V. Narayanan et al., “Origins of threading dislocations in GaN epitaxial layers grown on sapphire by metalorganic chemical vapor deposition,” Appl. Phys. Lett. **78**(11), 1544–1546 (2001) [doi:10.1063/1.1352699].

100. K. Saarinen et al., “Gallium vacancies and the growth stoichiometry of GaN studied by positron annihilation spectroscopy,” Appl. Phys. Lett. **73**(22), 3253 (1998) [doi:10.1063/1.122735].

101. D. Holec et al., “Critical thickness calculations for InGaN/GaN,” J. Cryst. Growth **303**(1), 314–317 (2007) [doi:10.1016/J.JCRYSGRO.2006.12.054].

102. D. J. Dunstan, “Strain and strain relaxation in semiconductors,” J. Mater. Sci. Mater. Electron. **8**, 337–375 (1997) [doi:10.1023/A:1018547625106].

103. P. Ferret et al., “Observation of Lomer-Cottrell locks in SiGe strained layers,” Appl. Phys. Lett **57**, 2220 (1990) [doi:10.1063/1.103896].

104. U. Kaiser and I. I. Khodos, “On the determination of partial dislocation Burgers vectors in fcc lattices and its application to cubic SiC films,” Philos. Mag. A **82**(3), 541–551 (2002) [doi:10.1080/01418610208239615].

105. D. Hull and D. J. Bacon, “Dislocations in Face-centered Cubic Metals,” in

Introduction to dislocations, Fifth Edition, pp. 85–107, Butterworth-Heinemann (2011).

106. M.-K. Wei, "Introduction to Dislocations," <http://www.ndhu.edu.tw/ezfiles/29/1029/img/3034/Chapter4-1_1041020.pdf> (accessed 26 October 2018).

107. H. Amano et al., "Improvement of Crystalline Quality of Group III Nitrides on Sapphire Using Low Temperature Interlayers," MRS Internet J. Nitride Semicond. Res. **4**(S1), 870–877 (1999) [doi:10.1557/S1092578300003550].

108. Y. S. Cho et al., "Reduction of stacking fault density in-plane GaN grown on SiC," Cit. Appl. Phys. Lett **93**, 111904 (2008) [doi:10.1063/1.2985816].

109. H. Marchand et al., "Metalorganic chemical vapor deposition of GaN on Si(111): Stress control and application to field-effect transistors," J. Appl. Phys. **89**(12), 7846–7851 (2001) [doi:10.1063/1.1372160].

110. S. Ploch et al., "Single phase {11-22} GaN on (10-10) sapphire grown by metal-organic vapor phase epitaxy," J. Cryst. Growth **331**(1), 25–28 (2011) [doi:10.1016/j.jcrysgro.2011.06.057].

111. H. Gao and W. D. Nix, "Surface Roughening of Heteroepitaxial Thin Films," Annu. Rev. Mater. Sci. **29**, 173–209 (1999) [doi:10.1146/annurev.matsci.29.1.173].

112. L. Lymperakis and J. Neugebauer, "Large anisotropic adatom kinetics on nonpolar GaN surfaces: Consequences for surface morphologies and nanowire growth," Phys. Rev. B - Condens. Matter Mater. Phys. **79**, 241308(R) (2009) [doi:10.1103/PhysRevB.79.241308].

113. U. W. Pohl, "Atomistic Aspects of Epitaxial Layer-Growth," in Epitaxy of Semiconductors, pp. 171–224, Springer-Verlag Berlin Heidelberg (2013).

114. S. Ploch et al., "Surface diffusion and layer morphology of (112-2) GaN grown by metal-organic vapor phase epitaxy," J. Appl. Phys. **111**, 033526 (2012) [doi:10.1063/1.3682513].

115. M. Barchuk et al., "Diffuse x-ray scattering from stacking faults in a-plane GaN epitaxial layers," Phys. Rev. B **84**(094113), 1–8 (2011) [doi:10.1103/PhysRevB.84.094113].

116. S. A. Church et al., “Effect of stacking faults on the photoluminescence spectrum of zincblende GaN,” J. Appl. Phys. **123**(18), 185705 (2018) [doi:10.1063/1.5026267].

117. A. Philippe et al., “Optical properties of cubic GaN grown on SiC/Si substrates,” Mater. Sci. Eng. B **59**(1–3), 168–172 (1999) [doi:10.1016/S0921-5107(98)00413-9].

118. E. Martinez-Guerrero et al., “p and n type doping of cubic GaN on SiC (001),” Mater. Sci. Eng. B **82**, 59–61 (2001) [doi:10.1016/S0921-5107(00)00719-4].

119. S. N. Waheeda et al., “Low fraction of hexagonal inclusions in thick and bulk cubic GaN layers,” Appl. Surf. Sci. **317**, 1010–1014 (2014) [doi:10.1016/J.APSUSC.2014.08.186].

120. J. Lähnemann et al., “Luminescence associated with stacking faults in GaN,” J. Phys. D. Appl. Phys. **47**(42), 423001 (2014) [doi:10.1088/0022-3727/47/42/423001].

121. S. A. Church et al., “Photoluminescence studies of cubic GaN epilayers,” Phys. Status Solidi B **254**(8), 1600733 (2017) [doi:10.1002/pssb.201600733].

122. D. Wang et al., “Initial growth of cubic GaN on Si(0 0 1) coated with a thin flat SiC buffer layer,” J. Cryst. Growth **220**(3), 204–208 (2000) [doi:10.1016/S0022-0248(00)00839-3].

123. W. H. Press et al., “Numerical recipes: the art of scientific computing, Third Edition,” pp. 727–728, Cambridge University Press (2007).

124. G. Parish et al., “SIMS Investigations into the Effect of Growth Conditions on Residual Impurity and Silicon Incorporation in GaN and AlxGa1-xN,” J. Electron. Mater. **29**(1), 15–20 (2000) [doi:10.1007/s11664-000-0087-3].